Towards Sustainable Manufacturing of Brass Components

Charaterisation, Machinability and Solid-State Recycling of Lead-Free Brass

Johansson, Jakob

2022

Document Version:
Publisher's PDF, also known as Version of record

Citation for published version (APA):
Johansson, J. (2022). *Towards Sustainable Manufacturing of Brass Components: Charaterisation, Machinability and Solid-State Recycling of Lead-Free Brass* (1 ed.). [Doctoral Thesis (compilation), Production and Materials Engineering]. Department of Production and Materials Engineering, LTH, Lund University,.

Total number of authors:
1

Creative Commons License:
Unspecified

Towards Sustainable Production of Brass Components

Characterisation, Machinability and Solid-State Recycling of Lead-Free Brass Alloys

JAKOB JOHANSSON
FACULTY OF ENGINEERING | LUND UNIVERSITY

Towards Sustainable Production of Brass Components

Characterisation, Machinability and Solid-State Recycling of Lead-Free Brass Alloys

Jakob Johansson

LUND
UNIVERSITY

DOCTORAL DISSERTATION

by due permission of the Faculty of Engineering, Lund University, Sweden.
To be defended at lecture hall KC:B, KemiCentrum, LTH, Naturvetarvägen 14 /
Sölvegatan 39 A-C, Lund. 2022-06-17 at 9.15

Faculty opponent
Professor Andreas Archenti

Department of Production Engineering, KTH Royal Institute of Technology,
Stockholm, Sweden.

Organization	Document name
Division of Production and Materials Engineering Faculty of Engineering LUND UNIVERSITY	Doctoral dissertation
	Date of issue
Author: Jakob Johansson	Sponsoring organization

Title and subtitle: Towards Sustainable Production of Brass Components - Characterisation, Machinability and Solid-State Recycling of Lead-Free Brass Alloys

Abstract:

Brass is a generic term for alloys with copper and zinc as the main constituents. It is one of the most common engineering materials and is used in plumbing components, locks and keys, automotive components, home furnishings, electronic components, small fasteners and musical instruments. Its good machining characteristics mean that it is often used for components where a large proportion of the workpiece material is removed during the manufacturing process, such as pipe fittings.

A contributing factor to the material's high machinability is that it traditionally contains lead (Pb). However, lead is a heavy metal that is hazardous to the environment and human health and should not be released into nature or society. New regulations are being introduced restricting the lead content of materials in various component categories, with the result that traditional alloys with high lead content can no longer be used in certain applications.

As high lead alloys are being phased out, it is important to identify differences in the mechanical properties of high and low lead alloys and to clarify how these differences affect the machinability of materials. In particular, it is important to be able to describe how lead increases the machinability of brass. If we understand this mechanism, we can use this knowledge to find sustainable ways to increase the machinability of lead-free brass. Accordingly, this dissertation explains the mechanisms that give brass with high lead content better machinability than lead-free alloys.

Any cutting operation produces metal cutting chips as a by-product. In the manufacture of small, hollow components such as pipe fittings and other plumbing components, it is not uncommon for more than half the raw material used to make a product to be cut away, giving rise to chips or other residues from the manufacturing process. These chips are usually sent back to the manufacturer of the raw material for recycling by remelting into new raw material. This transportation of large quantities of material between component manufacturers and raw material manufacturers does not add any real value. Developing a method of recycling chips in the solid state by hot forging at the component manufacturers would eliminate the need for transportation and increase the utilisation rate of the raw material, so contributing to a more sustainable industry. This dissertation thus also reports on investigations and developmental work showing that it is possible to recycle brass chips by hot forging. A life cycle assessment shows that the method results in reduced energy demand for manufacturing and thus a reduction in emissions that contribute to climate change.

Key words: Brass, Lead-free brass, Material properties, Machinability, Recycling

Classification system and/or index terms (if any)

Supplementary bibliographical information	**Language:** English
ISSN and key title	ISBN 978-91-8039-271-6 (print) ISBN 978-91-8039-272-3(electronic)

Recipient's notes	**Number of pages** 128	Price
	Security classification	

Signature   Date 2022-05-05

Towards Sustainable Production of Brass Components

Characterisation, Machinability and Solid-State Recycling of Lead-Free Brass Alloys

Jakob Johansson

LUND
UNIVERSITY

Acknowledgments

Abstract

Brass is a generic term for alloys with copper and zinc as the main constituents. It is one of the most common engineering materials and is used in plumbing components, locks and keys, automotive components, home furnishings, electronic components, small fasteners and musical instruments. Its good machining characteristics mean that it is often used for components where a large proportion of the workpiece material is removed during the manufacturing process, such as pipe fittings.

A contributing factor to the material's high machinability is that it traditionally contains lead (Pb). However, lead is a heavy metal that is hazardous to the environment and human health and should not be released into nature or society. New regulations are being introduced restricting the lead content of materials in various component categories, with the result that traditional alloys with high lead content can no longer be used in certain applications.

As high lead alloys are being phased out, it is important to identify differences in the mechanical properties of high and low lead alloys and to clarify how these differences affect the machinability of materials. In particular, it is important to be able to describe how lead increases the machinability of brass. If we understand this mechanism, we can use this knowledge to find sustainable ways to increase the machinability of lead-free brass. Accordingly, this dissertation explains the mechanisms that give brass with high lead content better machinability than lead-free alloys.

Any cutting operation produces metal cutting chips as a by-product. In the manufacture of small, hollow components such as pipe fittings and other plumbing components, it is not uncommon for more than half the raw material used to make a product to be cut away, giving rise to chips or other residues from the manufacturing process. These chips are usually sent back to the manufacturer of the raw material for recycling by remelting into new raw material. Transportation of large quantities of material between component manufacturers and raw material manufacturers does not add any real value. Developing a method of recycling chips in the solid state by hot forging at the component manufacturers would eliminate the need for transportation and increase the utilisation rate of the raw material, so contributing to a more sustainable industry. This dissertation thus also reports on investigations and developmental work showing that it is possible to recycle brass chips by hot forging. A life cycle assessment shows that the method results in reduced energy demand for manufacturing and thus a reduction in emissions that contribute to climate change.

Keywords: *Lead-free brass, Material properties, Machinability, Recycling*

Populärvetenskaplig sammanfattning

Mässing är ett samlingsnamn för legeringar där koppar och zink är huvudbeståndsdelarna och ett av våra vanligaste konstruktionsmaterial. Exempel på produkter som ofta tillverkas i mässing är VVS-komponenter, lås och nycklar, fordonskomponenter, prydnadsföremål som ljusstakar och dylikt, elektronikkomponenter, små fästelement och musikinstrument. Materialets goda egenskaper vid skärande bearbetning gör att komponenter där en stor del av ursprungsmaterialet avverkas under tillverkningsprocessen, t.ex. rörkopplingar, ofta tillverkas i mässing. En bidragande orsak till materialets höga skärbarhet är att det, traditionellt sett, innehåller bly. Bly är en miljö- och hälsofarlig tungmetall som inte bör spridas i natur eller samhälle och därför kommer nya regler att införas angående blyinnehållet för material i olika komponentkategorier, vilket kommer att innebära att de traditionellt använda legeringarna med höga halter av bly inte längre kan användas i vissa applikationer.

Eftersom legeringar med högt blyinnehåll håller på att fasas ut är det av vikt att kartlägga skillnader i mekaniska egenskaper mellan legeringar med högt respektive lågt blyinnehåll och klargöra hur dessa skillnader påverkar materialens skärbarhet. Det är särskilt viktigt att beskriva på vilket sätt bly bidrar till att öka skärbarheten i mässing. Om vi förstår hur bly ökar skärbarheten kan kunskapen användas för att hitta andra, hållbara, sätt att öka skärbarheten hos blyfri mässing. I avhandlingen förklaras mekanismerna som gör att mässing med hög blyhalt har bättre skärbarhet än blyfria legeringar.

Vid all skärande bearbetning kommer spånor att vara en biprodukt. Vid tillverkning av små och ihåliga komponenter, som rörkopplingar och andra VVS-komponenter, är det inte ovanligt att över hälften av råmaterialet som används för att tillverka en produkt skärs bort och ger upphov till spånor eller andra restprodukter från tillverkningsprocessen. Spånorna skickas oftast tillbaka till tillverkaren av råmaterialet för återvinning genom omsmältning till nytt råmaterial. Härigenom transporteras stora mängder material mellan komponent- och råmaterialtillverkare, ett transportarbete som inte skapar något egentligt mervärde. Genom att utveckla en återvinningsmetod där spånorna inte smälts ner utan kan återvinnas i fast fas med hjälp av varmsmide direkt hos komponenttillverkare är det möjligt att eliminera transportarbete och öka utnyttjandegraden av råmaterialet, och på så sätt bidra till en mer hållbar industri. Undersökningar och utvecklingsarbete av återvinningsmetoden som redovisas i avhandlingen visar att det är möjligt att återvinna mässingsspån genom varmsmide. I utvecklingsarbetet ingår en livscykelanalys som visar att metoden ger upphov till minskad energiåtgång för tillverkning och logistik och därmed reduktion av utsläpp som bidrar till klimatförändringar.

Nyckelord: *Blyfri mässing, mekaniska egenskaper, skärbarhet, återvinning.*

Appended Publications

This dissertation is based on the work presented in the following publications. In the text, these publications are referred to with Roman numerals I-VI.

I   **Machinability Evaluation of Low-Lead Brass Alloys**
        Johansson, J. Persson. H., Ståhl, J.-E., Zhou, J.M., Bushlya, V. *Procedia Manufacturing*, 2019. **38**: p. 1723-1730,
        DOI: https://doi.org/10.1016/j.promfg.2020.01.102.

II   **On the function of lead (Pb) in machining brass alloys**
        Johansson, J., Alm, P., M'Saoubi, R., Malmberg, P., Ståhl, J.-E., Bushlya, V., *The International Journal of Advanced Manufacturing Technology*, 2022, DOI: http://doi.org/10.1007/s00170-022-09205-0.

III   **Influence of subsurface deformation induced by machining on stress corrosion cracking in lead-free brass**
        Johansson, J., Bushlya, V., Obitz, C., M'Saoubi, R., Hagström, J., Lenrick, F. (Manuscript, submitted to *The International Journal of Advanced Manufacturing Technology*)

IV   **Hot forging operations of brass chips for material reclamation after machining operations**
        Johansson, J., Ivarsson, L., Ståhl, J.-E., Bushlya, V., Schultheiss, F., *Procedia Manufacturing,* 2017. **11**: p. 584-592,
        DOI: http://doi.org/10.1016/j.promfg.2017.07.152.

V   **Determining process parameters for successful material reclamation of lead-free brass chips using hot forging operations: Lubrication**
        Johansson, J., Gutnichenko, O., Ståhl, J.-E., Bushlya, V., Schultheiss, F., *Procedia CIRP*, 2019. **80**: p. 108-113,
        DOI: https://doi.org/10.1016/j.procir.2019.01.086.

VI   **Screening environmental impact reduction enabled by brass reclamation through hot forging operations**
        Johansson, J., Furberg, A., Schultheiss, F., *Advances in Transdisciplinary Engineering*, Presented at: 9th Swedish Production Symposium, SPS 2020. 2020. DOI: http://doi.org/10.3233/ATDE200162.

Author's Contribution

I   Johansson planned the work, performed the majority of the experimental work in collaboration with Persson, and wrote a major part of the paper.

II   Johansson planned the work, performed the majority of the experimental work, and wrote a major part of the paper.

III   Johansson planned the work, performed the majority of the experimental work, and wrote the paper in collaboration with Bushlya and Obitz. Obitz performed the corrosion testing.

IV   Johansson planned the work, performed the majority of the experimental work in collaboration with Ivarsson, and wrote a major part of the paper.

V   Johansson planned the work, performed the majority of the experimental work, and wrote a major part of the paper. Gutnichenko assisted in the statistical analysis of the influence of process parameters on the finished product.

VI   Johansson performed the majority of the experimental work and wrote a major part of the paper. Furberg performed the LCA analysis.

List of Symbols and Abbreviations

a_p	Depth of cut	mm
b_1	Theoretical chip width	mm
Al	Aluminium	-
As	Arsenic	-
BUE	Built-up edge	-
BUL	Built-up layer	-
Cu	Copper	-
Cr	Cutting resistance	N/mm^2
EBSD	Electron backscatter diffraction	-
f	Feed	mm/rev
F_c	Main cutting force	N
F_f	Feed force	N
F_p	Passive force	N
FIB	Focused ion beam	-
h_1	Theoretical chip thickness	mm
ICCI	Ion channelling contrast imaging	-
l_c	Contact length	mm
K_{v5}	Impact toughness for a 5 mm Charpy V-notch sample	kJ/m^2
K_W	Thermal conductivity	W/mK
LCA	Life cycle assessment	-
Pb	Lead	-
P	Phosphorus	-
r	Nose radius	mm
r_β	Edge radius	μm
R_{p02}	Proof strength at 0.2 % elongation	N
R_m	Ultimate tensile strength	N
SAED	Selected area electron diffraction	-
S_n	Strain hardening factor	-

SCC	Stress corrosion cracking	-
SEM	Scanning electron microscope	-
Si	Silicon	-
TEM	Transmission electron microscope	-
v_c	Cutting speed	m/min
VB	Flank wear	mm
XEDS	Energy dispersive x-ray spectroscopy	-
XRD	X-ray diffraction	-
Zn	Zinc	-
ε_b	Elongation at break	%
ε_I	Width of the deformation zone in zone I	mm
ε_{II}	Width of the deformation zone in zone II	mm
ε_{III}	Width of the deformation zone in zone III	mm
α	Clearance angle	°
β	Wedge angle	°
ε	Included angle	°
κ	Major cutting edge angle	°
κ_b	Minor cutting edge angle	°
λ	Inclination angle	°
γ	Rake angle	°

Table of Contents

1 Introduction

Brass, an alloy composed mainly of copper and zinc, is commonly used in parts production. To facilitate parts manufacturing, lead has traditionally been added to brass alloys. However, increased regulations on lead content in certain applications and environmental concerns require that brass with a high lead content be substituted for lead-free brass alloys. These regulations concern both the alloy manufacturing companies and component manufacturing companies. Systematic research on lead-free brass alloys, their machinability and manufacturability started in 2019 with OptiBrass research project (sponsored by the strategic innovation program Metallic Materials) which brought together twelve manufacturing companies from Sweden, Norway and Germany. An extensive range of components and products is affected, including valves, fittings and faucets, brass semi-products such as rods and ingots, automotive components and couplings for pressurised air and hydraulics.

1.1 Historical overview

Copper (Cu) was one of the first metallic materials that humans learned to use, starting around 1200–900 BC [1]. A few examples of prehistoric copper alloy with a small percentage of zinc (Zn) are known, but it is believed that deliberate production of brass began in the first millennium BC in Asia Minor [2]. Ore containing Zn is often found in association with Cu and lead (Pb). However, the boiling point of Zn at normal pressure (905 °C) is lower than the melting point of Cu (1083 °C), so that much Zn would have been lost during the roasting and subsequent melting of the ore. This made production of brass complicated with early metallurgical equipment.

The earliest known example of brass with high zinc content was in an object described as 'a worthless corroded pin' that was excavated in the early Palestinian Bronze Age village of Gezer by Macalister [3]. It had a measured Zn content of 23 wt.% but it is unclear whether the alloy had deliberately been made with so high a Zn content. Brass remained rare, although there are references to it in Greek literature from the 7th century BC on under the name *Oreichalkos* (mountain copper). It appears to have been an extremely valuable metal [2]. Until Roman times, most of the Cu alloys that have been found were alloyed with tin (Sn) to form

bronze, often with a small percentage of Pb [4]. In the Roman empire, brass was used for making coins between the first and third century AD. It was later used as a material for general metal working with the addition of Pb to improve its casting properties and machinability [2]. The practice of alloying Cu alloys with Pb is, in other words, not new, as it has been used since Cu alloys were discovered.

A somewhat more recent example of the historical use of brass was retrieved from the wreckage of the *Gribshunden*, the flagship of Hans, king of Denmark, that was lost in a storm in 1495. In the wreckage, the remains of chain mail with brass embellishments were found, together with a maker's ring from the blacksmith who made the chain mail. After so long on the sea floor, the steel that made up the bulk of the chain mail has been consumed by corrosion and anaerobic bacteria, but the brass embellishments were still intact when excavated in 2006 and 2019. Work is ongoing to map the trade routes for brass during the 13th century and the production methods used to make chain mail of this type. A cross section of a ring from the chain mail can be seen in Figure 1.1. The dark, wedge-shaped area seen in the top of the cross section is an iron-rich, non-crystalline area that may be related to the production of the ring or to reactions with the decomposing steel that was originally in the chain mail. The distribution of Pb in the brass and the size distribution of the bright Pb globules shown in the scanning electron microscope (SEM) image are similar to what is found in modern brass.
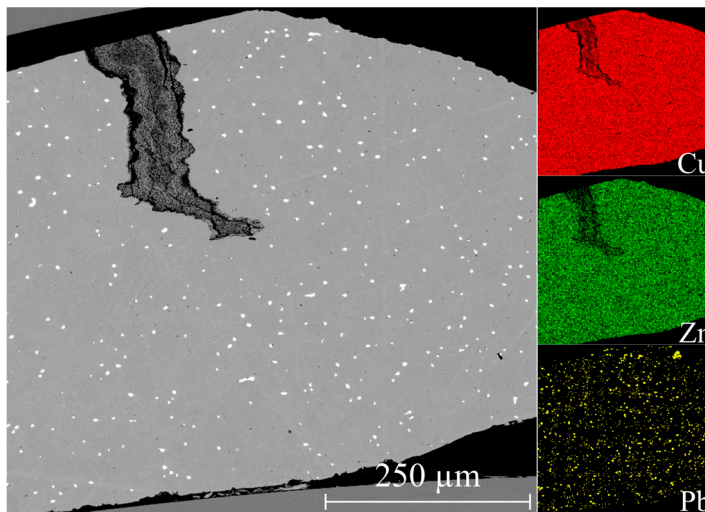
Figure 1.1. SEM image and elemental XEDS maps of a link of chain mail found in excavation of the Danish ship *Gribshunden* that sank outside Ronneby, Sweden, in 1495.

One of the earliest works on the subject of machining was presented by Rumford in 1798 [5]. He used four different experiments to investigate the heat generated when turning brass cannons. His conclusions were that the heat generated in turning is

caused by friction and that the amount of heat is inexhaustible, possibly disproving the existence of heat as a material substance. However, Rumford did not want to make any positive statement about the existence or non-existence of an 'igneous fluid', which, at the time, was believed to be the source of heat and appears to have been a divisive subject among philosophers.

1.2 Production of brass parts in general

Brass is the preferred material when demands on corrosion resistance are high, demands on mechanical strength are moderate, and electrical and thermal conductivity is desired. Besides these demands on the finished product, brass also has several characteristics that makes it easy to reshape and produce parts.

Common product categories manufactured in brass include pipe fittings, keys and locks, automotive components, small fastening elements, electrical components, architectural fittings, and home furnishings and utensils.

Brass with a high Cu content is commonly used for the production of such things as ammunition cartridges (whence the commonly used name 'cartridge brass' for alloys with approximately 70 wt.% Cu and the remainder Zn) [6]. The metal is soft and ductile, which makes it ideal for cold forming but difficult to machine. By introducing annealing steps in the cold forming process, it is possible to reshape brass to a high degree.

By increasing the Zn content of brass above 35 wt.%, the brass will become duplex. The formation of a secondary phase provides increased strength and lower ductility, making the material more machinable than single phase brass. Duplex brass alloys are suitable for hot forging, often in combination with machining as in Figure 1.2. Less workpiece material and production time is needed to make components compared to only using metal cutting if the component is first hot forged to roughly shape it. Metal cutting can then create features with higher tolerances regarding geometry and surface roughness.

Brass components or blanks for subsequent machining can also be cast using high- or low-pressure casting methods. In Sweden, there are currently more than ten foundries for brass components with a combined yearly production capacity of 7,700 tonne [7]. Casting provides great freedom of form within certain limitations, such as requiring an even wall thickness for good solidification, appropriate draft angles when applicable, and avoiding narrow sections that makes it difficult for the metal to fill the form cavity.
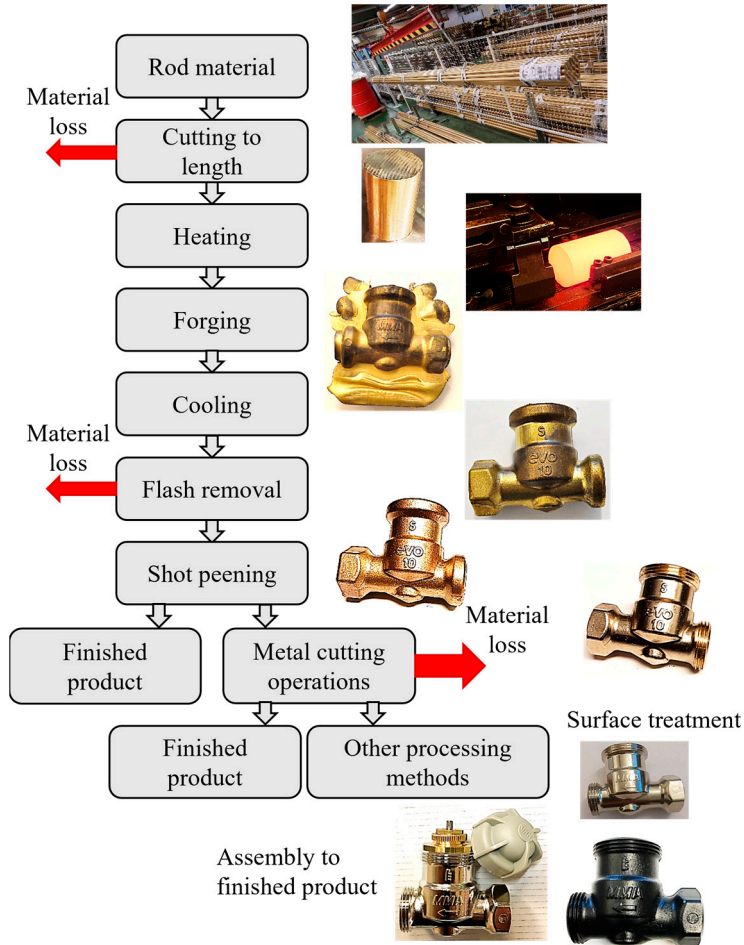
Figure 1.2. General process steps for a hot forged and machined brass component.

1.3 Reasons for not using lead in society

Pb has many applications in today's society, the most prominent of which is its use in lead-acid accumulators, commonly found in cars. Historically, Pb has been used as, among other things, an additive in petrol and as pigment in paint. These practices are now banned in most countries since they caused dispersion of Pb, which impacts living organisms negatively [8]. The use of Pb in petrol is extremely harmful since vehicle emissions will contain Pb in small particles that can be absorbed by humans via the respiratory system [9]. Paint containing Pb is also concerning for it is still present in residences. In the USA, lead-based paint was banned in 1978 [10], but

this did not prevent George H. W. Bush's dog from getting lead poisoning during a renovation of the White House in 1990 [11]. Although this is merely anecdotal evidence, it shows that even though a substance is banned from a certain application, it will remain in use until replaced.

Pb is added to brass alloys, mainly to aid in the manufacturing of parts. When Pb is added to brass in a sufficient amount, it will segregate into pure Pb globules since it is almost insoluble in brass [12]. These Pb globules provide several advantages in manufacturing that will be discussed later in this dissertation.

The suitability of lead-containing materials in drinking water applications has long been questioned. Samandi and Wise [13] point out that presence of lead in drinking water was already causing international concern in 1989. One well-known example of its detrimental effects comes from Flint, USA. In 2014, the town was switched from one water source to another without adequate attention being paid to the corrosive characteristics of the water from the new source or the ageing water distribution infrastructure in the area, which relied on old lead pipes. The Pb from these pipes then leached into the water consumed in households [14; 15].

Even though the detrimental effects of Pb are well known, use of the metal is increasing worldwide. According to the International Lead and Zinc Study Group, 2 % of the world's refined Pb was used in alloys in 2018, and 80 % in the production of batteries [16]. The need to phase out the use of Pb is reflected in companies' internal targets for long-term sustainable production as well as in tighter legislation at the EU level. In December 2020, a revised EU Drinking Water Directive came into force [17]. It sets a maximum Pb content in drinking water of 5 µg/l, half the level of the previous directive. Implementation of the directive in national laws is currently in progress in the EU. The alloys approved for use in contact with drinking water are determined by migration tests overseen by a dedicated group of four member states, called 4MS. The 4MS group has developed a 'Common Approach' that establishes a procedure for acceptance and a composition list of metals that are suitable for contact with drinking water [18]. The brass alloys suitable for contact with drinking water are referenced in the '4MS Common Composition List' [18]. This is a dynamic list to which alloys can be added or removed after acceptance tests.

The presence of Pb in various products is also regulated through two other EU directives and regulations: REACH (Registration, Evaluation, Authorisation and Restriction of Chemicals) and RoHS (Restriction of the Use of certain Hazardous Substances in Electrical and Electronic Equipment). These directives regulate the maximum lead content in products and components and how these should be reported and managed as waste. A comprehensive review of regulations regarding Pb in drinking water applications for different regions and their impact on the brass value chain was presented by Estelle in 2016 [19], but these regulations are susceptible to changes and updates may be needed.

1.4 Background and objective

The amount of published work about manufacturing in brass is not very large compared to that for other common engineering materials like steel, aluminium or titanium. One reason for the difference may be brass's high machinability and castability. Since the material is easy to work with, interest in improving production processes for brass part production has been low. Until 1990 there was some attention from the scientific community on the function of Pb in brass [20-22], specifically in machining [13; 23-28]. After 1990, with few exceptions [29-32], not much was published until discussions about restrictions on the Pb content of brass began around 2010. Articles published after 2010 about machining brass mainly focus on comparing the process behaviour and results of machining traditional free-machining brass (< 3 wt.% Pb) and Pb-free alloys [33-39] or alternative alloying routes for lead-free brass [40-42]. Few review papers for the subject exist [43; 44]. This critical lack of research on brass alloys, their use in production and their applications has created a knowledge gap. Knowledge is still needed about which mechanisms for machinability improvement are important, how the introduction of Pb to brass alloys facilitates producibility and machinability, whether this function can be replicated by other means, and the risks associated with using Pb-free alloys as regards component integrity and functionality.

Brass is highly recyclable. The 2020 sustainability report of the only Swedish raw material supplier of brass rods and ingots, Nordic Brass Gusum AB, claimed that close to 90 % of their production is based on secondary material (i.e., scrap material). The high degree of recycling is excellent from a sustainability point of view. However, the industry's shift towards Pb-free brass is creating challenges relating to the removal of Pb from existing secondary raw material, separating the material flow of Pb-free alloys and alloys with high Pb content, and economical and sustainable recycling of Pb-free scrap, of which there is currently a low volume. Methods of separating Pb from the available scrap material or solutions for separate recycling of lead-free scrap are necessary for this type of production to be feasible.

A few methods of extracting Pb from molten brass do exist, although to the author's knowledge none of them are implemented on an industrial scale. Compound separation is based on forming Pb-rich compounds that are lighter than the molten brass and therefore float to the surface, forming a slag that can be skimmed from the melt, thus lowering the Pb content of the melt [45; 46]. The compounds added to the melt to form Pb-rich compounds are Ca or Ca-Si and NaF. In general fluorides are highly toxic, and industrial usage of the compound requires safety measures to ensure the health and safety of workers and to control emissions. As investigated by Hilgendof [47], fluorine-free separation methods are available, of which dilution is by far the simplest. By diluting the scrap with virgin material, the lead content can be reduced to below 0.1 wt.% over 5–10 dilution cycles. Dilution, however, requires large amounts of virgin Cu and Zn and does not solve the issue of the massive

amount of Pb-containing brass scrap that exists today. Other separation methods include electric pulse treatment [48], pyrometallurgical decomposition based on vacuum distillation [47] and electrolytic decomposition as patented by Grohbauer and Wieland-Werke AG [49]. The current lack of industrial Pb-removal options emphasises the need to recycle Pb-free alloys separately from their Pb-containing counterparts.

Based on the identified knowledge gaps, the goals of this dissertation are to create knowledge about the usage and producibility of components using Pb-free brass alloys, and to develop understanding of how Pb-free alloys can be machined in a similar or better fashion than brass with high Pb content.

1.5 Hypotheses

The following hypotheses are formulated for the dissertation:

1. The machinability of brass is a measurable metric that is dependent on the material's microstructure and properties as well as the applied machining conditions and strategies.

2. While undesirable from a sustainability perspective, lead in brass alloys has machinability enhancing outcomes.

3. Advanced material and process characterisation is able to explore and reveal mechanisms that control machining process outcomes and material machinability.

4. A combination of high temperature and high strain rate deformation can accelerate consolidation of powderised brass, so ensuring adequate microstructural and mechanical integrity of the resulting material.

1.6 Research Questions

Based on the hypothesis the following research questions can be formulated:

RQ1: Which mechanisms of machinability improvement are activated by the addition of Pb to brass alloys?

RQ2: Which of the identified machinability improvement mechanisms can be replicated in Pb-free alloys by microstructural features or machining strategy management?

RQ3: Can solid state recycling of machining-generated chips be a viable recycling system providing high utilisation of material and sufficient quality in components for their intended use?

1.7 Scope and limitations

The author's goal is to increase knowledge about Pb-free brass alloys and their behaviour both during the machining process and afterwards in their application, including management of the inevitable by-product of any machining process, chips. To realise this ambition, knowledge gaps in existing research are identified and addressed.

Machining processes includes several different input variables, including workpiece material, method selection, tooling solutions and cutting parameters. These input variables can be combined in an almost infinite number of ways. Therefore, certain limitations have to be set to be able to conduct research in the subject area. In the case of this dissertation, the following limitations were accepted:

- The dissertation deals with commercially available alloys, primarily those used for pipes and fittings. Several other brass alloys are used for other applications, but these are not considered in this work. In the dissertation, the chemical content of the materials used is also not altered outside of specifications for the alloys.

- A majority of the machining tests were performed in a laboratory environment, and only a smaller fraction of tests was performed in an industrial environment.

- When selecting machining operations, the focus was on longitudinal and orthogonal turning in laboratory tests, and was further extended to limited industrial trials using step drills and form tools. All laboratory machining tests were performed in dry conditions. The machinability assessment did not include tool life or tool wear tests because of prohibitive test times and workpiece material consumption in a laboratory environment.

- For solid state recycling, a more balanced combination of laboratory and industrial tests was performed. Solid state recycling using hot forging of pre-compacted chips was developed based on an original methodology. Therefore, benchmarking against other recycling techniques was not performed.

1.8 Research Methodology

The research questions posted in the dissertation are based on an identified lack of knowledge, from either an academic or industrial point of view. The starting point for research into Pb-free brass alloys is regulatory, driven by future regulation of the Pb content of components in certain applications. This has created interest in the subject, primarily driven by the manufacturing industry and supported by academia. Initial test manufacturing using Pb-free brass revealed that its broad implementation would entail increased cost of manufacturing [50]. To lessen the impact of the increased manufacturing cost, ways of utilising the workpiece material to a higher degree were investigated. This led to the idea of solid state recycling using pre-compacted metal cutting chips in hot forging operations. Solid state recycling is dependent on a well-functioning machining system, but in both industry and academia there is a lack of understanding of best practices and mechanisms contributing to the comparatively low machinability of Pb-free brass. Material characterisation and investigation of certain machinability aspects were done to increase understanding of the mechanism by which high Pb content provides brass alloys with improved machinability. The stated research questions are thus internally dependant and complementary in terms of their implementation in an industrial environment.

There are two main approaches to scientific research: induction and deduction. In inductive research, a theory is formulated based on a pattern observed in a large number of observations. For instance, in a purely inductive study to prove that low-cost airlines are subject to more delays than others, observations of 100 consecutive delayed low-cost airlines compared to 'normal' airline delays suggests a pattern supporting the theory that low-cost airlines are subject to more delays than other airlines. The conclusions do not, however, indicate whether your next flight with a low-cost airline is more or less likely to be delayed than the alternatives. Deductive research, by contrast, starts with a theory from which a rejectable hypothesis is formulated. Data is then collected and analysed to support or reject the hypothesis. Problems arise in deductive research when there is no existing theory on the basis of which to formulate a hypothesis, and the method can be too rigid to answer complicated questions. In research on engineering and applied subjects, both methods are commonly used in the combination known as hypo-deductive research. In hypo-deductive research, an inductive study can be followed by deductive research to confirm or disprove the conclusions from the inductive study. To reduce the number of observations needed and to help disprove or confirm theories, strategic management of the studied environment (i.e., experiments) can be an effective tool [51].

Throughout the dissertation, various research methodologies have been applied, based on the needs of the individual studies. Since no alloying developmental work is included in the dissertation, the material characterisation in section 2 is purely

observational. In that section, methods and techniques are applied to highlight the difference between materials. When characterising one of the materials, it was found that one of its phases is insufficiently described in the literature, leading to an expanded study of its crystallographic characteristics. This example highlights the need for research to be iterative, based on previously unknown facts. The results of the material characterisation are an important step towards answering RQ1 and RQ2.

In section 3, a hypo-deductive approach was used. In machining, the almost infinite number of possible processes and process conditions makes it necessary to limit the variability in order to be able to draw any conclusions. Such limitations also allow for experiments to isolate effects and causes. Some of the results in this section are based on observations, presented as polar diagrams to assess the material's potential machinability. Some results are based on experiments, most clearly those in section 3.3 which describes and explains the machinability enhancing effect of Pb in brass alloys.

The methodology used in section 4 to answer RQ 3 is less linear since it describes the development of a new recycling method. Because the method is novel, there is little literature describing similar processes. The work began with a feasibility study to investigate whether continuing developmental work was justified. It continued with a parameter optimisation study to improve the process and with life cycle assessment to quantify the sustainability and environmental impact of the proposed method. Some of the developmental work would, in retrospect, have benefited from a more defined design of the experiments to limit the number of tests needed to optimise the process and allow for optimising more parameters to a similar cost of resources. On the other hand, the number of tests conducted increases the robustness of the investigation, which is valuable in developmental work and builds trust for its further industrial implementation.

2 Characterization of brass alloys

Brass is a common engineering material used when high corrosion resistance, good electric conductivity and good manufacturability are needed. These properties are a function of several mechanical, thermal, and electrical properties that can be modified by adding other alloying elements or changing the balance between Cu and Zn. Alloys with Zn content up to 45 wt.% are the most used for engineering purposes. Common application areas include, but are not restricted to, pipes and fittings for water applications, small fastening elements, electrical connectors, and musical instruments. Brasses with higher Zn content are often called 'white brass' due to their colour and are often too brittle to see much use.

In this section the mechanical and thermal properties of several commercially available brasses will be examined and combined for estimating their potential machinability, thus bridging to subsequent machining-based studies.

2.1 Microstructure and chemical composition

Since the major alloying elements of brass are Cu and Zn, it is necessary to consider the equilibrium phase diagram for the system (Figure 2.1). The commonly used brass alloys are found on the copper rich side of the phase diagram and contain the α- and β-phases found in Table 2.1. When the β-phase is below 450 °C, it changes its atomic arrangement and chemical composition slightly into the β′-phase via a diffusionless phase transformation [52; 53].

Table 2.1. Phases found in brass alloys [54; 55].

	Standard Formula	Structure class (space group)	Lattice parameter [Å]
α – phase	$Cu_{0.67}Zn_{0.33}$	Fm-3m (225)	a=b=c=3.70
β – phase	$Cu_{0.53}Zn_{0.47}$	Im-3m (229)	a=b=c=2.96
β′ – phase	CuZn	Pm-3m (221)	a=b=c=2.96
γ – phase	Cu_5Zn_8	I-43m (217)	a=b=c=8.87
δ – phase	$Cu_{0.7}Zn_{0.2}$	P-6m2 (187)	a=b=4.28, c=2.59
ε – phase	$Cu_{0.2}Zn_{0.8}$	$P6_3/mmc$ (194)	a=b=2.74, c=4.29
η – phase	Zn	$P6_3/mmc$ (194)	a=b=2.68, c=4.83
Pb	Pb	Fm-3m (225)	a=b=c=4.95
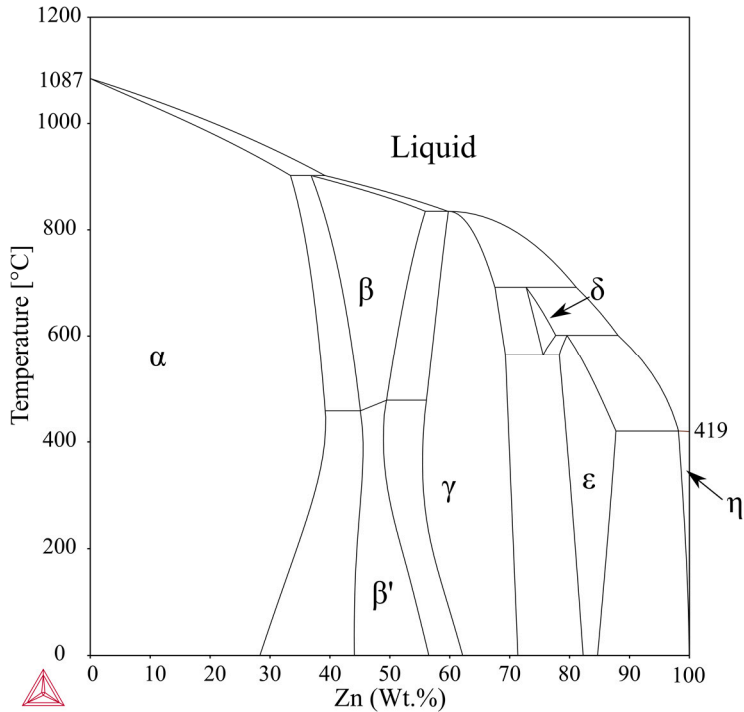
Figure 2.1. Phase diagram for Cu-Zn. [54; 56]

The materials used throughout this dissertation are commercially available alloys that include more constituents than shown in the phase diagram, see Table 2.2. Even small additions of certain elements alter the material properties; for example, adding small quantities of iron or aluminium increases the material's strength, and adding arsenic or tin increases its corrosion resistance [57; 58].

Table 2.2. Measured composition for materials used in this dissertation.

Alloy	EN code	Type	Cu	Zn	Pb	Sn	Fe	Al	Si	As
CuZn42	CW510L	α-β′	Rest.	42.2	0.1	0.02	0.09	-	-	0.01
CuZn38As	CW511L	α	Rest.	37.1	0.12	0.02	0.07	0.02	0.02	0.06
CuZn38Pb3	CW614N	α-β′ - Pb	Rest.	38.8	3.3	0.15	0.19	0.03	0.02	0.03
CuZn35Pb1.5Al As	CW625N	α - Pb	Rest.	34.8	1.2	0.06	0.11	0.5	0.02	0.03
CuZn21Si3P	CW724R	α-κ′[1]	Rest.	20.9	0.02	0.03	0.08	0.07	3.2	0.02

---

[1] See section 2.3 for more details.

The microstructure of materials extracted from extruded bars intended to be used in manufacturing is shown in Figure 2.2 to Figure 2.6. The images were made using electron backscatter diffraction (EBSD), which is a microscopy method capable of distinguishing between different crystal structures [59]. Since the material is extruded, its grain structure is elongated in the extrusion direction. All samples were cut in the same direction. In the IPF colouring images, X0 is along the extrusion direction and Z0 is transverse to the extrusion direction.

CuZn42, shown in Figure 2.2, has a lamellar structure where the β′-phase has precipitated after solidification. No continuous β-regions are found in the sample, which is good from a corrosion prevention point of view since the β′-phase is more susceptible to corrosion via dezincification than the α-phase [57]. The grain size of CuZn42 is larger than that of the other materials, around 500 μm compared to 70–20 μm for the other materials.

Two of the materials, CuZn38As and CuZn35Pb1.5AlAs, are almost purely α-phased material, with the exemption of Pb for CuZn35Pb1.5AlAs (Figure 2.5).

In the materials with high Pb content, CuZn38Pb3 and CuZn35Pb1.5AlAs, separated globules of lead are shown in black (Figure 2.4 and Figure 2.5). Pb is soluble in both Cu and Zn in the liquid state, but when the materials are solidified, Pb is almost insoluble in the present phases. The melting point of Pb ($T_{melt,Pb} = 328$ °C [60]) is rather low compared to the other materials and, if given enough time, it will migrate to the grain boundaries and solidify there.
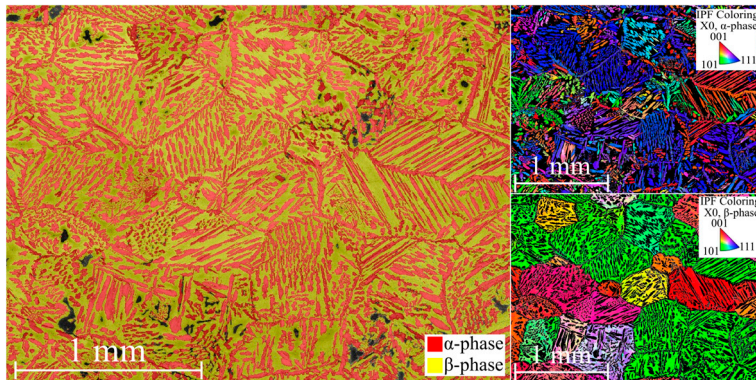
Figure 2.2. Image of the microstructure of CuZn42 from electron backscatter diffraction (EBSD).
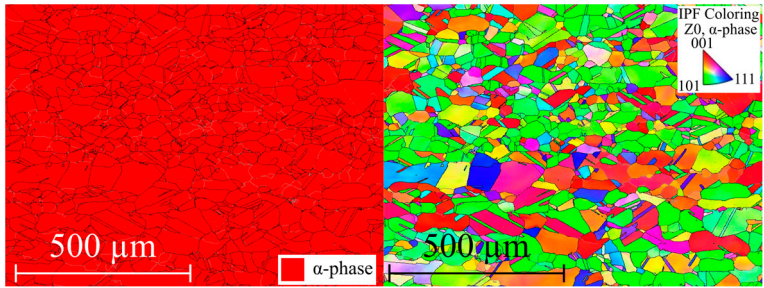
Figure 2.3. Image of the microstructure of CuZn38As from EBSD.
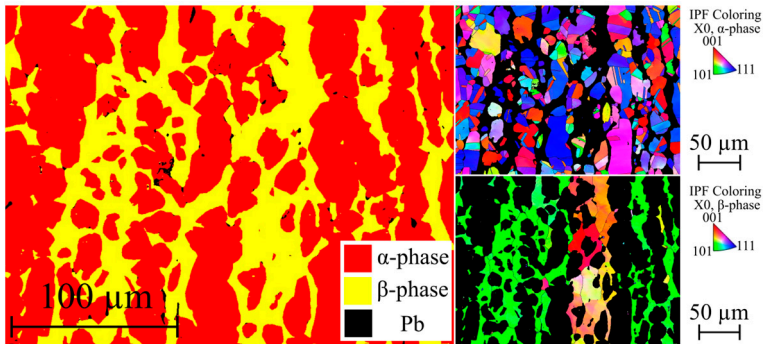
Figure 2.4. Image of the microstructure of CuZn38Pb3 from EBSD.
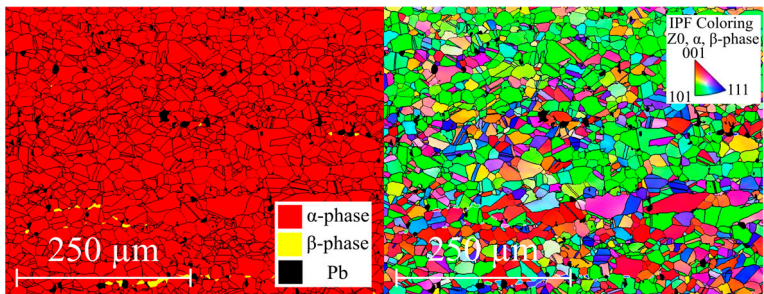
Figure 2.5. Image of the microstructure of CuZn35Pb1.5AlAs from EBSD.
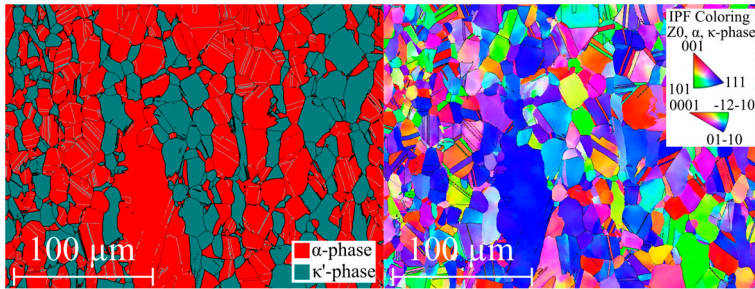
Figure 2.6. Image of the microstructure of CuZn21Si3P from EBSD.

2.2 Thermo-mechanical properties

A key element of this dissertation is that all brass alloys are different not only microstructurally, but also have significantly differing material properties. This will be demonstrated in the following sections by employing different standardised tests to characterise the thermo-mechanical properties of the chosen alloys.

2.2.1 Tensile testing

Tensile testing is one of the most common ways of reporting a material's mechanical properties. It is useful when determining static mechanical properties that are similar to the loading case of many components in use, such as proof strength, and for determining the breaking point for materials.

In tensile testing, a test piece of a certain geometry is clamped between a moving jaw and a fixed jaw. The moving jaw moves away from the fixed jaw at a predetermined rate and thereby creates tension in the specimen until the test piece breaks. During the test, the applied load and elongation of the test piece are measured. These values are recalculated into stress and strain to make the numbers independent of specimen size. The stress and strain can be calculated in two different ways, true stress/strain or engineering stress/strain. For true stress/strain the sample's instantaneous area is used to calculate the values, while for engineering stress/strain the original undeformed area is used. To make tensile tests comparable, standardised test methods are available. The test methods specify details of the test procedure (e.g., sample geometry and preparation) and the separation speed between the jaws. In general, the deformation rate specified for tensile tests is low.

The result of tensile testing indicates how much the material can elongate before it breaks and at what stress it starts to deform elastically and plastically. In the elastic region, stress and strain have a linear dependency but when the sample is further deformed, the relationship between stress and strain will no longer be linear.

The stress strain curves shown in Figure 2.7 are measured in accordance with ISO 6892-1 and show the average curves of three tensile test (blue line) and ± one standard deviation from the average curve (dashed red lines). To avoid strain hardening effects in the samples before testing, rods were annealed before being cut into flat test pieces using electric discharge machining (EDM). As the tensile testing machine used for the test did not have the capability to use different deformation rates in the elastic and plastic regions, the deformation rate was set to 0.00025 s^{-1} over the entire test series. All values in this dissertation for both stress and strain are engineering stress/strain, as opposed to the values shown in Paper I, where true stress/strain is used.
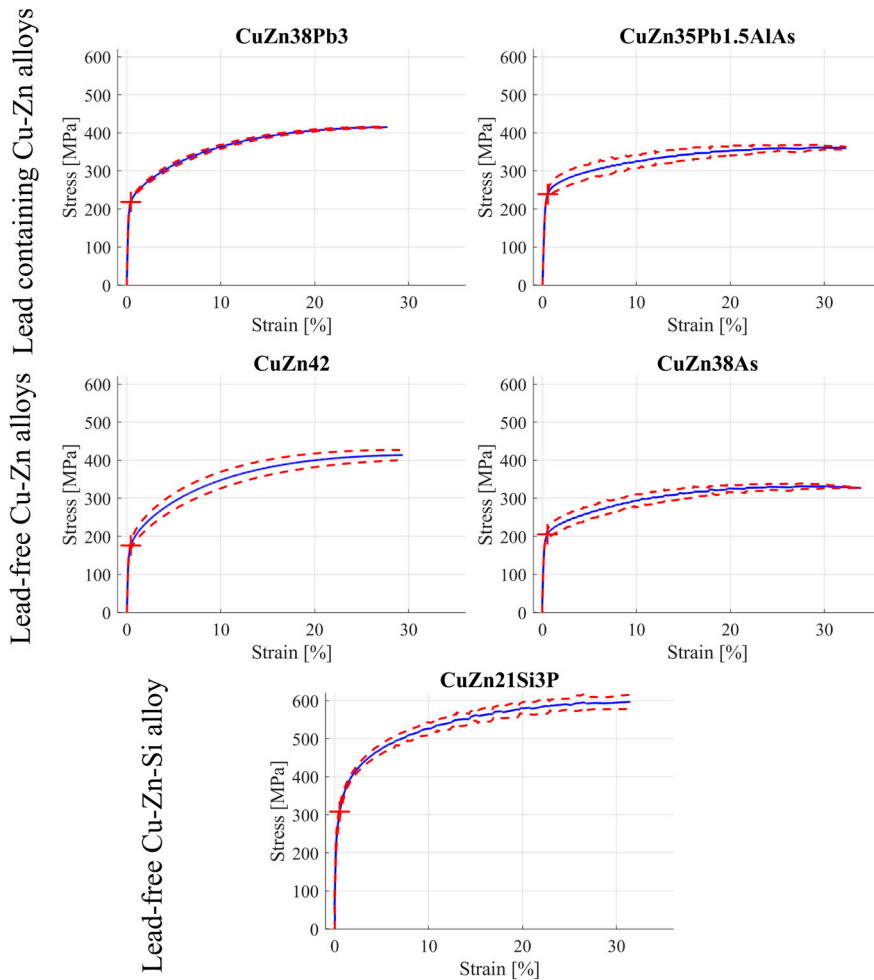
Figure 2.7. Stress-strain curves for tensile tests. The blue line shows the average result of three tests and the dashed red lines show ± one standard deviation. The red cross marks the proof strength (R_{p02}).

The results from tensile testing of the different alloys show that the α-alloys (CuZn35Pb1.5AlAs and CuZn38As) have fairly similar mechanical properties and α-β′-alloys have comparable properties, irrespective of Pb content. The α-alloys are more ductile than the other tested alloys, as shown by larger strain at breakage. CuZn21Si3P has approximately 50 % higher proof strength and ultimate strength compared to the other alloys.

2.2.2   Hardness

A material's hardness is described by its resistance to localised deformation. The hardness value of a material indicates its wear resistance [61] and is also closely related to its machining properties, such as cutting resistance [62] and tool wear [63]. There are many standardised methods of measuring hardness based on applying force with a hard object of well-defined geometry, commonly known as an indenter, and assigning hardness values corresponding to different scales. Examples of hardness scales include the Brinell (HB), Rockwell (HR), Vickers (HV) and Berkovich scales. Conversion between the different hardness scales is very complex and should be done with caution and interpreted as indicative values [64]. Different aspects of the material's hardness are measured depending on the applied load and geometry of the indenter. High load hardness testing shows the macrohardness and low load testing shows micro- to nanohardness. In the case of crystalline materials such as metals, the hardness can vary locally depending on microstructure and deformation history. These local differences will naturally be more obvious the smaller the indent.

Vickers hardness is one of the most used hardness scales for metallic materials. For Vickers hardness measurements, a diamond indenter in the shape of a right pyramid with a square base and an angle of 136 ° between opposite faces at the vertex is forced into the test piece. The diagonal lengths of the imprint left in the surface after unloading are then measured. The hardness number is calculated by dividing the test force by the area of the sloped surface of the indentation, which is assumed to have the same geometry as the indenter. In this dissertation macrohardness measurements were performed in accordance with ISO 6507-1 using a 5-kg load (nominal value of the test force $F = 49.03$ N). The resulting hardness values and standard deviation of five tests can be seen in Table 2.3.

The alloys that mainly consist of α-phase (CuZn38As and CuZn35Pb1.5AlAs) have the lowest hardness values. Single phase materials often have low hardness and, as seen in tensile testing, low strength and high ductility. CuZn42 has higher hardness than the other α-β′ alloy CuZn38Pb3, which may be related to its lamellar microstructure, shown in Figure 2.2. The hardest of the tested alloys is CuZn21Si3P with 176 HV5. This correlates with the tensile tests shown in Figure 2.7 where this alloy shows higher strength compared the other alloys.

Table 2.3. The average of five measured hardness values HV5 and the standard deviation for the set.

	HV5	Standard deviation
CuZn42	144.6	1.44
CuZn38As	95.7	0.53
CuZn38Pb3	127.2	2.03
CuZn35Pb1.5AlAs	104.8	1.72
CuZn21Si3P	176.4	1.86

Nano or microhardness measurements can be used to understand the differences in hardness between different phases in the materials. ISO 14577 defines under which terminology hardness measurements should be categorized, see Table 2.4. When using small loads for micro- and nanohardness measurements, the elastic properties of the test material will affect the size of the indentation after unloading to a higher degree than in macrohardness testing. To avoid the influence of elastic deformation and influence of the high-resolution microscope needed to measure the indentation, it is common to record a load-displacement curve during loading and unloading for calculation of the hardness values. A method for calculating the hardness value based on indentation depth was developed by Oliver and Pharr [65].

Table 2.4. Definition of hardness ranges according to ISO 14577. F is the indentation load and h is the depth of the resulting indentation.

Macro range	Micro range	Nano range
$2\,N \leq F \leq 30\,kN$	$2\,N > F$; $h > 0.2\,\mu m$	$h \leq 0.2\,\mu m$

When performing nano- and microhardness measurements it is extremely important that the sample surface be smooth and free of defects induced by sample preparation. If not, it is impossible to distinguish between the effects of poor sample quality and the actual hardness of the test material.

To characterize the material's microhardness, a 20x20 matrix of indents with a load of 50 mN using a Berkovich indenter was measured, see Figure 2.8. The indentation depth for the tests was 0.7–1.5 µm. As expected from the macrohardness tests shown in Table 2.3, CuZn38Pb3 has lower microhardness than CuZn21Si3P.
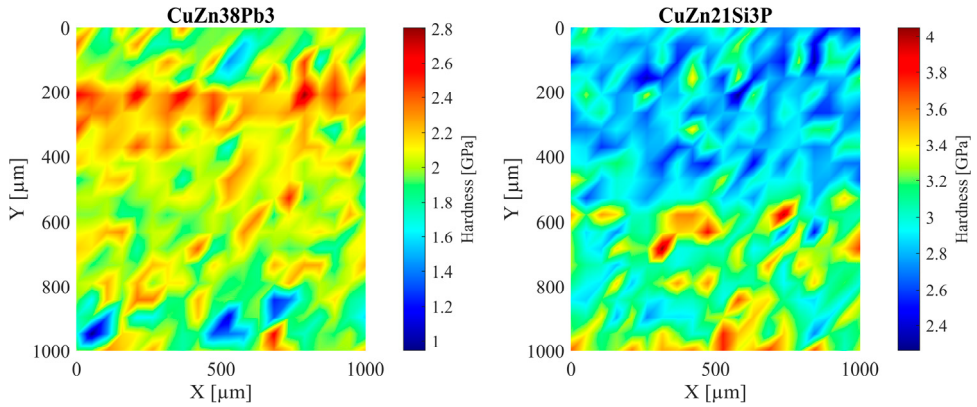
Figure 2.8. Examples of hardness measured in a 20x20 matrix using a Berkovich indenter and 50 mN load. Note the difference in hardness scale between the materials.
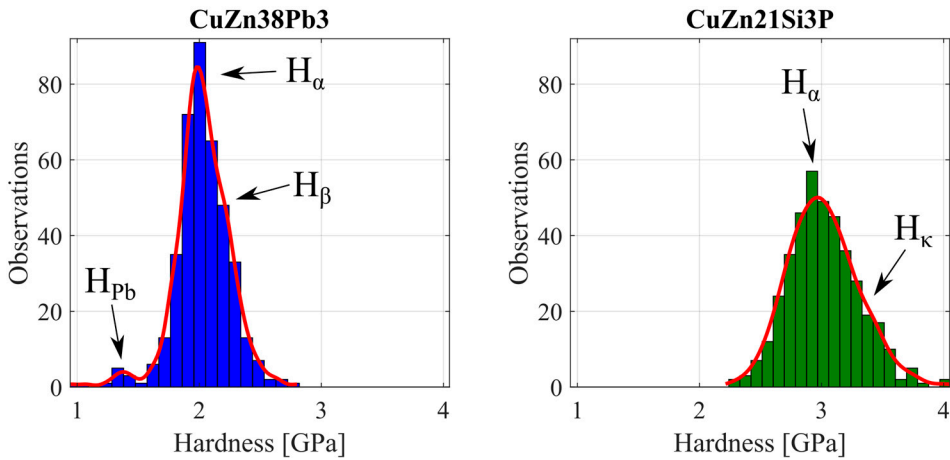
Figure 2.9. Distribution of microhardness for CuZn38Pb3 and CuZn21Si3P with the approximate hardness for the different phases marked.

By making a histogram of the obtained hardness values and fitting a non-parametric distribution to the histogram, the microhardness for the different phases can be identified, as seen in Figure 2.9. If the material contains only one phase, the distribution function fitted would be expected to be symmetric around the average microhardness for the phase. The fitted distribution function for CuZn21Si3P is slightly skewed due to the higher hardness in the κ′-phase. A small peak can be seen around 1.4 GPa for CuZn38Pb3, indicating the low hardness of Pb globules in the material.

2.2.3 Thermal conductivity

Light flash analysis (LFA) is a fast, non-destructive, non-contact, and absolute method for determining the thermophysical properties of a material, such as its thermal diffusivity (a), specific heat capacity at constant pressure (c_p) and thermal conductivity (K_w).

The measurements of thermal conductivity for the alloys were made using an LFA system, 467 HT HyperFlash made by Netzsch. The LFA system can perform measurements up to 1250 °C in different defined atmospheres. A vacuum-tight platinum furnace allows for heating rates up to 50 °C/min. The LFA system used is designed for sample dimensions of 12.7 mm (cylindrical) and 10 mm (cylindrical or square) with an integrated sample changer for up to four samples.

The front surface of a plane-parallel sample is heated by a short energy light pulse. Thermal diffusivity can be determined from the resulting temperature rise of the rear face as measured by an infrared (IR) detector. If a reference specimen is used, specific heat can also be determined. Combining these thermophysical properties with the density of the sample enables thermal conductivity to be calculated as a function of temperature, as shown in (1), where K_w is the thermal conductivity [W/(m·K)]; a is thermal diffusivity [mm²/s]; c_p is the specific heat capacity at constant pressure [J/(g·K)]; ρ is the bulk density [g/cm³].

$$K_w(T) = a(T) \cdot c_p(T) \cdot \rho(T) \tag{1}$$

The results of the LFA measurements are presented in Table 2.5. The measurements were conducted at 100 °C and 300 °C since this is the temperature range when machining brass alloys. More information about tool temperature can be found in section 3.2.2. The samples used were plane-parallel cylinders, Ø 10 mm x 2 mm, that were cut from rods using EDM to avoid mechanical deformation. The reference sample for the measurements was a pure Cu sample.

Table 2.5. Thermal conductivity at 100 °C and 300 °C for the different brass alloys.

	K_w (100 °C) [W/mK]	K_w (300°C) [W/mK]
CuZn42	144.3	167.4
CuZn38As	142.9	149.5
CuZn38Pb3	113.1	140.1
CuZn35Pb1.5AlAs	134.0	153.3
CuZn21Si3P	37.9	59.7

The materials all have similar thermal conductivity, apart from CuZn21Si3P, which shows significantly lower conductivity. At 100 °C, the other alloys have more than three times higher thermal conductivity than CuZn21Si3P. The difference may be related to microstructural differences between the materials.

2.2.4 Impact toughness

The Charpy test (named after the French scientist Georges Charpy) was introduced early in the 20th century to help correlate dynamic and static material testing results [66]. Unlike tensile testing, where the elongation and application of force is slow, the force in a Charpy test is applied by releasing a pendulum that hits a notched test piece. The test piece breaks when impacted by the pendulum and the pendulum's energy loss in the impact is measured. By applying the force to the test piece as an impact, less time is given for elastic deformation and dislocation movement. The strain rate in a Charpy test is between 10^{-1}–10^4 s^{-1} as reported by Lucon [67]. More sophisticated methods for measuring high strain rate properties of metals are also available (e.g., the split Hopkinson pressure bar), but Charpy tests give a good indication of a material's impact toughness.

Charpy impact testing was performed in accordance with SS EN ISO 148-1:2016 at room temperature. The test pieces had a quadratic cross section with a side length of 5 mm with a V-notch of 2 mm. The test was repeated five times for each material. The results are shown in Table 2.6.

Table 2.6. Average values of five Charpy tests and standard deviation for the test set.

	H_{V5} [kJ/m^2]	Standard deviation
CuZn42	278.5	19.5
CuZn38As	452.7	54.3
CuZn38Pb3	62.7	2.9
CuZn35Pb1.5AlAs	159.5	10.4
CuZn21Si3P	92.8	5.9

In tensile testing the α-β′ and α type materials performed similarly regardless of lead content, but the leaded materials have significantly lower impact toughness than their lead-free counterparts. For the two α–alloys, CuZn38As has three times higher impact toughness than CuZn35Pb1.5AlAs. CuZn38Pb3 has the highest Pb content and also the lowest impact toughness. There are, of course, more differences between the materials than only the Pb content. CuZn21Si3P silicon brass has second lowest impact toughness, which is likely related to its microstructural differences to the rest of brass alloys that are of α-β′ or α type.

2.3 Characterization of phases in Si-brass

CuZn21SiP differs greatly from the other brass alloys. It has substantially higher strength and hardness but lower thermal conductivity than the other alloys.

The phases found in CuZn21Si3P differ from those found in the other brass alloys that consist mainly of Cu and Zn. In machinability studies for CuZn21Si3P, several authors have reported that the material contains two phases, α-phase and κ-phase, without elaborating on which material system these abbreviations refer to [33-35; 68; 69], thus making the references incomplete. The high Si content appears to introduce an additional phase to an alloy that would be regarded as single phase if one consulted only the binary phase diagram for the alloy's major alloying elements, Cu and Zn, shown in Figure 2.1. Since the Si content seems to promote formation of a secondary phase in the material, it is necessary to consult the diagram for the ternary Cu-Zn-Si system. This system was thoroughly investigated by Wang et al. [56] and Borggren and Selleby [70]. Based on the composition of CuZn21Si3P and results presented by Wang et al., the κ-phase referred to by several authors should be a hexagonal phase in the Cu-Si system with the standard formula Cu_7Si [71; 72]. Cu_7Si has a hexagonal structure and belongs to the space group $P6_3/mmc$ (194) with the lattice parameters a = b = 2.56 Å and c = 4.18 Å. However, the phase is not stable below 500 °C, where it transforms into a cubic phase with the standard formula Cu_5Si and pure Cu according to the phase diagram reported by Springer Materials [73-75].

When investigating the residual stresses induced by machining, Tam, et al. [76] concluded that the material contains two phases: one very similar to the earlier described α-phase in the Cu-Zn binary system, and the other being a hexagonal phase. The hexagonal phase did not match any of the phases registered in the reference databank (PDF4+, 2014, International Centre for Diffraction Data) but calculations showed that the diffraction pattern matches space group $P6_3/mmc$ (194) with the lattice parameters a = b = 2.594 Å and c = 4.21 Å. It is highly unusual for phases in commercially available alloys not to match any of the registered phases in well-established databanks such as PDF4+.

After examining CuZn21Si3P using reflectance powder x-ray diffraction (XRD), Figure 2.10, the conclusions drawn by Tam, et al. were verified; no matching phases were found in the reference databank. Even though no match could be found for the phase in the reference databank, the diffraction pattern from XRD confirms that the phase is hexagonal with lattice parameters close to those reported for the κ-phase, but the measured diffraction pattern does not fit with the expected pattern for the κ-phase. Further examination of the diffraction pattern shows that the peaks that are not associated with the α-phase match the space group $P6_3/mmc$ (194) with lattice parameters a = b = 2.59 Å and c = 4.22 Å, Figure 2.10. Hence, the phase will be called κ′.

As previously mentioned, the κ-phase is not stable at room temperature. To determine whether the phase was retained in an undercooled state, a piece of CuZn21Si3P was annealed at 600 °C for 4 hours before the oven was turned off and the sample was allowed to cool slowly inside the oven. The annealing did not change

the diffraction pattern from XRD, thus confirming that occurrence of the phase is not an effect of rapid cooling.
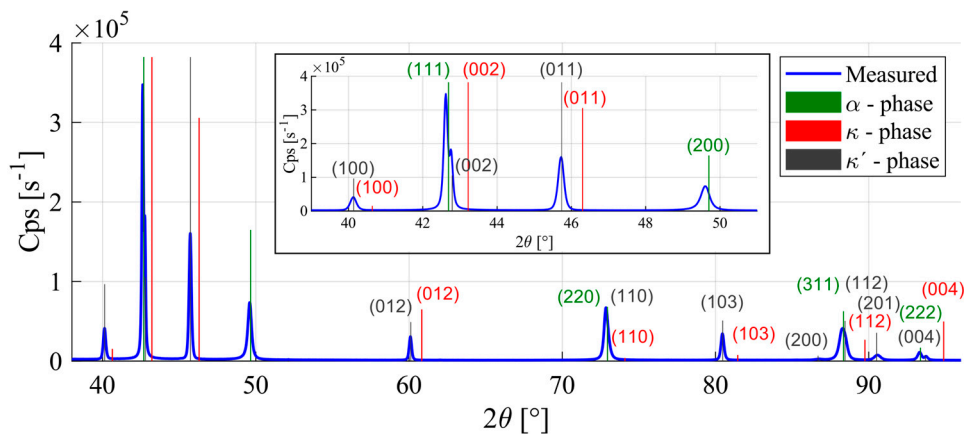
Figure 2.10. Diffraction pattern from XRD with theoretical peak locations indicated for certain phases.

To further examine the hexagonal phase, a small specimen suitable for transmission electron microscopy (TEM) was prepared using a focused ion beam (FIB) lift-out procedure similar to that described by Giannuzzi and Stevie [77]. EBSD mapping was first used to identify a large region of pure κ′-phase from which the TEM specimen was then extracted, see Figure 2.11.
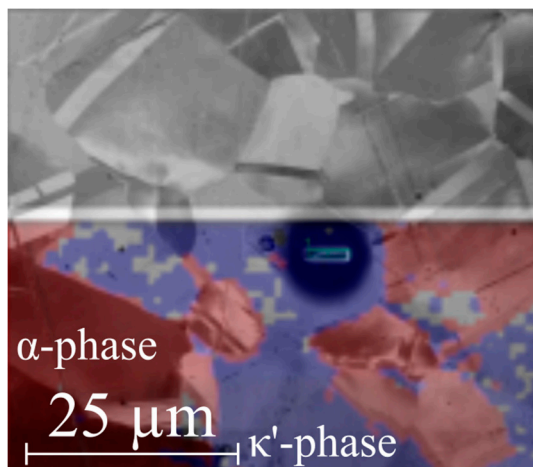
Figure 2.11. Combination of images from EBSD for identification of a large κ′-grain and FIB-milling for extraction of a TEM lamella from a single grain of the κ′-phase.

Since the TEM specimen was extracted from within one grain of κ′-phase, the TEM selected area electron diffraction (SAED) provided single crystal diffraction data, instead of the diffraction rings typical of powder XRD. Using a rotatable specimen holder in the TEM, single crystal diffraction patterns could be obtained from multiple orientations. Figure 2.12 shows such two diffraction patterns. Comparing the measurements obtained from SAED with simulated electron diffraction patterns indicates that these measurements reinforce the hypothesis that the κ′-phase crystal structure has the $P6_3/mmc$ (194) space group with lattice parameters a = b = 2.59 Å, c = 4.22 Å.
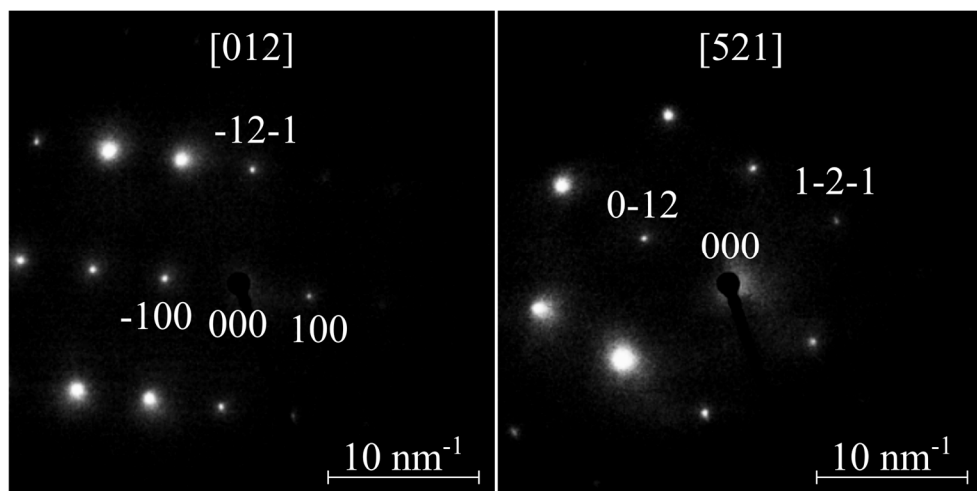
Figure 2.12. Single crystal diffraction patterns from SAED.

The results of the investigations on the hexagonal phase are, in part, inconclusive. The phase structure is determined by electron diffraction, and the chemical composition is estimated by SEM XEDS and provided in Table 2.7. It is, however, not clear whether the accuracy of SEM XEDS is sufficiently high to determine the phase composition as the stoichiometry calculations differed slightly from region to region.

Table 2.7. The chemical composition of the two different phases in CuZn21Si3P, measured using SEM XEDS.

(wt.%)	Cu	Zn	Si
α - phase	75.9	21.1	3.1
κ′ - phase	76.8	18.6	4.6

All measurements on the phase were done using commercially available material that contains several alloying elements other than Cu, Zn and Si. Even minor changes in chemical composition can influence the phases found in a material. For

further investigation of the κ′-phase, it is recommended that the material should be synthesised using elemental powders of high purity to exclude the influence of minor alloying elements. It is also of interest to determine the chemical composition of the phases in CuZn21Si3P with high accuracy to increase knowledge about the alloy.

From a manufacturing technology point of view, the practical significance of knowing the phase structure of a material is perhaps minor, but is noteworthy that so little information is available about a phase occurring in a commercially available material. A researcher more versed in material science might be able to decide whether this is indeed a new phase or a variant of the κ-phase from the Cu-Si system, stabilised at room temperature by Zn or minor alloying elements.

2.4 Conclusions

This section has shown that brass alloys have different thermo-mechanical properties depending on their chemical composition and microstructure. Although this may not be a ground-breaking discovery, it is important to consider this point when changing the material used for a component as any change may affect the intended manufacturing system for the product or the functionality of the component.

Given that alloys with high Pb content are being phased out, redesign of components will be necessary. Such redesign will be costly for the manufacturing industry, but it also presents opportunities. One of the Pb-free alternatives for replacing components made using alloys with high lead content, CuZn21Si3P, has substantially higher strength than the other alloys. This increased strength can be used to make components of equal strength using less material. The cost of material will thus decrease compared to purely switching materials without redesign.

It is also important to consider the differences in material properties when machining Pb-free alloys. In tensile testing, the mechanical properties for α- and α-β′ alloys are similar, but using higher strain rates, as in the Charpy-test, highlighted the differences between them.

3 Machining of brass alloys

Manufacturing of components in brass is characterised by short cycle times and oftentimes multi-spindle bar fed machines with complex cutting tools are used to generate several surfaces on the manufactured part simultaneously. The complex tools make it possible to remove much material per time unit but since the tool engagement with the workpiece is very extensive, the process is sensitive to changes in machinability. By alloying brass with Pb, a very high machinability is achieved. Since Pb is hazardous and its use regulated in certain applications it is necessary to characterize alloys with low lead content to find suitable machining strategies for them.

In this chapter the machinability of commonly used brass alloys will be assessed and the influence subsurface deformation on corrosion resistance will be discussed.

3.1 Overview of machining processes

Machining is the generic term for manufacturing methods in which undesired material is mechanically removed from a workpiece in the form of chips to achieve the desired shape of the final component. It is one of the most widely used industrial manufacturing methods as it offers great freedom of form and high productivity.

The different machining processes can be divided into several categories depending on whether the process is continuous, whether one or more cutting edges are used, and whether the workpieces are continuous or intermittent. In continuous processes, the cutting tool will be in contact with the workpiece throughout the process. Depending on process characteristics, different requirements are placed on the cutting tool. The tool material in an intermittent process like milling must be more tough and impact resistant since it is periodically loaded and unloaded when it moves in and out of engagement with the workpiece. A continuous process like longitudinal turning places different demands on the tool's ability to withstand elevated temperatures. It needs to have higher abrasion resistance than tools used in milling, where the tool needs to withstand repeated loading and unloading cycles in combination with impacts that occur when the tool engages the workpiece.

Machining processes are often difficult to analyse with many factors and choices affecting the outcome. Turning is one of the easiest to analyse since it has a

stationary tool and continuous engagement with the workpiece, and it is one of the most used cutting processes in the manufacturing industry.

For longitudinal turning, the main orthogonal directions used to describe a turning operation are T in the tangential direction, A in the axial direction of the workpiece and R in the radial direction, see Figure 3.1. The cutting forces are commonly divided into force components associated with these directions (F_c, F_f, F_p). Removed material per time unit is determined by the cutting data parameters: cutting speed v_c, feed f and cutting depth a_p. Here v_c corresponds to the relative speed, commonly expressed in m/min between the cutting edge and the uncut surface of the workpiece, f is the tool's axial movement per rotation of the workpiece, and a_p represents the tool's radial engagement. The angular position of the cutting edge in the AR plane is described by the major cutting edge angle, κ, see Figure 3.1. The cutting data parameters and κ determine theoretical chip thickness h_1 and theoretical chip width b_1 according to equations (2) and (3), whose product approximately gives the theoretical chip area A, (4).
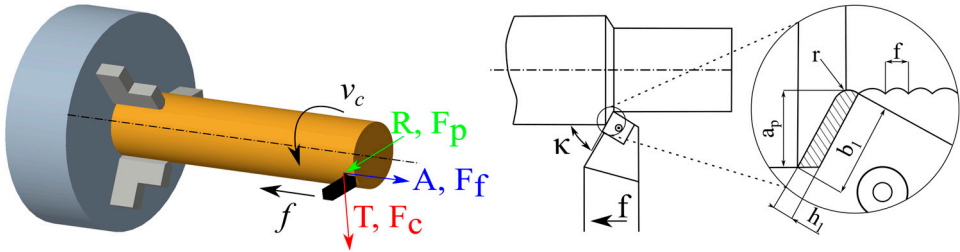
Figure 3.1. Definition of three orthogonal directions with respective force components in a longitudinal turning operation and the major chip area parameters, adapted from Ståhl [62].

$$h_1 \approx \sin(\kappa) \cdot f \qquad (2)$$

$$b_1 \approx \frac{a_p}{sin(\kappa)} \qquad (3)$$

$$A \approx b_1 \cdot h_1 \qquad (4)$$

The tool's geometry and angular position relative to the workpiece have a major impact on the cutting process. Depending on the goal of the operation, different choices need to be made to reflect different priorities. For example, if large amounts of material are to be removed as quickly as possible, tool strength needs to be prioritized over geometrical features promoting component's surface smoothness.

When a cutting tool is used, its geometry will change during its service lifetime. At the beginning of the tool's life, these changes are small, but depending on the

machining situation and engagement length, the changes may have a significant impact on the tool geometry. For example, some material may stick to the tool as a built-up edge (BUE) or layer (BUL) and then become part of the cutting tool geometry. The tool may become worn so that its effective clearance angle is smaller than intended, which means that a larger part of the tool's flank side is engaged in contact with the workpiece, eventually increasing the tool temperature, subsurface deformation and possibly promoting vibrations.
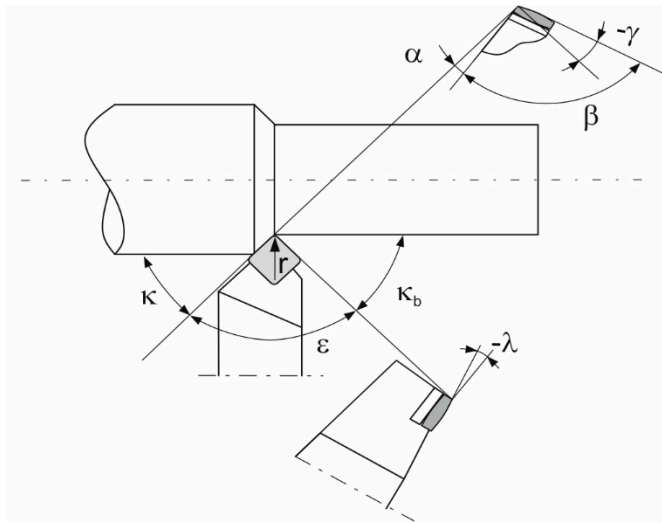
Figure 3.2. Definition of the cutting tool's macrogeometry, adopted from Ståhl [62] and based on original image from Vieregge [78].

A cutting tool's geometry can be divided into macro- and microgeometry depending on which part of the tool is referred to. The following description of tool geometries is not a result of research within the scope of the dissertation, but is important in all machining operations and is mainly adopted from Ståhl [62]. Similar explanations, with slightly different nomenclature, can be found in comprehensive books about metal cutting or respective standards [79; 80]. Examples of macrogeometry are the shape of the insert which can be, for instance, rhombic, square or round, the size of the nose radius and the rake angle of the tool, γ, see Figure 3.2. There are no absolute rules regarding which macrogeometry is suitable for individual applications, but some general conclusions can be drawn:

- A major cutting edge angle, κ, which is less than 90° means that the theoretical chip thickness, h_1, decreases but its width, b_1, increases compared to angles greater than 90°, according to (2) and (3) and Figure 3.3. In this case, the cutting force is spread over a larger length of the main cutting edge and gives a more favourable force distribution over the contact area. A smaller κ angle usually also leads to a better chip breaking and a

more favourable force distribution in the tool at the entrance to the workpiece.
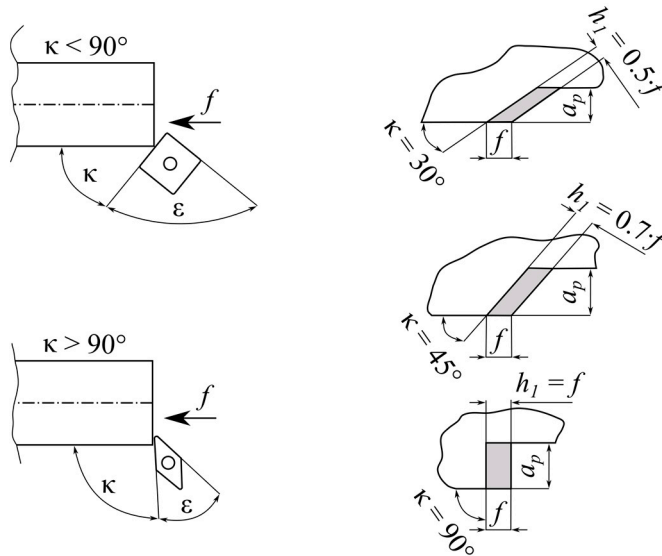
Figure 3.3. The influence of the major cutting edge angle, κ, on theoretical chip thickness, h_1. Adopted from Ståhl [62].

- The tool's nose radius, *r*, has a direct effect on the theoretical surface roughness after machining, the tool's contact length with the workpiece and the tool's load bearing capacity. Common sizes of the nose radii of standardized indexable inserts are 0.4, 0.8 and 1.2 mm. In theory, better surface roughness should be achieved by increasing *r*, but in practice the increasing contact length means that vibrations easily occur with a large nose radius. Therefore, tools with a smaller- or medium-sized nose radius are most often used for finishing. In the majority of finishing cases, the cutting depth is small, it is then often advantageous to choose a cutting insert with a nose radius that is smaller than the cutting depth.

- The inclination angle, λ, affects both cutting forces and chip curling and breaking. It can be greater than 0, and is then called positive, neutral (λ = 0) or negative. A negative inclination angle creates a more favourable load situation during tool's engagement in interrupted cutting, such as milling or sawing, because the rake face of the tool comes in contact with the workpiece and not the edge line, as is the case for a positive inclination angle. It also means that the chips are directed towards the unmachined part of the workpiece. This helps with chip breaking, decreases the risks of chip hammering on the tool, and redirects the chips from the finish-machined surface, hence preventing its scratching and chip re-welding.

- For a successful cutting process, only the part of the tool that contributes to chip removal, the rake face, must be in contact with the workpiece. Therefore, a clearance angle, α, is created on the tools to prevent a contact with the flank face. The angle can be obtained by the tool holder geometry or be built into the insert. If the as-sintered insert has no clearance angle, it is often possible to use more edges of the insert than if it has a built-in clearance angle, thus increasing tool utilization. At high feed, the effective clearance angle is reduced due to compliance of the workpiece. If too large a clearance angle is used, the strength of the insert decreases, but the risk of increased development of flank wear increases if a clearance angle is insufficiently large. The size of the clearance angle is also determined by whether internal or external machining is to be performed.

- Like α and λ, the rake angle, γ, can be achieved by a tool holder or is built into the insert. This γ angle affects, for example, the size of the cutting force and the radius of curvature of the chip. A positive rake angle gives a larger radius of curvature of the chip and reduces the cutting force but gives a weaker cutting edge. In intermittent machining, a negative rake angle is often used to better cope with the cyclic loads at the engagement and disengagement of the tool from the workpiece.
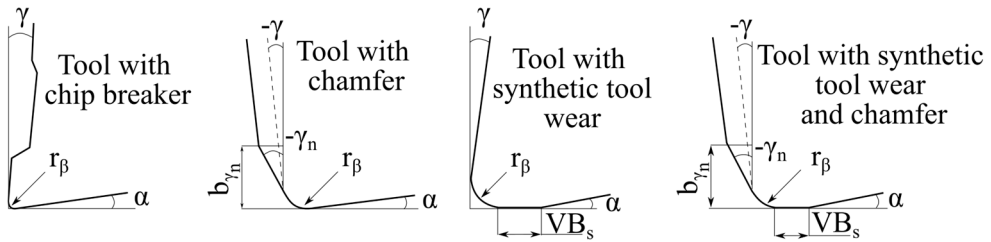
Figure 3.4. Examples of microgeometries of the cutting tool. Adopted from Ståhl [62].

Figure 3.4 shows examples of different microgeometries. The microgeometry of a tool explains what its edge line looks like. The design of the edge line has a great impact on the tool's strength and the properties of the machined surface. In the same way as for macrogeometry, there is no answer as to which microgeometry is 'best' as the requirements for the tool change depending on the machining case or situation.

- The edge radius, r_β, represents the junction of the rake and flank faces of the cutting tool, often in the form of a rounding. The edge radius is often not constant over the entire insert. Depending on how the insert has been made, the edge radius will vary slightly. In most cases, the edge radius is slightly larger at the tool's nose radius. A sharp tool (having a small edge radius) makes it possible to have a remove very small chip thickness (shallow cuts or small feed), which makes it suitable for finishing. Tools

with larger r_β are stronger and less sensitive to chipping. When machining brass, it has proved advantageous to use tools with small values of r_β.

- Chip breakers are often found in cutting tools and the purpose of these is, as the name suggests, to break the chip. They are often designed to reduce the radius of curvature of a chip and thus cause it to break against itself, against the cutting tool, or against the unmachined part of the workpiece. Improper chip breaker design redirects the chip onto the already machined surface. The chip breaker sometimes increases the contact length between the chip and the tool, which can lead to increased forces and tool temperatures.

- To get a stronger, more load-bearing edge line, a chamfer can be used. The chamfer is a local variation in the rake angle at the edge line. The chamfer is commonly between 0.05–0.20 mm in length and with, for example, $\gamma = 20\,°$, but the values depend on the application. This is common for inserts used for intermittent machining.

- In some machining cases, a synthetic flank wear, VB_s, has proven to provide advantageous force distribution between the flank and rake face. By increasing the mechanical load on the clearance side, high loads on the rake face can be balanced out and help avoid plastic deformation of the cutting edge.

3.1.1 Machinability

At first glance the concept of machinability seems quite straightforward: *How difficult is it to machine a certain material to the required specification?* However, the answer to the question will depend on the person answering it and their interests. If the person is, for instance, mainly concerned with the surface quality of the machined surface, the perception of machinability will be influenced by how easy it is to achieve a certain surface characteristic. Machinability is, furthermore, method dependant: a material that shows good machinability in a milling application may be difficult to machine using turning. In most fields of science and technology great care is devoted to the definition of relevant parameters, but in machining machinability tends to remain a loosely defined term without a universally accepted definition [81].

Machinability is not a well-defined or easily measurable parameter since it is a combination of many different attributes of both the workpiece material and machining system. Several different definitions of machinability exist derived from how a workpiece material can be machined. According to Shaw [79], machinability is a function of the workpiece material's chemistry, structure and compatibility with the tool material. A more economically oriented definition of machinability is

presented by Ståhl [62], who describes machinability as '*assessing the total cost of manufacturing a particular part in the manner aimed at, using the workpiece material in question.*'

In general, there are two types of machinability indexes: absolute and comparative. Absolute indexes use the workpiece material's physical properties and other measurements to calculate a number that describes machinability [82; 83]. Absolute numbers are easy to compare, but when combining as many factors as those influencing a material's machinability, information will inevitably be lost. Comparative indexes focus on comparing two or more materials under given experimental conditions.

One of the most reliable standardised machinability tests is ASTM E618. The scope of ASTM E618 is to evaluate the machinability of steels by ranking them to each other, but as demonstrated by Thiele et al. [84], the test is also suitable for other alloys such as brass. The test is intended to simulate mass production of parts based on manufacturing of a standardised component in a bar fed machine for eight hours using specified tools with a tool life of eight hours. Although it gives an accurate comparison between the machinability of different materials in actual production circumstances, a drawback of the test is the substantial amount of workpiece material and machine time used in the test, both in the actual test and in the calibration of the machining parameters for achieving a tool life of eight hours.

The most commonly used machinability rating systems for brass alloys are based on tool life. In this type of test, the time it takes for a tool to develop wear to a set criterion (e.g., VB = 0.3 mm) is measured in a specific machining operation for an alloy and compared to free-machining brass such as CuZn38Pb3 or UNS C36000 (CuZn36Pb3). The machinability rating is given as a percentage of the tool life measured for the free-machining alloy [85]. While a rating system based on tool life alone gives some valuable information, several key aspects of machining are overlooked, such as chip formation, quality of the produced component and power requirements to remove chips from the workpiece.

From material's perspective, the mechanical properties controlling machinability are hardness, strength, ductility, thermal conductivity, propensity for deformation hardening and inclusions of hard particles [80]. These attributes, directly and indirectly, lead to a specific tool life and surface finish as well as a certain power required to remove chips from the workpiece material with a specific tool.

3.1.2   Polar diagrams to assess the machinability of an alloy

A graphical, comparative method to assess the potential machinability of materials based on their thermo-mechanical properties was initially developed by Andersson and Ståhl [86] for steel alloys. By comparing the thermomechanical properties of an alloy with a reference material and plotting them in a polar diagram, it is possible to

assess the potential machinability of different materials where a small area in the polar diagram indicates high machinability compared to the reference material. The method was further developed by Xu et al. [87] and Olovsjö et al. [88] for nickel-based superalloys. The material properties considered in the method are:

Ductility: A material with high ductility can be difficult to cut due to strong adhesion on the cutting tool and burr formation, which is unfavourable in the machining process. Low ductility generally also promotes good chip breakage, which is advantageous from a manufacturing point of view.

Strain hardening: The energy required to remove a chip from the workpiece material is largely dependent on the material's ability to strain harden, which in turn leads to higher cutting forces. To simplify use of the model, the strain hardening factor of the workpiece material, S_n, is calculated as the ratio between the ultimate tensile strength, R_m, and the proof strength, $R_{p0.2}$, since these parameters are commonly found in material data sheets.

Thermal conductivity: Due to large plastic deformations and friction in the cutting zone, heat is generated in the machining process. If the heat is not dissipated in the chips and workpiece material, high temperatures can occur in the cutting zone, which can reduce the tool life due to decreased hardness and strength of the tool material and chemical wear. Thus, a high thermal conductivity increases machinability.

Hardness: The workpiece material's macrohardness significantly influences the cutting forces in the process. Machining materials with higher hardness is known to cause an increased forces and power consumption. Thus, high hardness implies lower machinability.

Abrasiveness: A workpiece material's abrasiveness is difficult to quantify, but it is an important parameter when assessing machinability. Abrasive wear generally occurs when the workpiece material contains hard particles or inclusions, such as carbides, but also if the material consists of multiple phases with different hardness. Ståhl [62] developed a method for quantifying the abrasiveness by using multiple nanohardness indentations, and this method was further developed by Chen [89]. The difference in nanohardness between phases, the volume fraction of each phase and the material's macrohardness are used to calculate the abrasiveness of materials.

For the brass materials used in this dissertation and for which the abrasiveness was evaluated, only small variations in hardness between the phases were measured. No hard particles, such as hard carbides, are either expected to be found in a copper or brass alloy. Hence, the parameter of abrasiveness might not be highly relevant for assessing the machinability of brass alloys.

It is worth noting that none of the previously presented properties takes rapid deformation, like that seen in metal cutting operations, into account. Therefore, a modified method of assessing the potential machinability of brass alloys is

presented, where abrasiveness is replaced by the impact toughness. This modification can better reflect the difference in machinability seen for brass alloys. Charpy impact testing is used to measure impact toughness, as described in section 2.2.4. The deformation rate in a Charpy test is similar in magnitude to metal cutting, $\dot{\varepsilon} \sim 10^{4} \text{ s}^{-1}$.

Since CuZn38Pb3 has long been one of the most used brass alloys in machining applications, it was chosen as reference material. Data from measurements reported in Chapter 2 are used to populate Table 3.1, which is used to construct the polar diagrams shown in Figure 3.5 and Figure 3.6. The reference material's properties are assigned the value 5 in the diagrams and maximum and minimum values for the properties are set. The other listed properties are compared to it and assigned a value based on the difference from the reference material's property in relation to the chosen maximum and minimum values, assigned according to the largest and smallest values in the dataset or according to user's experience.

Table 3.1. Values used for constructing polar diagram to assess the materials machinability.

Alloy	$S_n \left(\frac{R_m}{R_{p02}} \right)$	ε_b [%]	H [HV5]	W_{ab} [GPa]	K_w [W/mK]	K_{v5} [kJ/m²]
CuZn42	2.36	31.3	144.5	1.17	167.4	278.5
CuZn38As	1.63	36.0	95.7	-	149.5	308.6
CuZn39Pb3	1.91	29.4	130.9	1.15	140.1	62.7
CuZn35Pb1.5AlAs	1.52	36	104.8	-	153.3	159.5
CuZn21Si3P	2.11	34.8	176.4	1.41	59.7	92.8
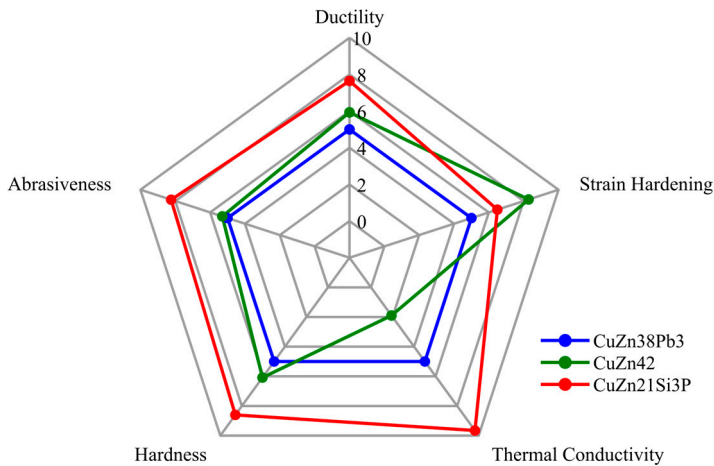
Figure 3.5. Polar diagram to asses the machinability of three different brass alloys using the method presented by Xu et al. [87] and property values from Table 3.1.
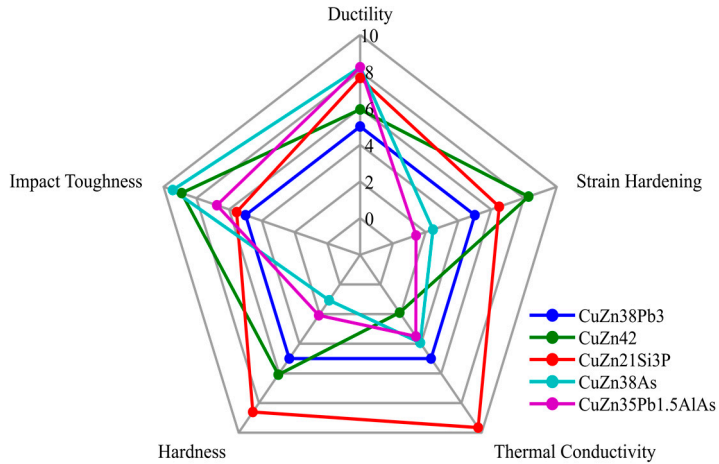
Figure 3.6. Modified polar diagram using impact toughness instead of abrasiveness to better describe the potential machinability of brass alloys.

3.1.3 Machining of brass alloys

Machining of brass can be considered a special case of machining. Due to the material's high machinability, form tools and step drills are commonly used in multi-spindle machines to manufacture components with extremely low cycle times, see Figure 3.7. Due to long tool life for the cutting tools used, the production can experience low disturbance and run almost without supervision which reduces the cost of personnel. This has, in part, been possible due to the enhanced machinability provided by alloying brass with Pb.
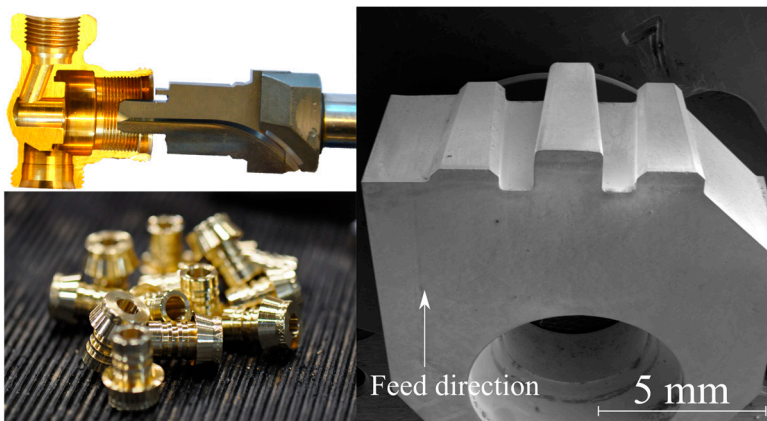
Figure 3.7. Examples of step drill and form tool used for making brass components.

When phasing out brass with high Pb content, the manufacturing industry faces challenges due to decreased machinability. The transition need not be too dramatic, but careful evaluation of production procedures is needed.

A production test for three different components in lead-free brass was set up, using the same tool and manufacturing setup as for production in brass with high Pb content. Two tonnes of CuZn42 and CuZn38As were used in the production test for three different parts. Before starting the test, issues were expected to occur related to tool life and chip formation.

In the initial stage of the production test, problems with vibrations and chip formation were resolved by adjusting the cutting data. For some operations with large problems in chip formation, pauses in the feed helped to break the chips that otherwise formed large nests that were difficult to evacuate from the machine and scratched the other components that were being manufactured simultaneously. Vibrations were avoided by decreasing the cutting speed and feed rate for the finishing operations.

Since tool life was identified as a potential problem in the production test, the tools used in the test were measured in a 3D-optical microscope (Alicona Infinite Focus G4) before and after use, to be able to evaluate the tool wear. The tool with the largest wear after the production test can be seen in Figure 3.8. The measured flank wear is low, but the tool is so large that even flank wear as small as $VB = 0.13$ mm changes the cutting conditions and introduces vibrations. When the tool is fully engaged, the length of the edge line in contact with the workpiece is more than 15 mm. When the contact area is so large, even small changes can have a major effect on the end result.
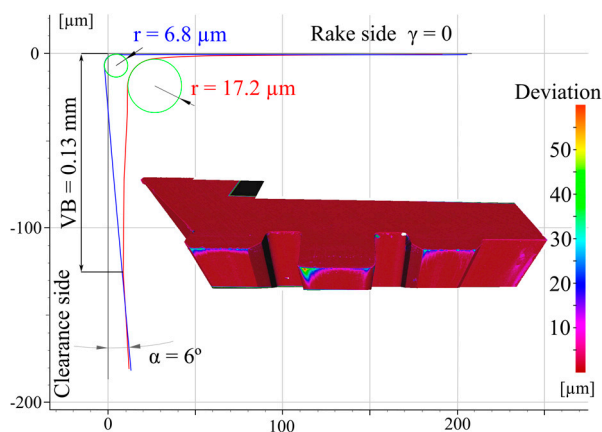
Figure 3.8. The volume difference measurement between a used and unused tool from the production test, illustrated by the colourmap 3D image, and cross-sectional profile of the edge line. The edge line is the most worn section of the tool, where the blue line shows the unused tool and the red line the worn tool.

Evaluation of tool wear and optimal cutting conditions are extremely difficult in actual production since the cutting conditions may not be the same even for an individual tool, as is shown in Figure 3.9. This makes it difficult to isolate the cause and effect of changes to the process to achieve optimal results. One of the products manufactured in the production test was a nut with an external chamfer. The starting material for production of the nut is a hexagonal rod. It is internally machined with drills, boring tools and a thread tap, while the outside of the part is chamfered with a coated cemented carbide insert. As is shown in Figure 3.10, the edge radius is larger (~ 35 µm) for the insert compared to the form tool (~7 µm) shown in Figure 3.8, and the inclination angle, λ, goes from positive near the nose radius to neutral in the middle of the insert. When fully engaged, the depth of cut for the insert is approximately 8 mm. Due to the large depth of cut, the middle part of the insert, where λ = 0, is also used. Since the workpiece is hexagonal, the insert will also experience intermittent contact and impacts during the machining.
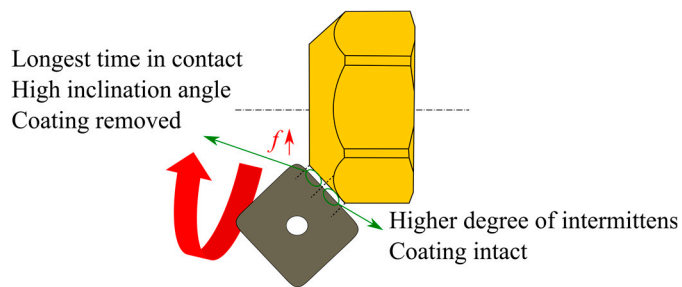
Figure 3.9. Description of the differences in cutting conditions for an insert used in production of a nut with a chamfer from hexagonal rod.
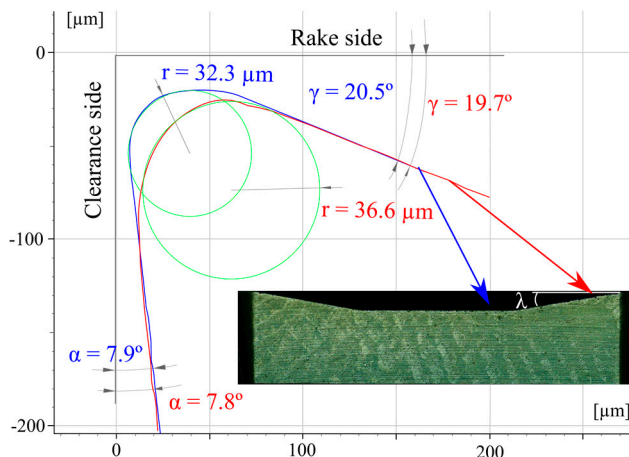
Figure 3.10. Differance in edge line and inclination angle, λ, for an insert used in the production test.

After the production test, the insert was examined in a SEM, where it was found that the coating had been worn off in the section of the tool that had the longest engagement time, see Figure 3.11. The coating used for the tool consists of two layers. A titanium-rich coating (titanium carbonitride) is situated closest to the cemented carbide substrate, and the upper layer is aluminum oxide with large concentrations of chromium as detected by XEDS. In the regions of the edge line where the coating is removed exposing the cemented carbide, an interesting ridge-like structure is discovered.
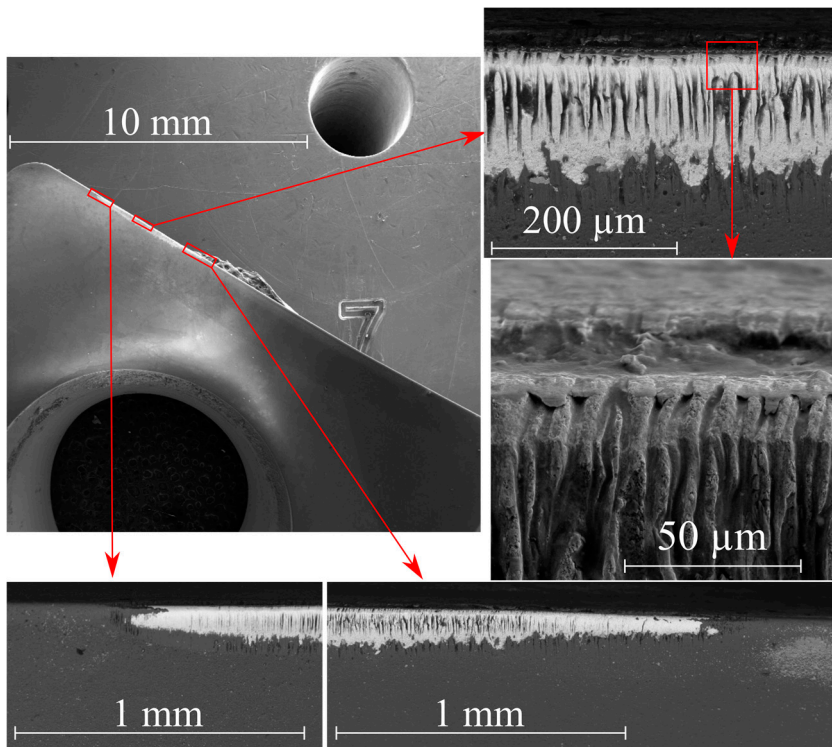
Figure 3.11. SEM image of the edge line of a used insert. In sections of the edge line, the coating is worn off and the cemented carbide is showing.

3.2 Results of laboratory machining tests

High uncertainty of the machining conditions and the end results when using industrial tests, as shown in previous section, calls for more controlled environment if only the influence of material is to be evaluated. Hence, this section presents results of laboratory testing. Several aspects of machining are investigated to

highlight the difference between the used alloys. Results from the different investigations will be presented in separate sub-headings.

3.2.1 Cutting resistance

All cutting processes give rise to cutting forces that act on the tool. These forces can to some extent be controlled by tool selection, and cutting data used in the process. If the forces are too high, it can lead to discarded components due to tool failure or dimensional deviations outside the tolerance range.

In some cases, it is not possible to avoid high cutting forces, and then it is important to ensure that the workpiece is sufficiently clamped and that the machine has sufficient rigidity and is able to perform the operation. The cutting speed v_c is much larger in the main cutting direction than the tool's speed in the feed direction, and consequently the power needed to perform a certain cutting operation can be approximated based on the main cutting force and v_c.

There are two commonly used models to describe how the main cutting force varies depending on the chip area. Both the Woxén-Johansson [90; 91] equation (5) and the Kienzle [92] equation (6) are named after their inventors. Although both models describe the same phenomenon, different terminology is used. Woxén-Johansson's model describes 'cutting resistance', whereas Kienzle's model describes a 'specific cutting force'. Irrespective of which terminology is used, cutting resistance and specific cutting force are not material properties; they are highly dependent on the conditions that exist in the cutting process, that is, tool geometry and the tribological aspects of the tool and the process. The difference between specific cutting force and cutting resistance is purely semantic, and the term 'cutting resistance' will be used throughout the dissertation.

Some differences in the physical interpretation of the constants exist. The constants in (5) approximately describe the load distribution between the tool's rake and clearance side. Cr_1 is associated with the load on the rake side, and Cr_2 with the load on the clearance side. For large h_1, Cr asymptotically approaches towards Cr_1. For Kienzle's model, (6), the physical interpretation of the constants is more difficult, especially for small values of h_1.

$$Cr = \frac{F_c}{h_1 \cdot b_1} = \frac{C_1}{b} + \frac{C_2}{h_1 \cdot b} = Cr_1 + \frac{Cr_2}{h_1} \tag{5}$$

$$k_s = \frac{F_c}{h_1 \cdot b_1} = k_{c1.1} \cdot h_1^{-m_c} \tag{6}$$

The constants for both models need to be determined through measurements of cutting force at varying h_1. Measurements of cutting forces were made using a force dynamometer, Kistler 9129 AA, in a lathe, SMT 500.

The cutting resistance is measured using two different tools, a flat tool that was plane ground into neutral geometry and a sharper tool with a positive rake angle, see Figure 3.12 and Figure 3.13. For tests done with a tool with neutral geometry, Figure 3.12, the highest cutting resistance is seen for CuZn38As, which is a purely α-brass with high ductility and impact toughness. High ductility, combined with high impact toughness, means that much energy is required to separate the chips from the workpiece. It also means that the material can withstand much deformation without fracturing. The two alloys with high Pb content (CuZn38Pb3 and CuZn35Pb1.5AlAs) have approximately half the cutting resistance of CuZn38As. Interestingly, the material's hardness does not correlate with the measured cutting resistance. The largest correlation between cutting resistance and material properties is found for impact toughness. The cutting resistance would be ranked in the same order as impact toughness when sorting from highest to lowest, except that CuZn21Si3P and CuZn35Pb1.5AlAs would be ranked in reverse order.

Using a positive rake angle decreased the cutting resistance for all tested materials. This is not surprising, as similar conclusions were drawn in the classic work on metal cutting, *On the Art of Cutting Metals* [93]. The biggest effect of the positive rake angle is seen for CuZn38As, where the cutting resistance was halved in the tested range of h_1. For the other tested alloys, the cutting resistance was also reduced, but not to the same extent as for CuZn38As.

Both models for cutting resistance work reasonably well for all tested materials. Kienzle's model slightly underestimates the cutting resistance for small chip thicknesses when using a neutral tool geometry but shows a good fit for the tool with positive geometry.
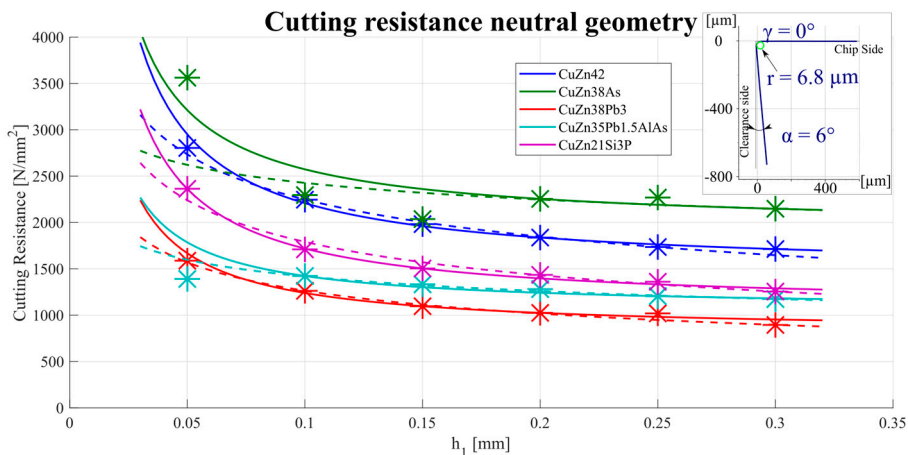
Figure 3.12. Cutting resistance for different brass alloys using an insert with neutral geometry. The solid line shows cutting resistance according to Woxén-Johansson, the dashed line cutting resistance according to Kienzle. Stars show the measured values used for determining the model constants.
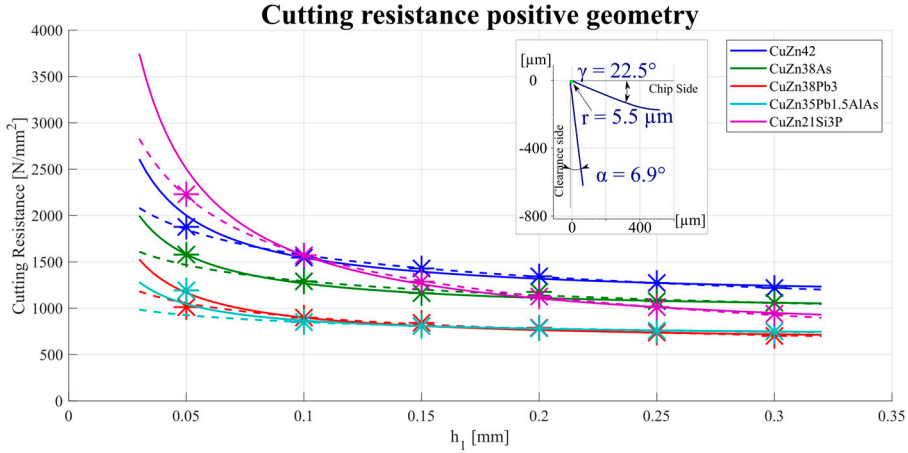
Figure 3.13. Cutting resistance for different brass alloys using an insert with positive rake angle. The solid line shows cutting resistance according to Woxén-Johansson, the dashed line cutting resistance according to Kienzle. Stars show the measured values used for determining the model constants.

For machining of steels, hardness is a good predictor of cutting resistance [62]. In the case of machining of brass, hardness is shown to have very limited ability to predict cutting resistance. CuZn21Si3P is significantly harder than the other alloys but has lower cutting resistance than the other Pb-free alloys when using neutral tool geometry. The alloy with the lowest hardness, CuZn38As, has the largest *Cr* for neutral tool geometry. Instead, cutting resistance for brass alloys appears to be more linked to material properties that affect the contact length between tool and chip and adhesion, such as ductility and impact toughness, and chip formation. The chip form is largely dependent on inhomogeneity of microstructure, such as presence of phases with different mechanical properties. Extreme example of inhomogeneous microstructure are brass alloys with high Pb-content since the segregated Pb-globules are much weaker than the surrounding brass. Low cutting resistance is seen for both alloys with high Pb-content, which calls for further investigation on the function of Pb in metal cutting, see section 3.3.

3.2.2 Tool temperature

Since cemented carbide tools are much harder than brass and there are no phases or particles with comparable hardness to the tool material as measured by microhardness measurements, abrasion is a highly unlikely wear mechanism when machining brass with cemented carbide tools. More likely wear mechanisms are chemical or diffusion-related wear processes. Both of these wear mechanisms are highly dependent on, and accelerated by, temperature. When machining Pb-free brass, tool life is reported to be much shorter than when machining brass with high

Pb content [94]. To compare the temperature in the cutting zone, thermal imaging was used [95; 96]. As seen in section 3.2.1, the cutting resistance is reduced when using tools with positive rake angle, making it of interest to measure whether the rake angle has a large influence on tool temperature.

In the below reported tests, temperature is measured using infrared thermal camera and only the tool temperature is measured since it is difficult to reliably measure the chip temperature because it is affected by the emissivity of the material being machined. For brass alloys, emissivity ranges between 0.03–0.5 [97]. The lowest values occur for polished surfaces, and the emissivity strongly increases with increasing surface roughness, degree of oxidation, and the temperature itself [98]. During machining, the side of the chip simultaneously experiences a varying degree of change in roughness and oxidation, thus making the thermal data from chips very unreliable. Cutting tool, on the contrary, remains stationary and unaffected, thus investigation of tool temperature is more reliable.

The tool temperature measurements were performed during orthogonal turning of disk-shaped workpieces, as shown in Figure 3.14. The depth of cut (disk thickness) $a_p = 2$ mm and the cutting speed $v_c = 200$ m/min were kept constant, but the feed varied from $f = 0.05$ mm/rev to 0.2 mm/rev for three tools with different rake angles ($\gamma = \pm 10°$ and $0°$). An infrared thermal camera (FLIR X6580sc with a T198970 lens) was set up to capture the side of the cemented carbide tool at 200 frames per second. The tool was positioned 0.15 mm outside the disk on the camera side to avoid uncut material and burrs covering the camera's view. The emissivity of the cemented carbide tool was set to 0.3 as determined by separate two-colour pyrometer and thermocouple tests.
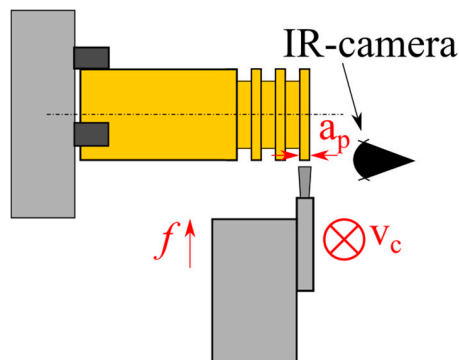
Figure 3.14. Setup for thermal imaging using othogonal turning.

In general, the tool temperature when machining brass is very low compared to that when machining other materials, as seen in. The highest measured tool temperature of 360 °C is seen when machining CuZn38As with $f = 0.2$ mm/rev. Similar temperatures are seen when machining the other Pb-free alloys, CuZn42 and

CuZn21Si3P, . In machining materials other than brass, tool temperatures are reported to be above 900 °C for Ca-treated steel [99] and just below 1100 °C for Ti6Al4V [100], both measured at v_c = 300 m/min. For brass with high Pb content, very low tool temperatures (below 200 °C) were measured for all tested cutting conditions. The low tool temperature, in combination with low mechanical load, may explain the extremely long tool life when machining brass with high Pb content.
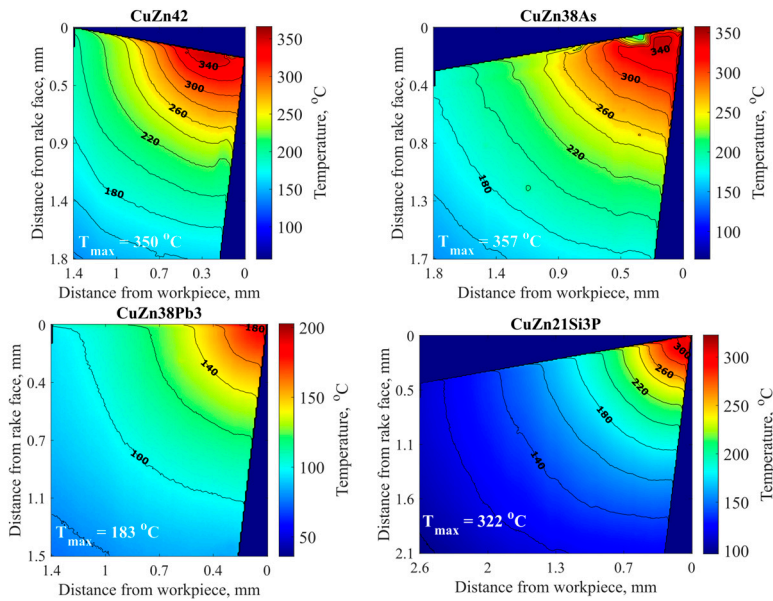
Figure 3.15. Examples of tool temperatures when machining different brass alloys using a_p = 2 mm, v_c = 200 m/min and f = 0.2 mm/rev.
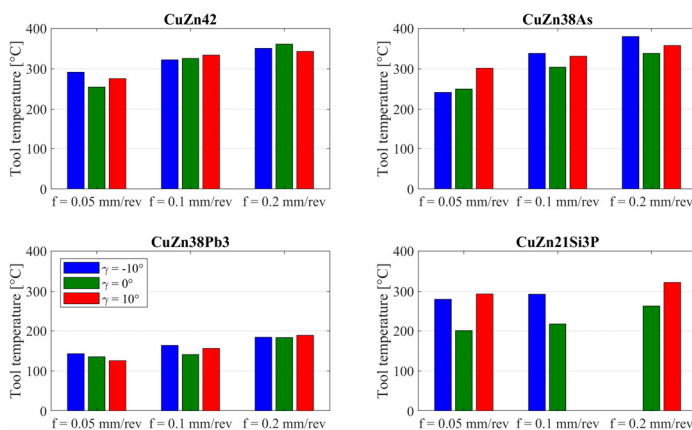
Figure 3.16. Summary of measured tool temperatures for different brass alloys, cutting conditions and tool geometries.

The measurement of tool temperature also involved varying rake angle γ in three steps between -10 ° and 10 ° since a large influence of rake angle was seen for the cutting resistance described in section 3.2.1. When using a positive rake angle, the heat generated in the cutting zone is concentrated closer to the cutting edge as less tool material is available for an efficient heat dissipation, see Figure 3.17. Although heat transfer in not favourable, the maximum tool temperature is not significantly higher when using a negative angle γ since the cutting forces are simultaneously reduced, as previously described.
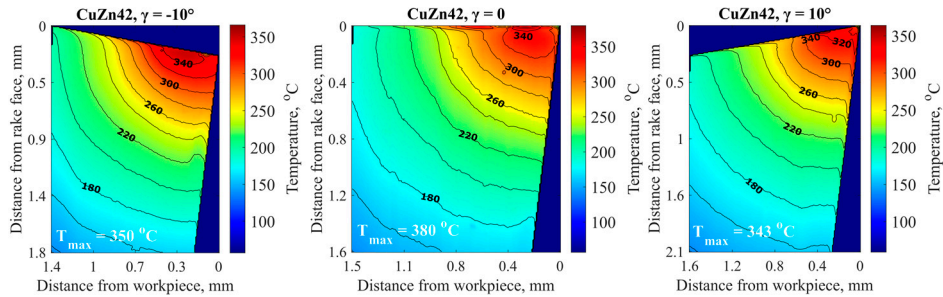
Figure 3.17. Influence of varying rake angle γ in the range ± 10 ° using a_p = 2 mm, v_c = 200 m/min and f = 0.2 mm/rev.

3.2.3 Chip formation

The formation of long chips is one of the largest issues when implementing production in Pb-free brass. In machining, brass with high Pb content is known for producing short, discontinuous chips that are easily evacuated from the cutting zone and machine. Chip formation in metal cutting also affects the process behaviour as regards cutting forces and heat generation.

High-speed filming of the chip formation process involved an orthogonal cutting setup. A camera was installed in a planing machine to film the stationary tool and moving workpiece, see Figure 3.18, and set up to capture images at 30,000 frames per second. The experimental conditions used a constant cutting speed and various theoretical chip thicknesses h_1 between 0.05 and 0.4 mm and rake angles, γ, between 10° and -10°.
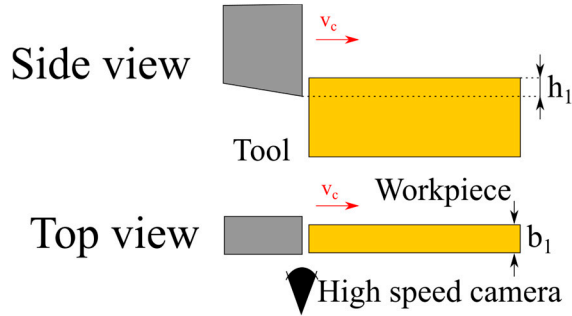
Figure 3.18. Setup for high-speed filming in orthogonal planing machining setup.

It is difficult to obtain continuous chips in brass with high Pb content. Throughout the test set with high-speed filming, semi-continuous chips were only seen for smallest values of h_1 and positive γ, as shown in the top part of Figure 3.19. For all other tested conditions, the chip formation follows the typical segmentation sequence of compression by the tool followed by deformation along the shear plane and separation from the workpiece [101], as in the lower part of Figure 3.19.
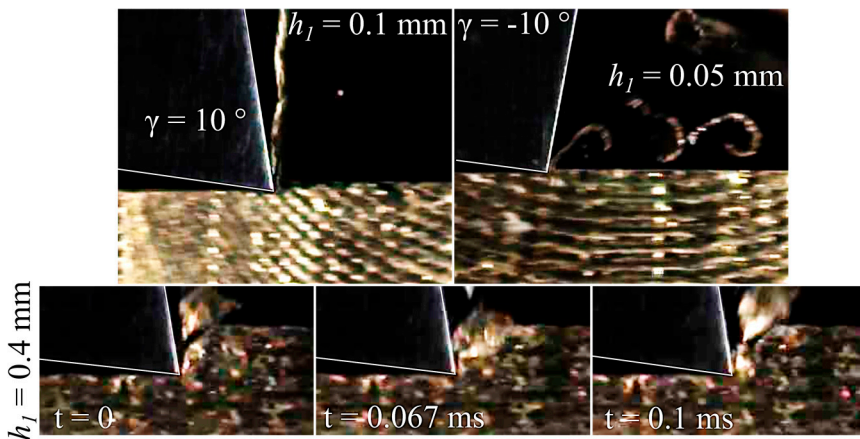
Figure 3.19. Chip formation in CuZn38Pb3 with timestamps for the chip separation process.

The chip formation process in the single phased α-alloy, CuZn38As, is entirely different from the discrete chip segments seen for CuZn38Pb. Continuous chips are formed, and no chip breakage occurred over the machined length (40 mm). Figure 3.20 shows that the chip formation is homogenous with only traces of segmentation. Machining of α-brass is, in this respect, very similar to machining pure copper [102]. Some side-flow and bi-chip formation is seen for all tool geometries at $h_1 > 0.1$ mm. CuZn38As has the highest impact toughness of all the tested alloys, which indicates that the material keeps its high ductility in rapid deformation, resulting in poor chip breaking and side flow. A small chip curling

radius promotes chip breaking and, as seen in Figure 3.20, a negative rake angle produces a more tightly curled chip, although not enough to break the chips in the tested conditions. The curling radius increases with increasing γ.
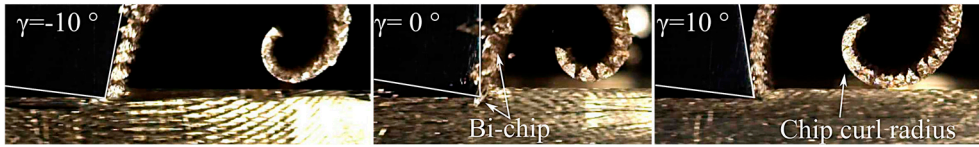
Figure 3.20. Chip formation in CuZn38As for various rake angles γ at $h_1 = 0.2$ mm.

When machining an alloy with a secondary phase, the chip segmentation is more pronounced, as is seen when machining CuZn42 and CuZn21Si3P, Figure 3.21 and Figure 3.22. The difference in mechanical properties between the phases makes the deformation non-uniform when the material is exposed to uniform stress, which promotes chip breaking. Chip segmentation is also seen for both duplex alloys, but is more pronounced in CuZn21Si3P compared to CuZn42. The difference in mechanical properties between the phases is greater in CuZn21Si3P than for CuZn42 due to the addition of Si in the material and the formation of the relatively hard and brittle κ′ phase. For CuZn42, a longer contact length, l_c, between tool and chip is seen for negative γ compared to positive γ. However, Figure 3.17 shows there are only slight differences in tool temperature for these different cutting conditions.
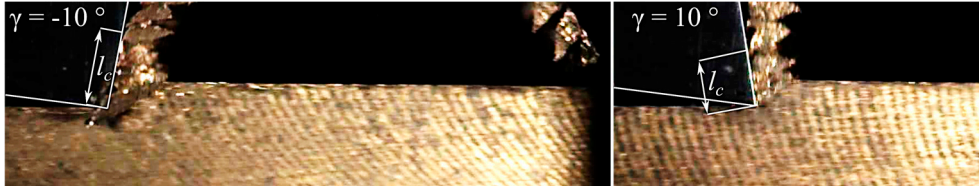
Figure 3.21. Chip formation in CuZn42 using γ = ±10° at $h_1 = 0.4$ mm with the contact length, l_c, between tool and chip marked.
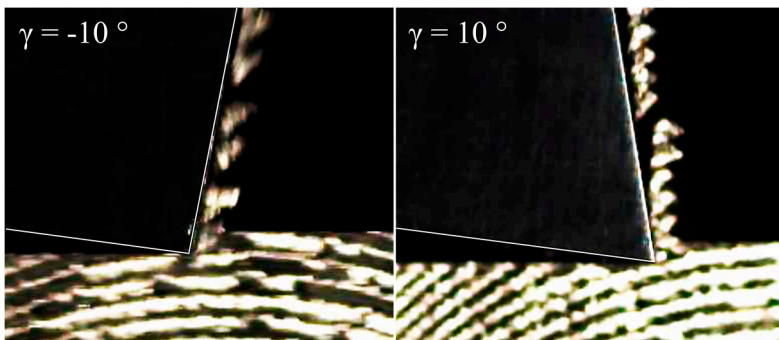
Figure 3.22. Chip formation in CuZn21Si3P using γ = ±10° at $h_1 = 0.2$ mm.

47

To be able to further examine the chip formation process, the instantaneous cutting zone and chip root during machining must be made visible. This was done using a quick-stop method. The setup is schematically shown in Figure 3.23. During machining, a striker M is accelerated towards the tool by a gunpowder charge. Upon impact, the tool will pivot and break the shear pin, thereby disengaging from the workpiece. The chip root obtained, see Figure 3.24, is subsequently cross-sectioned and polished to reveal chip formation, microstructural changes, and the deformation zones within the chip ε_I, at the tool–chip interface ε_{II}, and at the tool–workpiece interface ε_{III}. All chip roots are prepared using the same cutting data: $a_p = 2$ mm, $v_c = 70$ m/min and $f = 0.4$ mm/rev.

For visualization of the chip roots, ion beam polishing of the samples, followed by Ion Channelling Contrast Imaging (ICCI) [103] was performed on a FEI Nova 600 Focused Ion Beam/Scanning Electron Microscope (FIB/SEM). ICCI is an imaging technique that provides excellent grain contrast in brass.
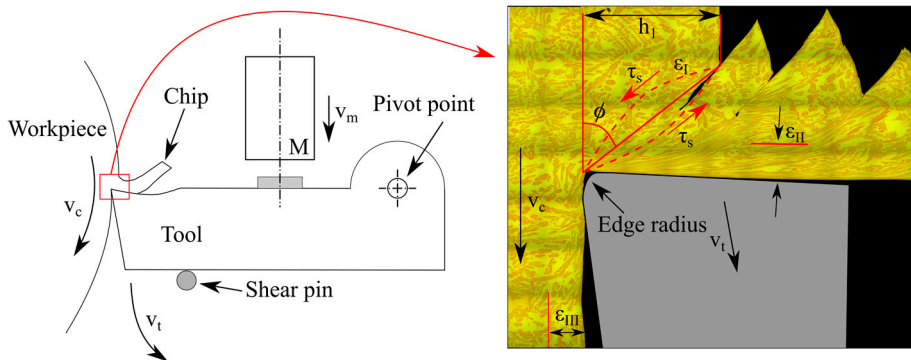
Figure 3.23. Test setup for acquisition of quick-stop samples. The image is inspried by Childs [104].
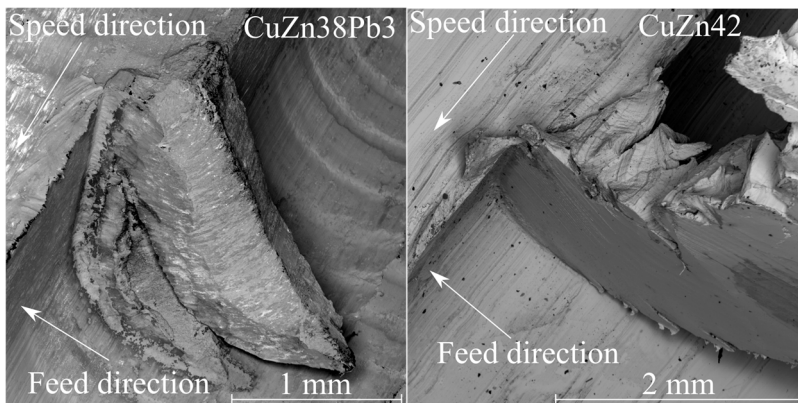
Figure 3.24. Chip roots from quick-stop machining before extraction from the workpiece.

The chip root of CuZn42 (Figure 3.25, right) is characterized by segmentation, with larger segments separated by shear bands, shown in Figure 3.25. The shear bands seen in the image are very thin and material with less deformation can be seen between the shear bands. Shear bands are formed in metals under adiabatic shear deformation. The formation of shear bands is highly dependent on the material's thermal conductivity; low thermal conductivity promotes formation of shear bands [105]. The secondary ε_{II} and tertiary ε_{III} deformation zones, on the other hand, are substantial: both around 100 μm.
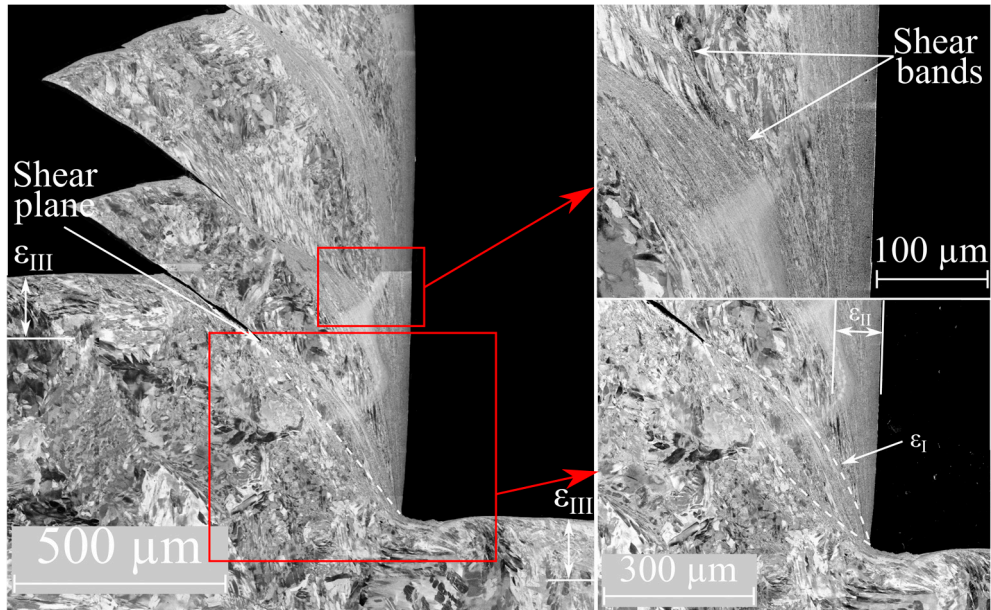
Figure 3.25. ICCI of chip root from machining of CuZn42.

A degree of chance is involved in quick-stop testing, especially for materials with discontinuous chip formation. When preparing the chip root for CuZn21Si3P, the cutting process was stopped when the tool had moved approximately 200 μm after chip separation, Figure 3.26. The fracture surface after the chip separated is visible and a small chip is starting to form. Even at the beginning of cutting the wedge remaining after chip separation, serrations in the chip are formed.
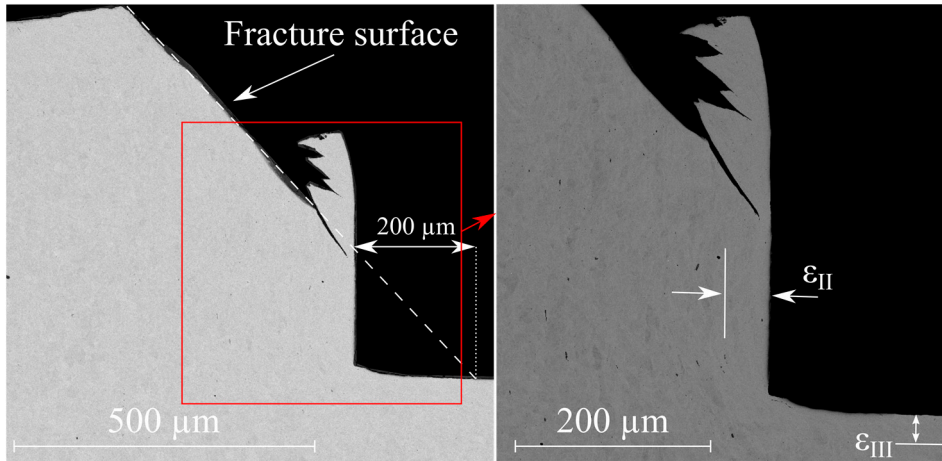
Figure 3.26. Chip root from CuZn21Si3P shortly after chip separation.

A well-defined primary deformation zone, ε_I, between the undeformed workpiece material and the deformed chip can be seen in the chip root, extracted after quick-stop from machining of CuZn38As shown in Figure 3.27. In ε_I, a relatively sharp line between material with a grain structure and heavily, uniformly, deformed material indicating increasing shear stress closer to the shear plane where the maximum stress level is found. Signs of increasing stress close to the shear plane is shown by the unidirectional slip lines and shear bands inside individual grains. Contrary to the chip root of CuZn42, no shear bands originate from ε_I, which may be related to the homogeneous microstructure of CuZn38As resulting in even deformation. For all metal cutting operations, the workpiece material flowing against the tool is separated into two separate flows by the cutting edge. The point where the material flow is separated, in the vicinity of the edge radius is called the stagnation point. In practice, the stagnation point is dynamic and will move slightly during the machining process. Therefore, the stagnation zone, where the material flow is separated between chip and workpiece is labelled in Figure 3.27. The secondary shear zone, caused by the normal and tangential stresses at the tool and chip interface, is ~150 µm wide with several layers of shear bands. ε_{III} can be seen at several locations in the chip root, to the left of the chip from the previous cut and to the right from the interrupted cut. Since the deformation in the chip is relatively even, traces of the severely deformed part of ε_{III} can be seen on the backside of the chip.
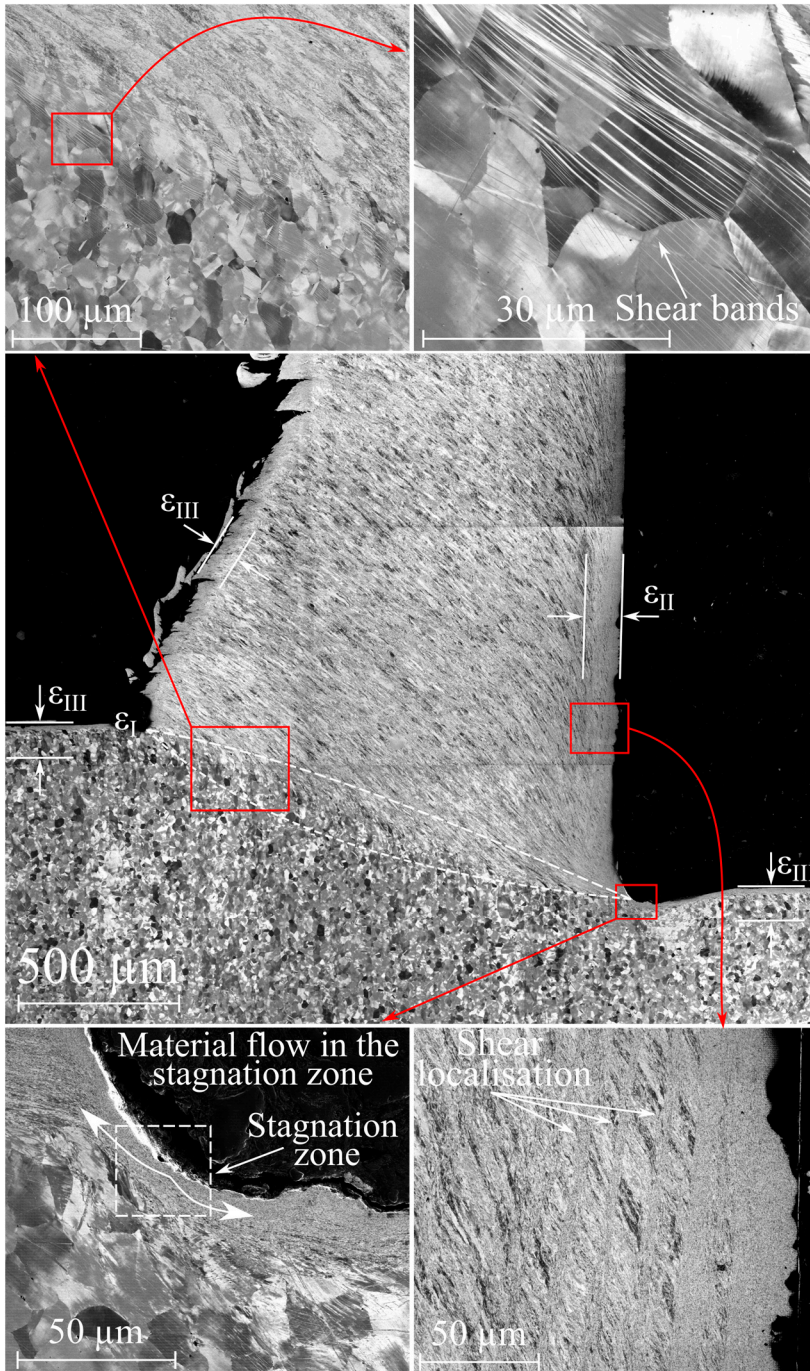
Figure 3.27. ICCI of a chip root from machining of CuZn38As with important features marked.

Two different tool geometries were used in preparation of chip roots of CuZn38As, one with neutral γ and one with the geometry seen in Figure 3.13 ($\gamma = 23$ °), since there is a large difference in cutting resistance when using the tools. The chip formation is continuous without signs of segmentation, and the shear angle ϕ is similar for both geometries used. It can be noted that the chip is tapered in the neutral geometry case, indicating the same type of uneven chip formation reported by Childs et al. [106] in machining pure Cu. From the chip roots, it is not clear why the cutting resistance is much lower for the tool with $\gamma = 23$ °.
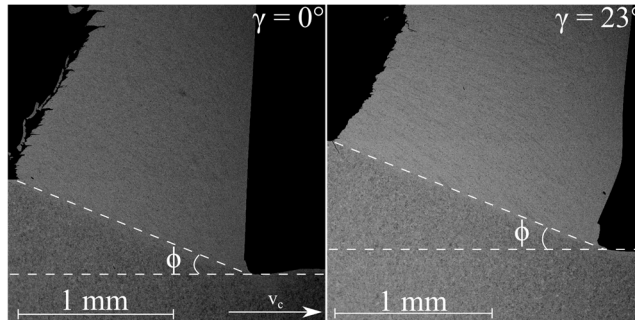
Figure 3.28. Chip roots from machining of CuZn38As with different tool geometries.

Even though the measured Pb content of CuZn38As is low (0.12 wt.%), small Pb globules are found in the material. When these globules pass through the primary shear zone, they become deformed and elongated, see Figure 3.29. This is similar to what is seen in free-machining steels with added manganese sulphide (MnS) to improve machinability [107]. A Pb content of 0.12 wt.% appears to be too low to provide any machinability enhancing effects.
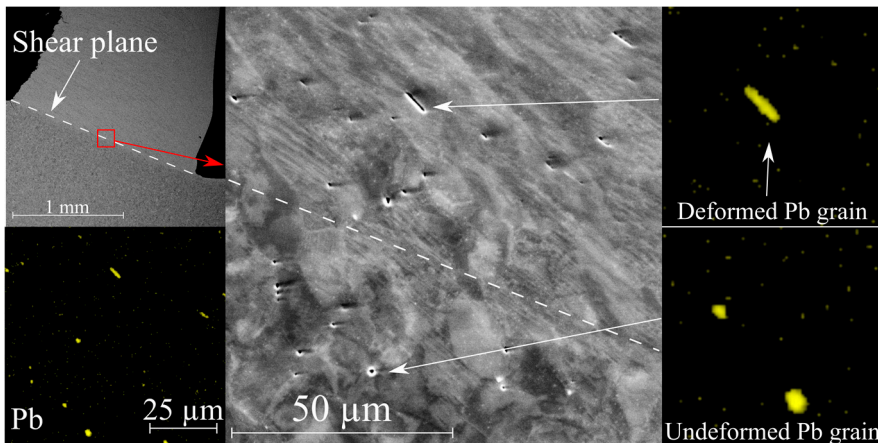
Figure 3.29. Detailed study of the shear plane of a quick-stop sample obtained from machining CuZn38As.

Large differences in the chip formation process are seen for the materials. The local and time-resolved differences in chip formation process itself cause differences in cutting forces that can only be measured with a high sampling rate. The dynamic cutting forces were measured by a centre-in-line force sensor designed and built at the Department of Mechanical Engineering Sciences at Lund University [108; 109]. The force sensor has a high eigenfrequency and thus allows high sampling rates during the measurement. In this study the sampling rate was 200 kHz. All measurements of dynamic cutting forces were done using a flat ground cemented carbide tool with neutral geometry at $v_c = 150$ m/min, $a_p = 2$ mm and $f = 0.4$ mm/rev.

A clear correlation between the dynamic cutting forces and chip form can be seen in Figure 3.30. The higher the degree of segmentation seen in the chip, the higher the amplitude. For the alloys with high Pb content, CuZn38Pb3 and CuZn35Pb1.5AlAs, discrete chip segments are formed and the cutting force is almost sinusoidal. The separation frequency and the size of the separated segments are different for the two alloys, which may be linked to the amount of Pb globules found in the materials. For the pure α-alloy, CuZn38As, very little variation in cutting force is seen and the deformation in the chip is even. Some variation in chip thickness is also seen, as previously mentioned for the quick-stop sample. The alloys that have a segmented chip formation, CuZn42 and CuZn21Si3P, show similar variation in cutting force over the measured length. The average cutting force is higher for CuZn42 compared to CuZn21Si3P, as is expected from the measurements of cutting resistance shown in Figure 3.12. The segmentation is more pronounced for CuZn21Si3P than for CuZn42, but both chips came out as continuous.
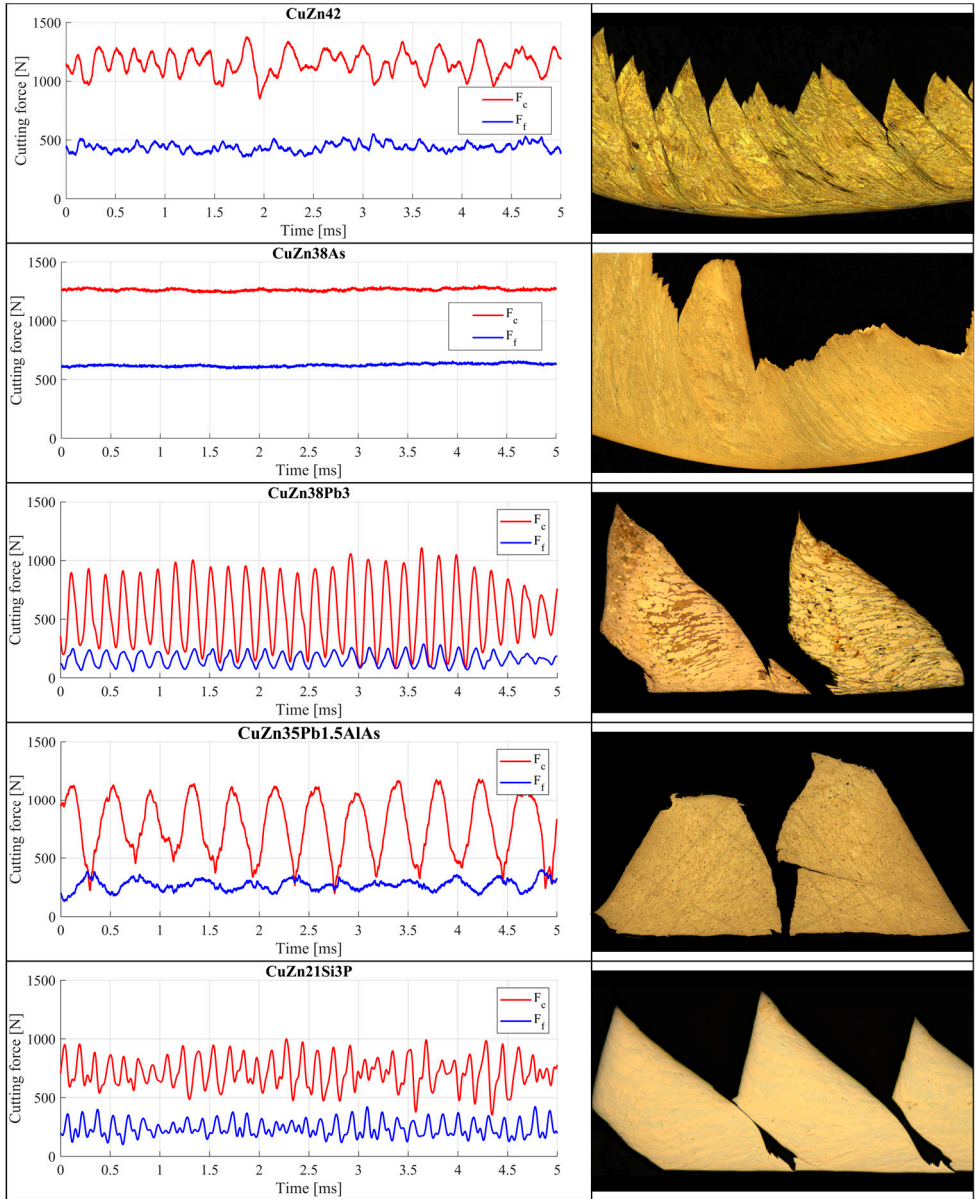
Figure 3.30. Dynamic forces and chip form for the alloys used with the cutting data $v_c = 150$ m/min, $a_p = 2$ mm and $f = 0.4$ mm/rev.

3.3 Function of lead in machining of brass

As shown in section 3.2, as well as by other authors [33; 34; 110], the machinability of brass alloys that contains more than 3 wt.% Pb is very high. While several contradictory opinions on the function of Pb in the machining of brass alloys have been formulated, consensus exists on the benefits Pb brings to the outcome of machining operations [32; 36; 37; 94; 111].

(i)   Excellent chip control and chip breaking

A characteristic feature of machining leaded brass is the extremely favourable chip form with small, discontinuous chip segments. Under common production conditions, no continuous chips will be formed irrespective of depth of cut and feed [28]. The type of chips formed (continuous, segmented, discontinuous) is linked to the mechanical and thermal properties of the workpiece material [112]. When using standard tensile testing protocols, similar mechanical properties are found for brasses with similar phase compositions but different lead content, as shown by Figure 2.7. However, the behaviour of these alloys during machining is quite different. Doyle [25] attributed the discontinuous chip formation in leaded brass to a ductile rupture process instigated by segregated Pb globules in the alloy.

(ii)   Low cutting forces

Measurements of cutting forces for different brass alloys clearly show that brass alloyed with Pb results in lower cutting forces than those generated for lead-free variants (Figure 3.12 and Figure 3.13).

A possible explanation for the lower cutting forces in machining of brass alloyed with Pb was presented by Stoddart et al. [27] in 1979. Using Auger electron spectroscopy, they demonstrated that lead forms a thin film on the side of the chip that slides against the cutting tool. They suggested that the lead layer forms and replenishes on the tool–chip interface, so contributing to lubrication, cooling of the cutting edge, and reduction of forces. Gane [24] further investigated friction in the machining of leaded and lead-free brass, using both cutting and sliding experiments. His experiments showed that the friction stress for leaded brass was about half that measured for brass without lead. He proposed that the reduced cutting forces when cutting leaded brass could partly be attributed to the weak interfacial bond between the brass matrix and Pb globules. The weak interface might allow separation and void formation under plastic deformation. Wolfenden and Wright [23] investigated the temperature in the secondary shear zone and whether Pb appeared in solid state or as a liquid in the cutting zone. They concluded that although the heating time of a chip in a metal cutting operation is extremely short, at cutting speeds above $v_c =$ 125 m/min the dispersed Pb globules in the material will melt at the end of the secondary shear zone. Such melting is expected to facilitate lubrication of tool-chip interface and result in lower cutting forces. However, these tool temperatures were

not explicitly measured but were based on calculations using shear plane angle theory.

(iii)   Long tool life

In machining brass using cemented carbide tools, there is a large difference in hardness between the tool and the workpiece material. A low level of abrasive tool wear is expected, suggesting that diffusional wear or chemical wear controls tool life. Both of these degradation processes are highly dependent on cutting temperature and can be slowed by using protective coatings. The tool temperatures reported in the literature [13; 23; 113] indicate the possibility that Pb may melt in the secondary shear zone. If melting of the metal occurs in the cutting zone, it can form a protective film between tool and chip, thus retarding diffusional or chemical wear processes. Samandi and Wise [13] measured tool temperatures based on microhardness measurements and microstructural changes in a cutting tool made of a tool steel (1 % C; 1.5 % Cr). Based on these measurements, the tool temperature at the end of the contact zone was found to be around 350 °C at a cutting speed of 120 m/min for leaded brass. However, these results for tool steel may not be transferable to today's industrially used cemented carbide tools, which have different properties and tribological performance.

The literature thus agrees that Pb benefits the machining process, yet the exact mechanisms associated with these benefits are open for discussion.

- It is not clear whether Pb melts during the machining process. If so, does it melt in the primary or secondary shear zone?
- Is the difference in cutting force due to tribological or mechanical properties, and does the effect originate in the primary or secondary shear zone?
- Is the long tool life for leaded brass related to the formation of a diffusion barrier from the Pb film on the cutting tool, or to the low temperatures caused by low force and short contact length?

Answering the above questions will throw more light on the machinability enhancing effect of adding Pb to brass alloys. When the mechanism that provides the machinability enhancement is more clearly understood, the knowledge may be used to provide the same effect using other means, so contributing to the development of more machinable lead-free brass alloys.

To address these questions, CuZn38Pb3 and CuZn42 were compared. These materials have similar chemical content, with the exception of Pb, and similar mechanical properties in tensile testing. However, the cutting resistance when machining CuZn42 is about 50 % higher compared to machining CuZn38Pb3.

Revisiting section 3.2.2 where results from thermal imaging are shown, allows the first question to be answered. The highest measured tool temperature for

CuZn38Pb3 is around 180 °C for $f = 0.2$ mm/rev (Figure 3.16) which is significantly lower than the melting temperature of Pb ($T_{melt, Pb} = 328$ °C). CuZn42 gives nearly double the tool temperature, 368 °C, under identical cutting conditions. It can also be noted that the hottest zone on the tool is located some distance from the cutting edge when machining CuZn42, indicating the presence of sticking and sliding regions on the rake face associated with continuous chip formation [107]. The low measured tool temperature for CuZn38Pb3 may in part also explain the long tool life reported for leaded brass.

As already indicated by the thermal imaging, the tool–chip contact length appears to be different for the two materials. High-speed filming shows the same trend as thermal imaging, but with better temporal and spatial resolution. Figure 3.31 shows that for CuZn38Pb3, the chip is separated from the workpiece as discrete segments, unlike the chips produced from CuZn42 where the chip is segmented but continuous. The contact length, l_c, for CuZn38Pb3, is comparable with the theoretical chip thickness and ranges $l_c = (0.6–1.0) \cdot h_1$. For CuZn42, the contact length is much larger, namely $l_c = (1.7–2.2) \cdot h_1$.
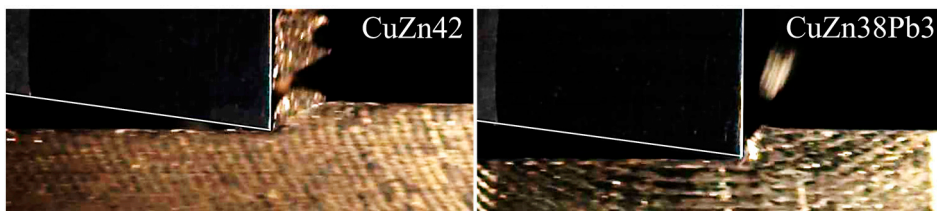
Figure 3.31 Images showing the chip formation and tool-chip contact length, l_c, for CuZn38Pb3 and CuZn42 at $h_1 = 0.2$ mm [114].

More remarkable is that the chip formation for CuZn38Pb3 is independent of cutting speed, as seen in Figure 3.32. Even at cutting speeds as low as 12 m/min, the chip formation follows the typical segmentation sequence of compression by the tool followed by deformation along the shear plane and separation as is shown in Figure 3.19. Such chip segmentation at low speed indicates that the short chipping of leaded brass is not controlled by temperature in the primary deformation zone and precludes the melting of Pb on the interface between the chip segments. A more likely explanation for the chip formation is presented by Doyle [25], who investigated the plastic instabilities that can arise in heterogeneous materials. Pb has nearly a 10 times lower Young's modulus and 20 times lower strength than the matrix brass alloy [8], making brass with high Pb content highly inhomogeneous on the micrometre scale.
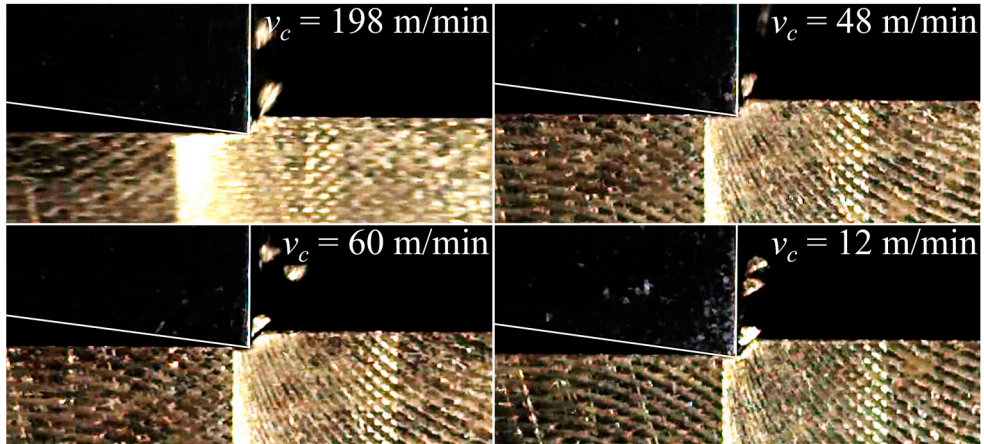
Figure 3.32. Chip formation during machining of CuZn38Pb3 alloys at various cutting speeds ($h_1 = 0.2$ mm, $b_1 = 3.5$ mm) [114].

Even though melting of Pb does not take place in common machining operations, this does not mean that Pb has no influence on the cutting process. Some authors [23; 113] suggest that Pb has a significant lubricating effect that enhances machinability. Thermal softening, and thus its lubricating efficiency, is temperature dependent. This effect should be quantifiable by varying the cutting speed, a controllable process parameter that has a direct effect on the process temperature.

A series of machining experiments within the speed range of $v_c = 2$ m/min to 100 m/min were conducted to evaluate the effect of Pb on cutting forces and the friction coefficient. All tests were performed using a constant depth of cut, $a_p = 2$ mm. The results can be seen in Figure 3.33. Figure 3.33 b–d show that the cutting forces for both brass alloys are largely independent of the cutting speed. However, the force level is higher for CuZn42 than for CuZn38ZnPb3 under all conditions. It is worth noting that machining the CuZn38Pb3 alloy resulted in a consistent artifact in force behaviour. This artifact consists of a strong variation in forces at particular speed ranges, which depended on the feed used. For feed $f = 0.1$ mm/rev, this variation was observed at $v_c = 30$ m/min. It increased to $v_c = 60$ m/min at $f = 0.2$ mm/rev, and further shifted to $v_c = 80$ m/min at $f = 0.3$ mm/rev. The most likely source of the variation is vibration or chatter. To eliminate this effect, the experiments were repeated with different setups, and even on another lathe with another force measurement system, yet all yielded similar results. An alternative explanation is that the formation of a built-up edge (BUE) might influence the forces. However, analysis of the machined surfaces and the cutting tools revealed no BUE. The consistency of the observed phenomenon calls for further investigation.
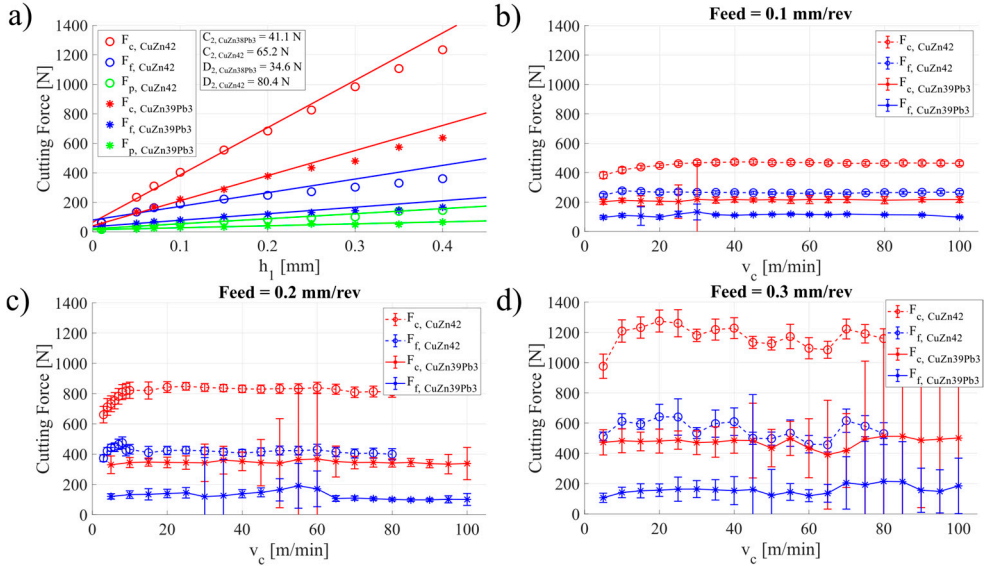
Figure 3.33. a) Measured cutting forces as a function of h_1 and their extrapolation to zero theoretical chip thickness ($v_c = 200$ m/min), **b–d)** Cutting forces as a function of cutting speed. Markers show the average values, and the error bars show one standard deviation [114].

Estimating the coefficient of friction on the tool-chip interface requires separating the force components acting on the rake and the clearance side of the tool. For rough machining applications, it is sometimes argued that forces on the flank can be neglected so that the coefficient of friction is simply a ratio of feed force to cutting force: $\mu = F_f/F_c$ [79].

The material below the stagnation point, whose slightly exaggerated position is denoted as y_s in Figure 3.34, moves towards the tool's clearance side, then is ploughed under the edge, and is thus not removed from the workpiece. Ploughing forces involved in this action do not contribute to the normal and frictional forces on the tool rake side. Similarly, the rubbing action of the tool clearance against the machined workpiece material adds to the clearance forces, see Figure 3.34. To be able to estimate the coefficient of friction on the rake face, it is necessary to subtract the forces on the tool's clearance side from the total measured cutting forces. Such separation can be easily done by extrapolating the feed or chip thickness values for $h_1 = 0$ [115]. Therefore, the total force can be described by (7), where C_2, D_2, and E_2 are the forces acting on the clearance side.
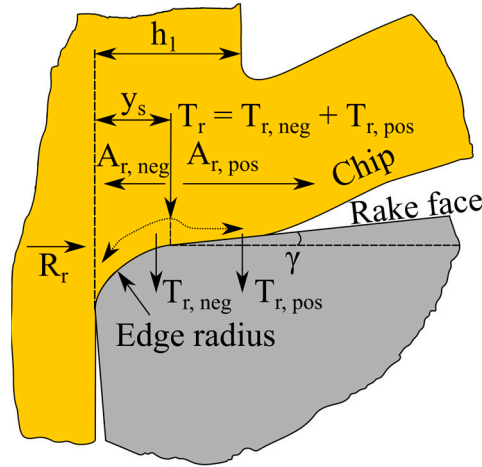
Figure 3.34. Section of an engaged tool with the forces that act on the rake face of a cutting tool. Modified after Ståhl [62] and Schultheiss [116]. [114]

$$F_c = C_2 + C_1 \cdot h_1 = T_r + T_{cl}$$
$$F_f = D_2 + D_1 \cdot h_1 = A_{cl} + A_r \qquad (7)$$
$$F_p = E_2 + E_1 \cdot h_1 = R_r + R_{cl}$$

Figure 3.33 a) shows the linearization of the cutting forces necessary to determine the values of C_2, D_2, E_2. From Figure 3.34 and equation (7) it is possible to derive and calculate the apparent coefficient of friction based on the measured cutting forces by slightly changing the model presented by Schultheiss et al. [116] to accommodate the contribution to friction from F_p, equation (8). The apparent coefficient of friction will be an indicator of how much Pb contributes to reducing friction and thereby the cutting forces.

$$\mu_r = \frac{\sqrt{A_r^2 + R_r^2}}{T_r} = \frac{\sqrt{\left(F_f - D_2\right)^2 + \left(F_p - E_2\right)^2}}{F_c - C_2} \qquad (8)$$

The calculated apparent coefficient of friction is shown in Figure 3.35. For CuZn42 (on the right), the apparent coefficient of friction μ_r is between 0.39 and 0.57 and is relatively constant over the considered range of cutting speed and the feed. The same cannot be said about machining CuZn38Pb3. While the change in μ_r over the speed range can be related to the force artifact mentioned above, there is also a strong dependence on the feed. At feed $f = 0.1$ mm/rev, the apparent coefficient of friction is $\mu_r = 0.45$, which reduces to $\mu_r = 0.24$ at feed $f = 0.3$ mm/rev. On the one hand, an expected increase in process temperature with an increased feed should facilitate softening of Pb, increasing lubrication efficiency, and thus result in a lower friction

coefficient. On the other hand, an increase in the cutting speed should also increase the process temperature and thus produce similar effects, yet the data shows that increasing speed does not reduce μ_r.
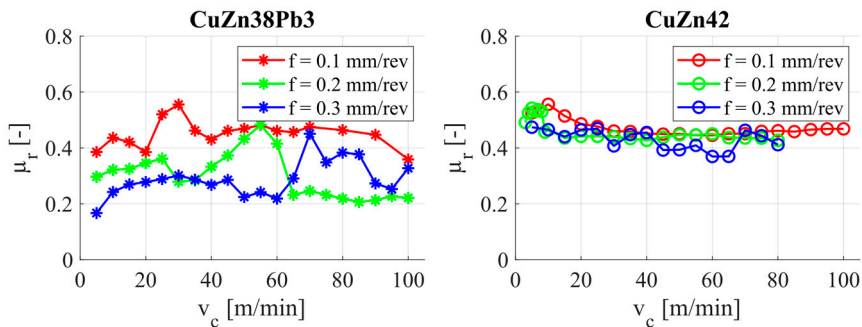
Figure 3.35. Apparent coeficient of friction for the two alloys based on values presented in Figure 3.33 [114].

The surface chemistry within the contact region was analysed in an attempt to detect the impact of Pb on the friction and tribology, because the mechanistic explanation appears to be contradictory. An uncoated cemented carbide tool was used to machine CuZn38Pb3 for three minutes at $v_c = 200$ m/min, $f = 0.2$ mm, and $a_p = 1.5$ mm. SEM and XEDS elemental maps, see Figure 3.36, do show the presence of lead on the rake face, but not in the contact zone between the tool and the chip. The Lα energy level for Pb is 10.55 keV, and thus XEDS maps were made using an acceleration voltage of 20 kV for accuracy of quantification. Using such high voltage for XEDS analysis means that the excitation volume also includes some bulk material and can probably not detect thin surface layers such as the Pb monolayer reported by Stoddart et al. [27].
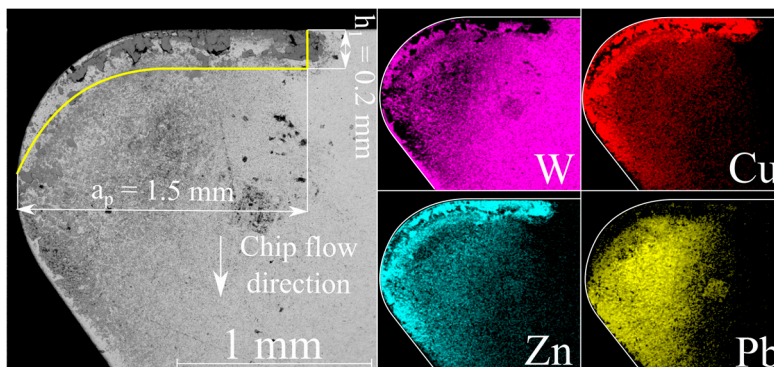
Figure 3.36. SEM image and XEDS maps of the rake face of a tool used to machine CuZn38Pb3 for three minutes. The theoretical chip contact area is marked by a yellow line. [114]

Time-of-flight secondary ion mass spectrometry (ToF-SIMS) was used to be able to detect even thin layers on the rake side of the tool, see Figure 3.37. The same tool was examined using both XEDS and ToF-SIMS. As with the XEDS, high levels of Pb were found outside the theoretical contact area, but ToF-SIMS reveals that the copper from the workpiece material covers nearly the entire contact zone. Pb is detectable in the part of the contact area furthest from the edge line. Using the analogy of the common sticking and sliding regions found on cutting tools [107; 117], lead is not present in the sticking region, but is slightly present in the sliding region. As shown in the high-speed footage, Figure 3.31 and Figure 3.32, the tool–chip contact length for CuZn38Pb3 is very short and approximately equal to the theoretical chip thickness. The footage also reveals that there is no sliding region in its conventional form. Therefore, it can be assumed that the Pb within the contact zone stems from rubbing of chips after separation from the workpiece, and the Pb outside the contact zone is from the particles ejected from the chips. Since the area where Pb is detected is small compared to the entire tool–chip contact zone, the effect of Pb on the frictional forces and its likely lubrication effect can be considered minor.
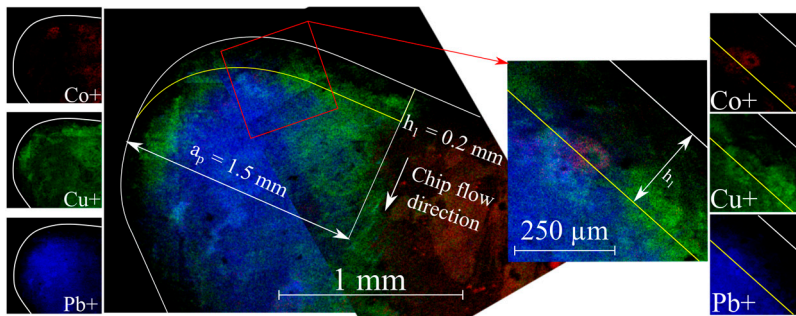
Figure 3.37. Chemical composition on the same tool as shown in Figure 3.36, captured by ToF-SIMS. [114]

The chip root of CuZn38Pb3 exhibits a morphology with a distinct and wide shear band and the expected segment separation, see Figure 3.38. The secondary and tertiary deformation zones are large: $\varepsilon_{II} \approx 100$ μm and $\varepsilon_{III} \approx 50$ μm as can be seen by elongation of the material structure and Pb globules. The primary deformation zone is also very wide ($\varepsilon_I \approx 100$–$150$ μm), where the Pb globules are strongly textured and parallel to the shear plane, as compared to the unaffected microstructure. A more detailed image of the primary shear zone can be seen in Figure 3.38, in combination with XEDS maps for relevant elements. The elongated and flake-like Pb globules are clearly visible as bright spots in the backscatter image. Additionally, in the XEDS map, high concentration of Pb on both sides of the shear plane is clearly distinguishable. High excitation voltage during XEDS analysis will read the signal from subsurface layers not visible in the backscatter mode. The agglomeration of Pb near the shear plane may stem from a high concentration of Pb on the shear plane itself.
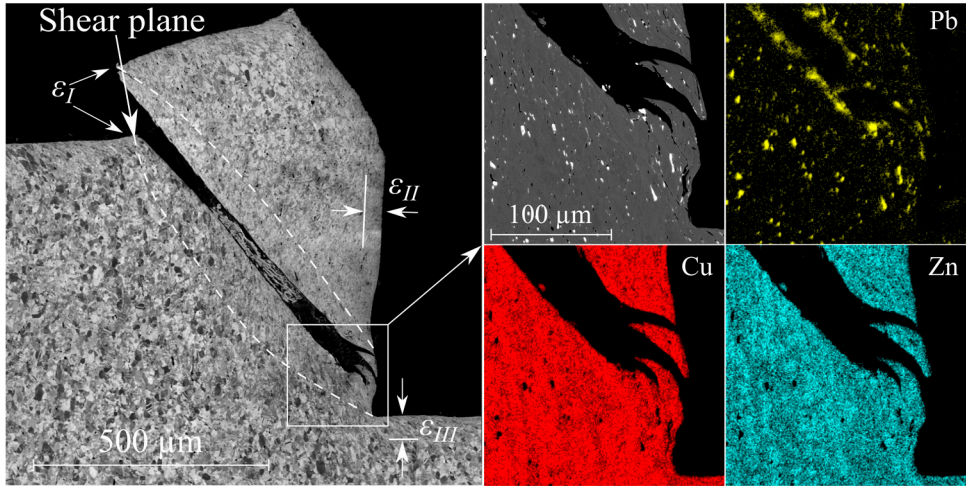
Figure 3.38. Chip root of CuZn38Pb3 (ICCI) and close up of the primary shear zone captured with backscatter SEM and XEDS elemental maps. Modified after Johansson et al. [114].

Not all sides of the shear plane are visible in the quick-stop sample; the plane itself is in the same direction as the viewing direction shown in Figure 3.38. Additional information about the shear plane can be found by inspecting the separated chip, see Figure 3.39. Investigations show that Pb is indeed elongated and smeared all over the chip side of the shear plane.
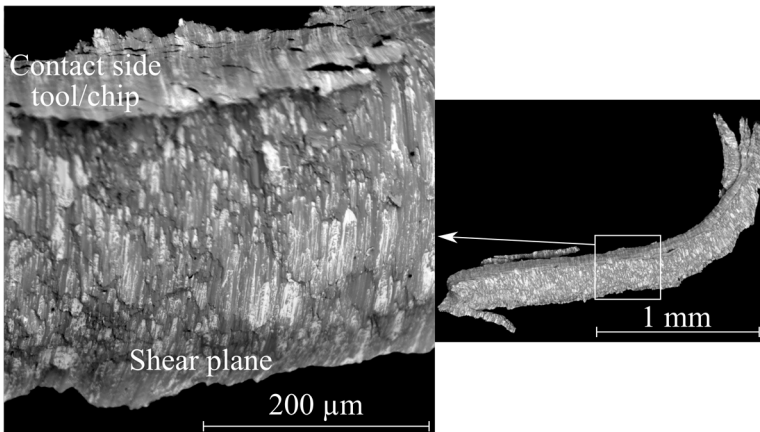
Figure 3.39. Backscatter SEM image of the shear plane on a CuZn38Pb3 chip. Bright areas show Pb. [114]

The same tendencies of smeared Pb found on the shear plane can also be found on the machined surface, see Figure 3.40. The layer of Pb found on the machined

surface is thin and is mostly visible when using a relatively low acceleration voltage in the SEM. At a high acceleration voltage of 20 kV, only traces of elongated Pb globules are distinguished. At a low voltage of 5 kV, Pb covers nearly the entire surface. Smearing of lead on machined surfaces is documented in the literature [13; 118]. From a product point of view, smearing and redistribution of lead across the machined surface is more problematic than the presence of Pb inclusions in the material. It is well known that the lead can leach into water and create adverse health and environmental effects (see section 1.3). The extensive surface coverage by Pb may create a spike in lead leaching and exposure during the initial stage of product use and cause more harm than estimated based on the Pb content of a material.
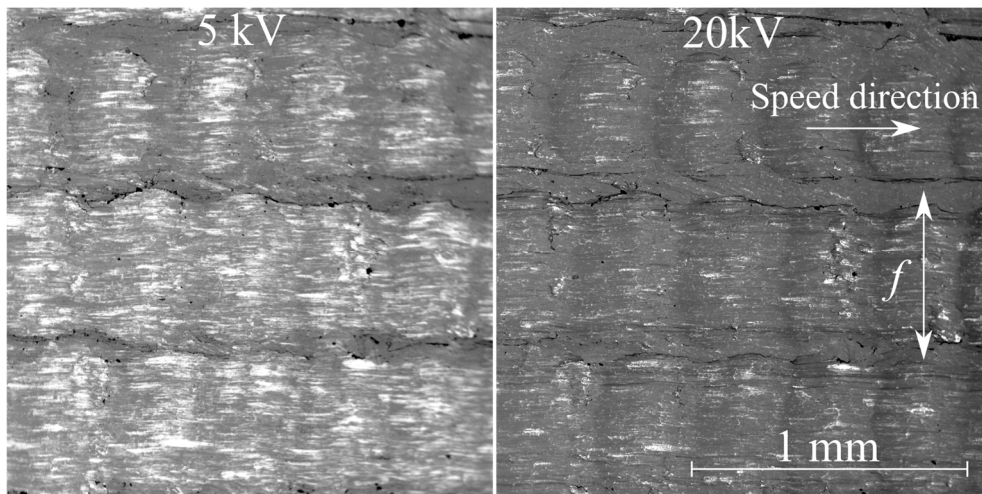
Figure 3.40. Surface of machined CuZn38Pb3 captured in backscatter mode at the same location with different acceleration voltages, 5 kV (left) and 20 kV (right). Bright areas show Pb. [114]

The findings presented here and in paper II suggest that neither melting of Pb nor lubrication (and thus low friction) across the tool–chip interface occur when machining brass with high Pb content. Instead, the observations, as summarized graphically in Figure 3.41, show that the low cutting forces are largely due to deformation of the segregated Pb inclusions in the primary deformation zone. The highly deformed Pb globules stretch along the shear plane, change shape from globular to flake-like inclusions, and act as crack initiation points in the brass matrix, so enforcing the process of discontinuous chip formation. The presented findings support Doyle's [25] conclusion about mechanical instabilities causing discontinuous chip formation. This type of chip formation restricts the contact length between tool and chip, resulting in low frictional forces and low tool temperature. Thermal measurements confirm that machining CuZn38Pb3 results in an approximately 180 °C lower tool temperature than machining CuZn42. Such low

temperatures explain the extremely long tool life of cutting tools when machining brass with high Pb content.
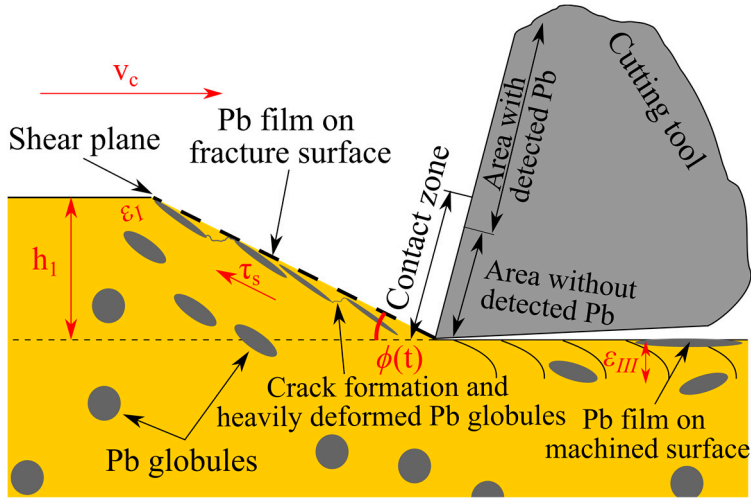
Figure 3.41. Graphical sumary of the function of Pb in machining of brass [114].

It is common to find the term 'internal lubrication' being used to describe the beneficial effects of Pb on the machining process [23; 25; 43; 113]. This term is often confusing as induced lubrication implies reduced friction. Findings presented in this section reveal that the lower apparent coefficient of friction for leaded brass is more dependent on chip formation, low tool–chip contact length, and subsequently lower feed force F_f, than on the lubricating effect of Pb. In particular, ToF-SIMS shows that Pb is sparse on the tool surface in the contact zone, see Figure 3.37. For these reasons, the term 'internal lubrication' is misleading and should not be used this context.

To summarise, the questions posed at the beginning of the section can be answered as follows:

- It is not likely that Pb melts when machining brass using cemented carbide tools and industrially relevant cutting data. Thermal imaging shows that the temperature is well below the melting point of Pb at $v_c = 200$ m/min, for the tested feed rates. No change in chip formation is seen for any cutting speed, indicating that the chip formation is not temperature dependant. Instead, evidence points to deformation of Pb inclusions and crack formation, starting at deformed inclusions, as the primary reason for the discontinuous chip formation.

- Low cutting forces can, in part, be attributed to the discontinuous chip formation. Since no continuous chips are formed, the contact length

between tool and chip is extremely short and frictional forces on the rake side are low.

- No evidence of a protective Pb film could be found in the contact zone between tool and chip on the tool's rake face. The long tool life is likely due to the low temperature in the cutting zone.

3.4 Influence of subsurface deformation on corrosion resistance

Machining of Pb-free brass alloys causes higher cutting forces, more tool wear, and less chip control as compared to machining of brass with high Pb content as shown in previous sections. The increased tool wear and cutting forces when machining Pb-free brass may lead to more subsurface deformation in finished components which, in turn, tends to lower the materials corrosion resistance. Subsurface deformation is a part of surface integrity, as introduced by Field and Kahles [119; 120], and can have a large influence on a components service life. Since more tool wear is seen for machining in Pb-free brass alloys and tool wear is a contributing factor to increased subsurface deformation [121], it is of interest to investigate the influence of tool geometry and cutting data on subsurface deformation and its link to stress corrosion cracking (SCC).

Stress corrosion cracking is a corrosion phenomenon with failure of components as the ultimate consequence. For brass products in water systems, SCC can cause leakage of water that risk extensive damages to surrounding structures [122]. SCC involves crack formation due to simultaneous effects of static tensile stresses and corrosion. The factors behind SCC can be divided into environmental factors, metallurgical factors and mechanical stress and strain [123]. For brass, it have long been known that aqueous ammonia is the principal environment associated with SCC [124; 125]. However, SCC can be caused by a wide variety of species including sulphates, nitrates, nitrites, chloride containing species and pure water [126]. Among the metallurgical factors, alloy zinc content and concentration of different alloying elements impact the susceptibility to SCC, as well as alloy heat treatments [126]. The tensile stress may originate from external load or as residual stresses induced by cold working, machining, welding or heat treatment [126]. Initiation sites are often either pits formed by pitting-, or deposit corrosion or as defects caused by forming and machining [126].

Assessment of a relationship between machining-induced surface integrity and product performance is a routine procedure for components operating in critical applications, and is well documented for Ni-based superalloys, Ti-alloys [127; 128], stainless steels [129; 130] and some brass alloys [131-133]. However, a limited

knowledge about surface integrity of machined Pb-free alloys is available, and even more scarce is knowledge regarding the corrosion resistance of such alloys after machining.

The cutting conditions chosen for producing samples are similar to those that can be found in at brass component manufacturing facilities. The samples were produced in longitudinal turning operations. The depth of cut, a_p, and cutting speed, v_c, was kept constant at 2 mm and 200 m/min, respectively, while the feed rate, f, was varied in three levels, 0.05; 0.15 and 0.4 mm/rev. Since tool wear is a major contributor to subsurface deformation and Pb-free brass reduces tool life as compared to brass with high Pb-content, a worn tool with flank-, and crater wear, VB = 0.37 mm, as well as an unworn tool with small edge radius and a large positive chip angle ($\gamma = 22.5\,°$) was used to produce high and low levels of deformation, see Figure 3.42. The profiles of the edge line, shown in Figure 3.42, was measured using a 3D-optical microscope, Alicona InfiniteFocus G4, and represents an average of 500 measured edge profiles.
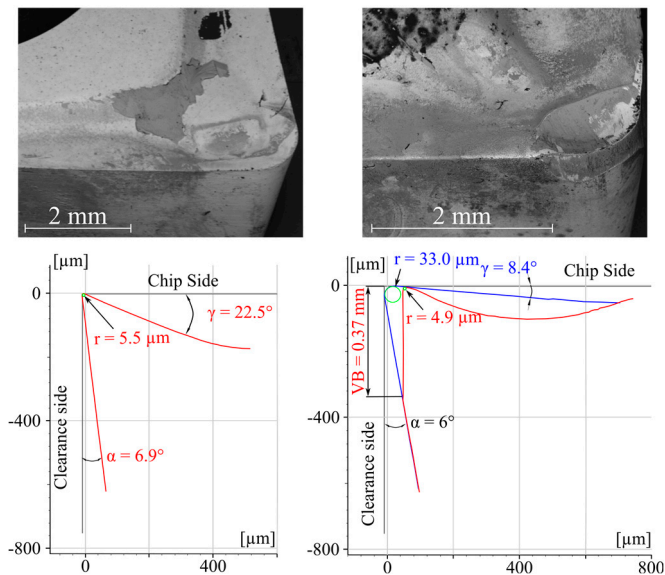
Figure 3.42. SEM image of the used tools together with cutting edge cross-sectional profiles. The blue line represents the original edge line and the red line shows the actually used edge line of the worn tool.

Two different techniques were used to quantify the depth of the subsurface deformation, micro indentation and EBSD. Both of the techniques chosen for characterization are well suited for the task and complement each other since they rely on different principles to measure subsurface deformation, micro indentation by increased hardness in the deformed material and EBSD by misorientation in the

crystallographic structure. Two materials were chosen for this investigation, CuZn21Si3P and CuZn38As. Both alloys are Pb-free and dezincification resistant, which makes them common choice for components in contact with corrosive fluids. Since it is of interest to characterize the hardness in a narrow region of the sample, a lower load of 10 mN is used in these micro hardness measurements, as compared to the micro hardness measurements shown in section 2.2.2 where the bulk micro hardness where of interest. As can be seen in Figure 3.43, the hardness distribution is different for the used materials. CuZn21Si3P contains two different phases and show a wider, non-symmetric hardness distribution as compared to CuZn38As that only contain one phase. The mean hardness value for CuZn21Si3P is 2.6 GPa, which is higher than for CuZn38As, 1.5 GPa.
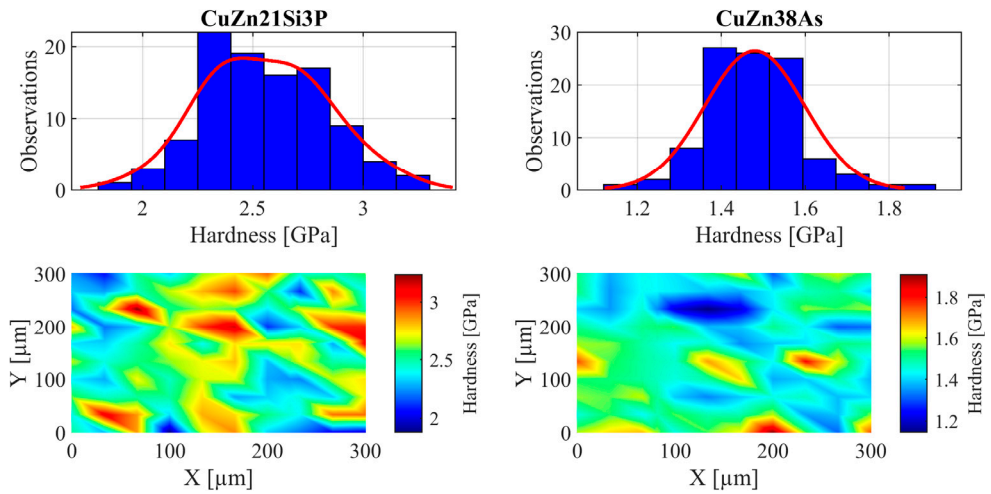
Figure 3.43. Hardness distribution for the used materials measured in a 10x10 matrix with 30 µm spacing between indents made by an Berkovich indenter and 10 mN load. Note the difference in hardness scale between the colormaps.

To characterize the subsurface deformation using micro hardness measurements, five columns of indents with internal spacing of 50 µm, were made on samples sectioned in the radial direction. Each of the column contained 15 indents with an internal spacing of 15 µm, an example of micro hardness indents and measured hardness in a sample can be seen in Figure 3.44.
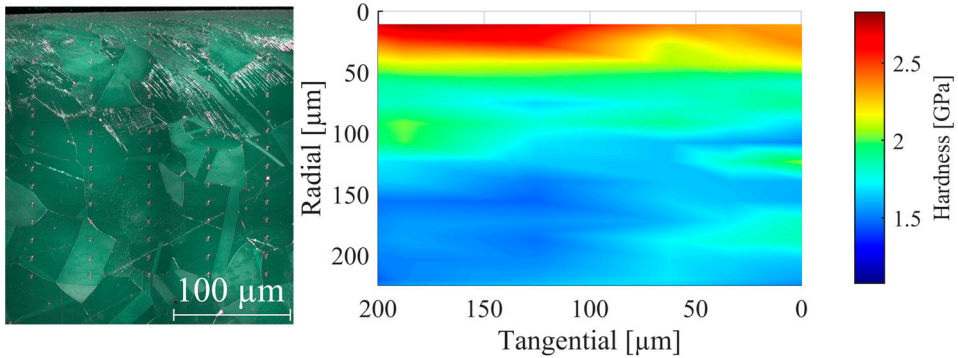
Figure 3.44. Example of micro hardness indentations captured using a light microscope with polarized light and measured hardness in the same sample, CuZn38As machined using a worn insert and $f = 0.4$ mm/rev.

For visualization of the deformation zone after machining and corrosion testing, ion beam polishing of the samples, followed by Ion Channelling Contrast Imaging (ICCI) in the same way as for the chip roots in section 3.2.2. To evaluate the susceptibility to SCC, accelerated corrosion testing in accordance with SIS 117102 [134] was performed. This test method was chosen because it was developed to evaluate the effect of processing-induced internal stresses without the influence of externally applied stress. For brass and other copper alloys, the susceptibility to SCC is commonly evaluated in accordance with standard ISO 6957 [135], in which an external applied stress is used. That standard is thus not suitable for evaluation of the impact of machining-induced surface integrity only. The different samples were exposed in separate exicators and taken out of the test solution after 30 minutes.

In longitudinal turning, the induced subsurface deformation and other surface topography and integrity characteristics are strongly dependent on the sample's orientation. When inspecting a cross section of a machined workpiece along the axial direction, the tool's nose radius will create ridges, and the spacing between the ridges is approximately equal to the feed rate, Figure 3.45 b). When inspecting a cross section of the workpiece seen along the tangential direction, the surface is curved according to the workpiece diameter, but no ridges will be formed, as can be seen in Figure 3.45 (a). Although the surface topography is different depending on analysis directions, the depth of the severely deformed material, $\varepsilon_{III,severe}$, closest to the machined surface, appears to be similar.
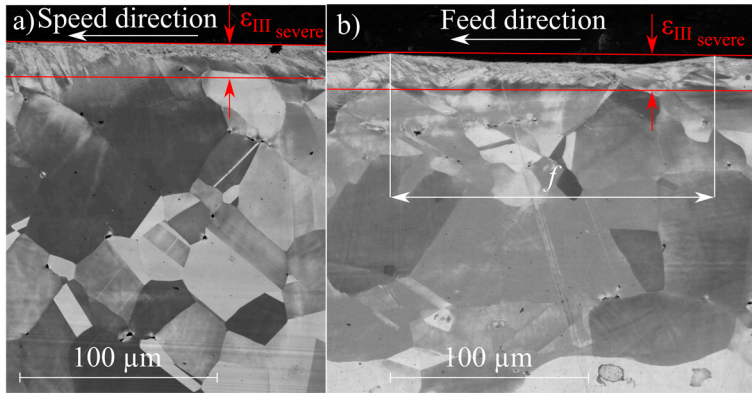
Figure 3.45. ICCI after FIB polishing of subsurface deformation with the severely deformed part marked by red arrows, for a sample cut in the radial direction, **a)**, and a sample cut in the axial direction, **b)**. The samples were prepared using a sharp insert for turning CuZn38As with $f = 0.15$ mm/rev.

Formation of subsurface deformation – i.e., its depth and degree of work-hardening is dependent on thermo-mechanical state of the being generated surface. For a given material, it is mainly controlled by cutting conditions, tool geometry and tool wear. It is known that higher feed and respective higher mechanical load cause both higher degree of work-hardening and its propagation depth [62]. Thermal softening under high cutting speeds can increase the deformation and simultaneously facilitate localization of deformation in the near-surface layer. Still, tool wear is among the most defining factors influencing subsurface deformation and subsurface damage [136]. This rather predicable and linear behaviour becomes much more complicated when machining with cutting tools having a nose radius, r [137]. Subsurface deformation that is generated during the current cut affects not only machined surface but also the temporary surface, Figure 3.46. During the sequential cut, when the tool moves one feed forward and the workpiece makes one revolution, the cutting tool might cut through already work-hardened layer, thus multiple deformation takes place. The magnitude of such multiple deformations is controlled by three parameters: tool nose radius - r, feed - f, and depth of subsurface deformation from a single cut – ε_{III}.
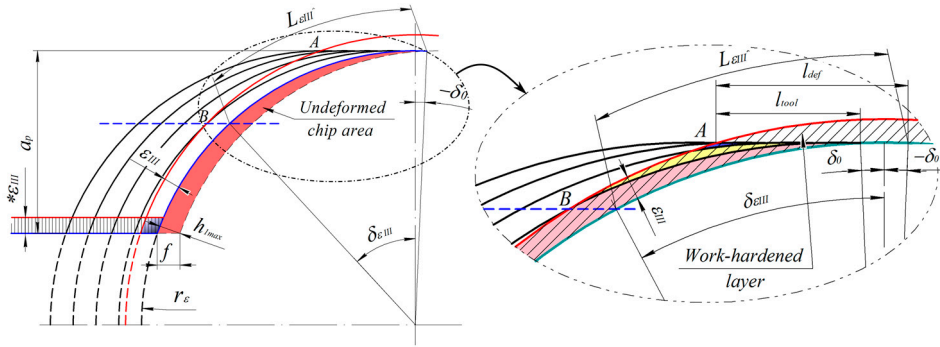
Figure 3.46. Schematic of the interaction between subsurface deformation from single and sequential cuts in lognitudinal turning with tools having a nose radius. Adopted from Bushlya et al. [137]

Involvement of so many parameters make the surface integrity response to machining operation rather difficult to predict analytically. While it is expected that machining with low feed should generate lower plastic deformation, in the case of a worn tool a rather comparable subsurface deformation ε_{III} is found for $f = 0.05$ mm/rev and $f = 0.15$ mm/rev, Figure 3.47. For both machining conditions, the depth of work-hardening is approximately 220 µm. Still, for low feed of $f = 0.05$ mm/rev the surface hardness is higher because the cutting tool passed over the surface several times. When the feed is very large and is bigger than the original ε_{III}, the tool will not re-engage with previously deformed layer and will generate lesser overall deformation, as seen in Figure 3.48 for $f = 0.4$ mm/rev.
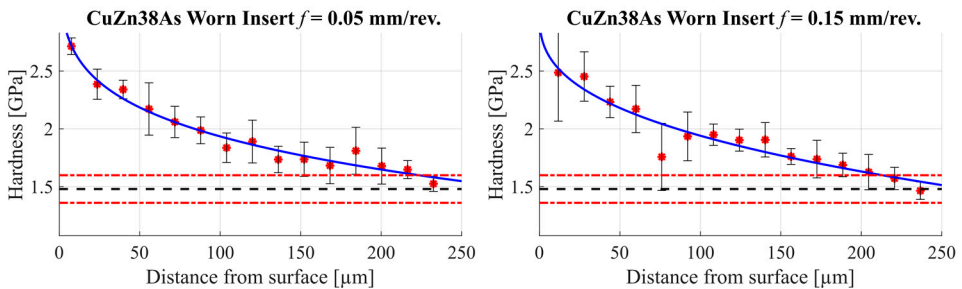
Figure 3.47. Hardness distribution for two samples machined with a worn insert and different feed. The red lines show max and min bulk hardness and the black line shows the average hardness measured in material unaffected by deformation.

While the influence of feed rate is not very significant, large differences in both depth of ε_{III} and the severity of work-hardening can be seen between the brass alloys and the different conditions of the tools. In Figure 3.50, a quotient between the local subsurface hardness, H, to the unaffected bulk hardness, H_{bulk}, is presented for all cases. For a sharp tool, machining of CuZn38As generates nearly twice deeper

plastic deformation and approx. 20% higher degree of work-hardening comparing to CuZn21Si3P. Much more severe cases are observed when machining with a worn tool. The depth is somewhat comparable for both alloys, yet the work-hardening for CuZn38As is more than 40 % higher. The severity of deformation, H/H_{bulk}, for CuZn38As is close to 2, as compared to CuZn21Si3P, where H/H_{bulk} is well below 1.5.
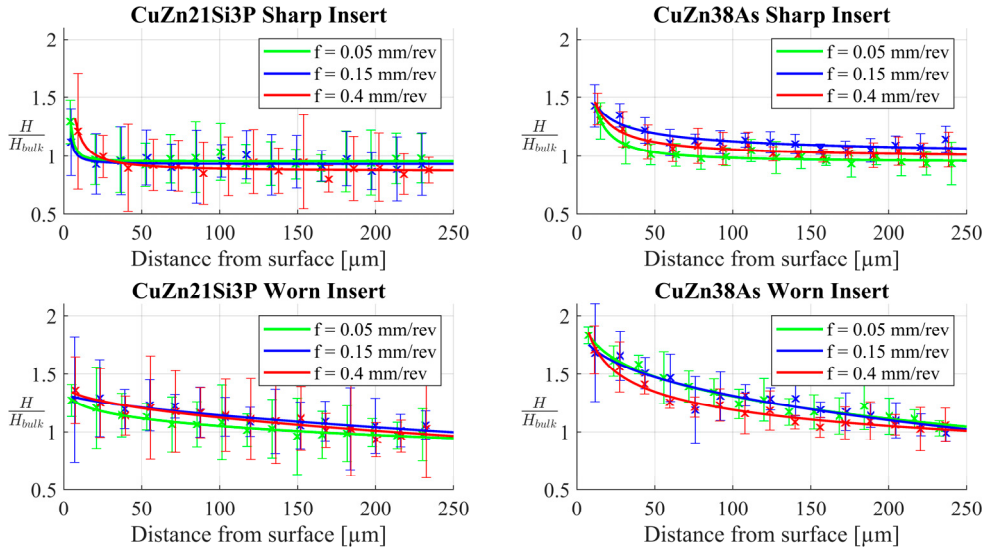
Figure 3.48. The quotient between measured subsurface hardness and the average hardness of unaffected bulk material for all used machining conditions.

Good correlation is seen between the measured microhardness profiles and the crystallographic misorientation, measured using EBSD and kernel average misorientation with a step size of 0.5 µm. At approximately the same distance from the machined surface where the hardness is within the maximum and minimum bulk hardness, the density of misorientation becomes low, see Figure 3.49. This indicates that both methods are well suited for quantification of subsurface deformation. Slightly lower quality of the analysis is seen for CuZn21Si3P which may be related to the relatively unknown crystal structure for κ′ or the smaller grain size in the material. In the severely deformed layer closest to the machined surface, it is difficult to obtain Kikuchi diffraction patterns, likely due to excessive deformation and misorientation, which results in unresolved black areas. Further investigation of $\varepsilon_{IIIsevere}$ with higher magnification and a step size of 0.05 µm reveals that the black area closest to the machined surface has a high fraction of submicron and nano-sized grains, Figure 3.50. Formation of such microstructural features in the near-surface region is typically attributed to either severe plastic deformation under conditions of high strain and low homologous temperature, T_{hom}, or dynamic recrystallisation under high strain and high homologous temperature. Dynamic recrystallisation

typically requires $T_{hom} \geq 0.5$ [138], which for brass alloys is equivalent to $T \geq 320$ °C. The temperature when machining these two brass alloys is slightly higher than this threshold for sharp tools, Figure 3.16, and even higher for worn tools. Therefore, the submicron grains are likely the result of dynamic recrystallisation, while presence of microshear bands is the result of severe plastic deformation [138], which is related to a gradient temperature reduction deeper into the sub-surface layer. These microstructural features and transformations are representative of the so-called white layer which is well studied for machining Ni-alloys and Ti-alloys [127; 128].
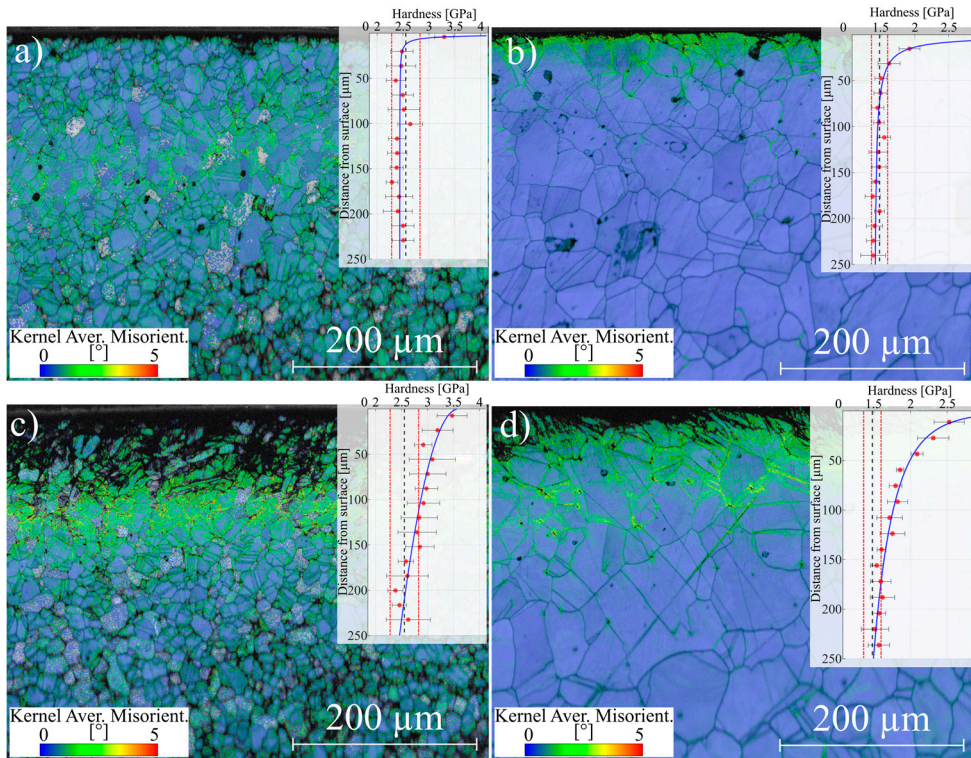
Figure 3.49. Kernel average misorientation measured using EBSD overlayed with the hardness profile for the sample, measured with micro indentation. **a)** CuZn21Si3P machined with a sharp insert and $f = 0.05$ mm/rev, **b)** CuZn38As machined with a sharp insert and $f = 0.05$ mm/rev, **c)** CuZn21Si3P machined with a worn insert and $f = 0.4$ mm/rev, **d)** CuZn38As machined with a worn insert and $f = 0.4$ mm/rev.
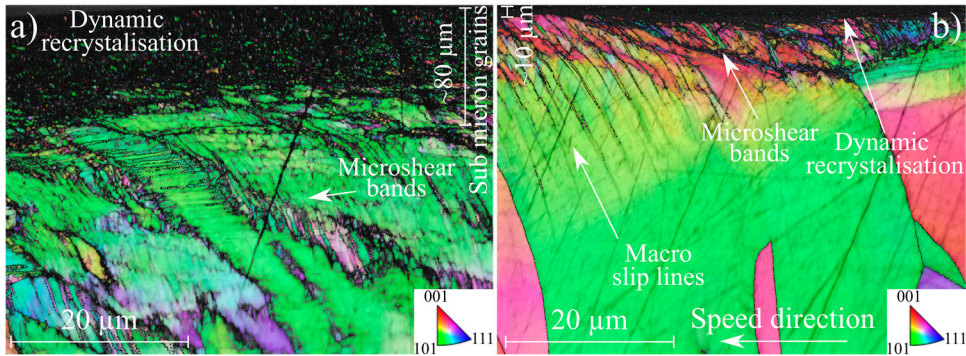
Figure 3.50. EBSD coloured according to crystal orientation at higher magnification of $\varepsilon_{IIIsevere}$ for CuZn38As machined with **a)** worn tool and f = 0.4 mm/rev. and **b)** sharp tool and f = 0.05 mm/rev.

Figure 3.51 shows the optical images of test specimens after corrosion experiments. Compared to the as-machined samples both brass alloys have a duller appearance. Spots and areas with darker coloration are visible for both alloys. This appearance is expected even at short exposure times compared to the maximum exposure time, 48 hours, referred to in guidelines to standard SIS 117102 [134], due to the harshness of the test media. For CuZn21Si3P alloy a fraction of surface has the appearance of corroded striations perpendicular to the cutting speed direction, see Figure 3.51. The fraction of corroded surface is higher for a sample machined with a worn tool. For CuZn38As alloy the corrosion striations are not observed and the surface is affected uniformly. However, the cracks propagating from the surface into the bulk material are present on the CuZn38As sample machined with a worn insert, and these cracks propagate also perpendicularly to the cutting speed direction. The cracks are spaced rather uniformly, approximately 30-50 µm apart, see Figure 3.51. The difference in the cracking behaviour of the alloys cannot be attributed to a difference in the surface topography. Surface roughness before and after exposure is comparable for equivalent feeds and tool wear conditions, as shown by the surface profiles extracted from measured 3D surfaces.
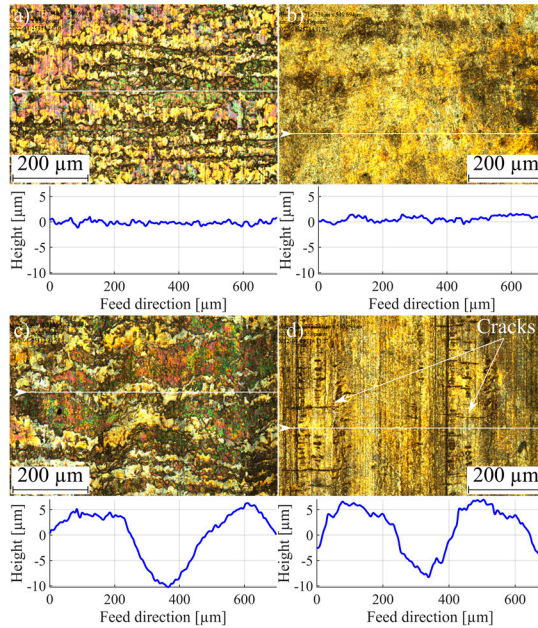
Figure 3.51. Optical images of test specimens after 30 minutes exposure and respective surface roughness profile, measured as indicated by the white arrow. **a)** CuZn21Si3P machined with a sharp insert and $f = 0.05$ mm/rev, **b)** CuZn38As machined with a sharp insert and $f = 0.05$ mm/rev, **c)** CuZn21Si3P machined with a worn insert and $f = 0.4$ mm/rev, **d)** CuZn38As machined with a worn insert and $f = 0.4$ mm/rev.

Cross-sectioning of the corroded samples was performed in the cutting speed direction, which was followed by mechanical grinding, polishing and ion beam polishing. Ion Channelling Contrast Imaging (ICCI) was used to analyse the effect of subsurface deformation on the stress cracking corrosion, because EBSD was not able to resolve the severely deformed near-surface region (see Figure 3.50) where crack initiation and propagation is expected. Despite the very different degree of work-hardening (see Figure 3.48) for CuZn21Si3P samples machined with a sharp and worn tools, cracks were not found in any of the samples, see Figure 3.52. The cross section of CuZn38As machined with a sharp tool revealed a plastic deformation, identical to as-machined samples, yet without distinct localized corrosion defects and cracks. On the contrary, CuZn38As sample machined with a worn tool has a series of cracks perpendicular to the surface. Figure 3.53 shows a detailed view of a crack, which extends approximately 45 µm into the material. The crack originates on the surface and propagates until it meets the grain boundary where it is deflected. Several similar cracks were found in the sample.
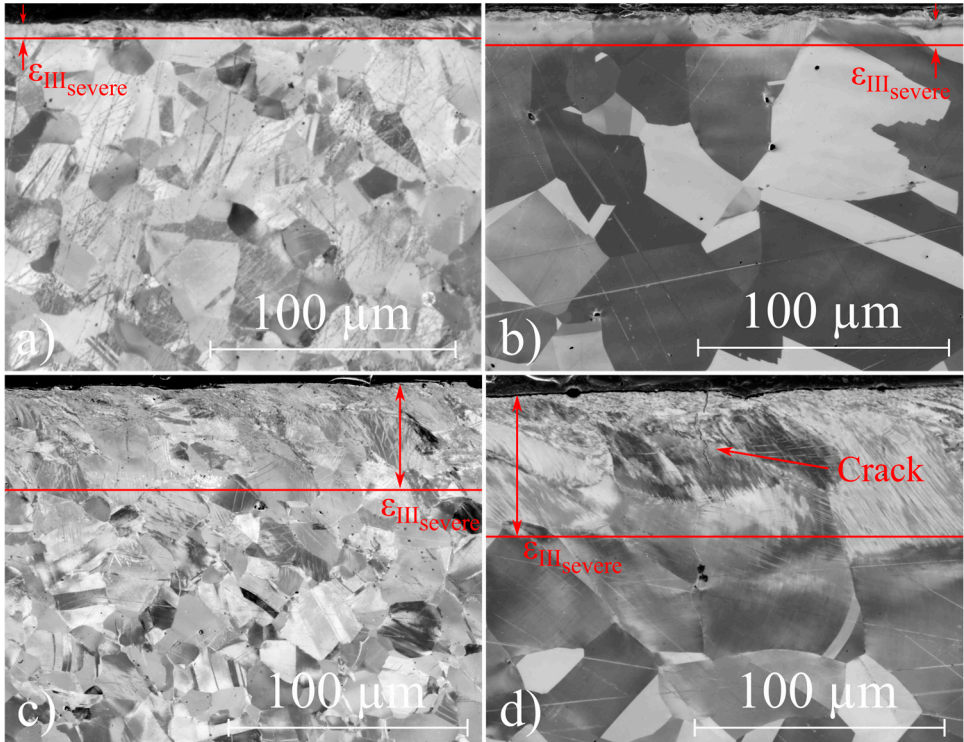
Figure 3.52. ICCI after corrosion test. **a)** CuZn21Si3P machined with a sharp insert and $f =$ 0.05 mm/rev, **b)** CuZn38As machined with a sharp insert and $f = 0.05$ mm/rev, **c)** CuZn21Si3P machined with a worn insert and $f = 0.4$ mm/rev, **d)** CuZn38As machined with a worn insert and $f = 0.4$ mm/rev.
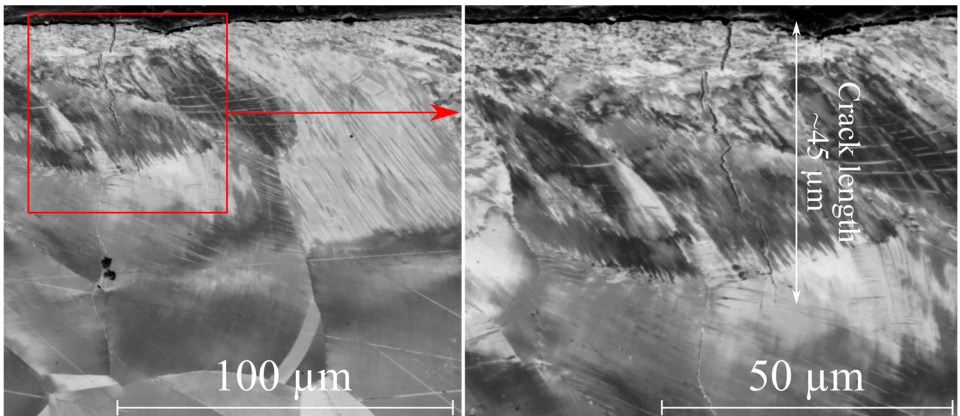
Figure 3.53. Detailed view of the crack formation in CuZn38As machined with a worn insert and $f = 0.4$ mm/rev. The crack is approximately 45 µm deep and several similar cracks were found in the sample.

The observed behaviour of the two brass alloys can be attributed to several different factors. Higher zinc content in the alloys is known to increase the susceptibility to SCC [126]. CuZn21Si3P contains 21 wt.% Zn while the Zn-content in CuZn38As is 37 wt. %. Thus, the lower zinc content in CuZn21Si3P is a possible factor behind is absence of cracking in these samples. Still, it is likely that more prolonged exposure will cause the cracking in the silicon brass. As seen from nano-indentation (Figure 3.48) the degree of work-hardening for this alloy was lower compared to CuZn38As, thus more favourable stress state can be expected. At the same time, silicon brass has nearly 3 times lower thermal conductivity [35] and therefore higher tensile residual stresses are expected [62]. Hence, complementing the surface integrity analysis with residual stresses should be able to further clarify the observed difference in the accelerated corrosion test.

Still, it should be noted that the performed accelerated test in the environment according to SIS117102 is very harsh for brass products compared to real working conditions. The actual impact of surface deformation and residual stresses on SCC can only be achieved by evaluation of machined brass products after field exposure. Therefore, it can be recommended to install test components manufactured with sharp and worn tools in real water handling systems to evaluate the SCC susceptibility from a component life-time point of view. Likewise, prolonged exposure time for the specimens of CuZn21Si3P necessary to identify which subsurface defects act as initiators for stress corrosion cracks. In this study only one sample of each machining condition was exposed to the corrosion test, which is hardly enough data for any definitive, general statements on the materials resistance to SCC. However, investigations show that subsurface deformation is deeper and more severe in machining of CuZn38As compared to CuZn21Si3P under identical machining conditions and that cracks were only found in CuZn38As machined with a worn insert and $f = 0.4$ mm/rev.

3.5 Discussion and conclusions

When switching from brass with high Pb content to Pb-free alloys, reduced machinability is one of the largest problem areas for the manufacturing industry. Machining Pb-free alloys results in higher cutting forces and more continuous chip formation, which has several effects on the outcome of the machining process. The machining strategies commonly employed in the brass industry are based on machining brass with high Pb content with large form tools and step drills. These tools are very effective in removing material quickly due to a large depth of cut and complex tool geometry that can machine several surfaces simultaneously. Section 3.2.1 showed that the cutting resistance is higher for Pb-free alloys than for alloys with high Pb content and that this becomes more evident the greater the depth of cut used in machining operations. One way of lowering the cutting resistance is to use

a positive rake angle, as shown in Figure 3.13. However, the complex geometries already inherent to form tools can make it difficult to manufacture tools with other than neutral rake and inclination angles with efficient, exact and repeatable methods.

Given the limited possibilities for changing the tool geometry of form tools, careful consideration and evaluation of appropriate machining strategies is needed when changing production from brass with high Pb content to Pb-free brass. A possible solution for problems with chip handling is to move towards more intermittent machining operations, for example, using milling rather than turning. In general, a transition from turning to milling requires major investment in new machines, but not all turning operations are problematic. Ideally, operations where chip handling is seen as problematic could be moved to a milling machine, but this can be highly disruptive in a product flow that consists of several consecutive steps. The problems in implementing Pb-free brass should, however, not be exaggerated. As is shown in section 3.1.3, a large number of components can be manufactured in Pb-free brass without major changes to machining strategies and cycle time.

Tool wear will be higher when machining Pb-free brass compared to alloys with high Pb content, all other parameters being equal. The increase in tool wear is likely related to the higher tool temperature seen for Pb-free brass under varying cutting conditions (Figure 3.16). Temperature, differences in concentration of elements and reactivity are the driving forces for the chemical and diffusional wear that are the most likely degradation mechanisms for a cemented carbide cutting tool used on brass. The investigation of the contact area between tool and chip showed no formation of a protective layer of Pb in machining of CuZn38Pb3. If such a layer had been detected, it could have explained the low wear rate, but since Pb was mostly detected outside the contact area it is difficult to see how Pb is directly involved in prolonging tool life. Pb does, however, provide other machinability enhancing features, mainly related to chip breaking.

Short chips have benefits in machining other than being easy to evacuate from the machine. When short chips are produced in the machining process, as when machining brass with high Pb content, the contact length between tool and chip is low. Keeping the contact length short allows less time for heat transfer from the hot chip, so reducing tool temperature. The highest tool temperature is normally found in the sliding zone [113], but due to the short chip length, no sliding zone is seen on the tool in machining CuZn38Pb3 and the highest tool temperature is found at the cutting edge. Consequently, if the contact length between tool and chip is short, the frictional forces on the tool's rake face must be low compared to machining that produces continuous chips.

Some clear differences in chip formation can be seen between the Pb-free alloys. The duplex alloys produce segmented chips with visible shear bands, while α-brass has a very homogenously deformed chip. In machining, the α-brass behaves much like pure copper, although with lower ductility and higher strength provided by the

solution hardening effect of the added zinc. If chip breaking and evacuation are important in a manufacturing situation (e.g., for internal turning, internal groove making or drilling of small holes) and the requirements on the components allow it, there is a clear advantage to using duplex brass.

The two duplex brasses investigated in the dissertation do have some differences between them, both in mechanical properties and machining behaviour. CuZn21Si3P is a stronger alloy with lower thermal conductivity that produces more segmented chips compared to CuZn42. The heavy segmentation seen for the material makes the chip form semi-continuous, especially at high feed rates. Even though CuZn21Si3P is mechanically stronger and has lower thermal conductivity than all the other tested brass alloys, the measured cutting resistance and tool temperature are lower than for the other Pb-free alloys.

Due to the high Cu-content of CuZn21Si3P, the price for the material is higher than for the other brasses. The high Si content of the alloy also causes problems in manufacturing sites since the waste material from production (i.e., chips) needs to be kept separate from other alloys to avoid polluting the material stream to recycling. This makes it necessary to thoroughly clean the machines if Si-brass and other brass alloys are machined using the same equipment, which results in long setup times. Long setup times in combination with higher material price naturally lead to higher production costs. However, it is possible that the higher machinability of CuZn21Si3P may contribute to fewer disruptions, such as downtime and quality losses. In an ideal production scenario using both Si-brass and other brass alloys, it could be beneficial to have machines that are restricted to specific types of brass. Doing so might reduce the flexibility in the factory, but setup times could be shorter, making production of smaller batches viable.

4 Recycling brass chips in the solid state

Using machining to manufacture components will always result in scrap material in the form of removed material, or chips. When manufacturing small, hollow components, such as pipe fittings, the majority of the raw material being used to make a component may be converted into chips.

Brass has a very high degree of recycling between manufacturing sites and raw material suppliers. The chips from the manufacturing sites are sent back to the raw material supplier for remelting into new raw material, creating a loop where material is sent back and forth between the sites. By introducing on-site recycling of waste material from manufacturing processes, it may be possible to promote more sustainable production. The developed method of solid state recycling will henceforth be called *chip forging.*

In this section, the development of a method of on-site recycling in the solid state will be presented and evaluated.

4.1 Motivation for developing chip forging

All industries must strive for a sustainable future. The purpose of developing a direct recycling process is to increase the degree of utilisation of the workpiece material without remelting the material, so increasing the sustainability of the manufacturing of brass parts.

The United Nations has defined seventeen goals for sustainable development [139]. These goals include targets for efficient use of natural resources (goal 12.2) and reduction of waste generation through prevention, recycling and re-use (goal 12.5). While pursuing these goals, a company needs to be profitable in order to be able to develop its operations and make relevant investments. The proposed recycling method has a potential to help meeting these goals by reducing the use of raw material, the transportation of material, and the energy consumed in the recycling process. If the potential of the method is realised, implementation of it could reduce the environmental impact of brass industries.

According to Jovane et al. [140], sustainable development can be divided into three main domains: societal, economic, and environmental. When all three domains interact, sustainable development can be achieved. Chip forging can potentially influence the environmental domain by reducing emissions from recycling and activities related to recycling, such as transportation. If it is possible to replace some of the stock material needed to make components, the economic domain will be influenced. As shown in Figure 4.1, the price for materials needed to make brass fluctuates. Between 2019 and 2022 the price for pure copper varied between 410 and 950 EUR/100 kg [141]. These large fluctuations can make it difficult to price products in a way that makes them affordable for potential buyers but still profitable for the producing company.
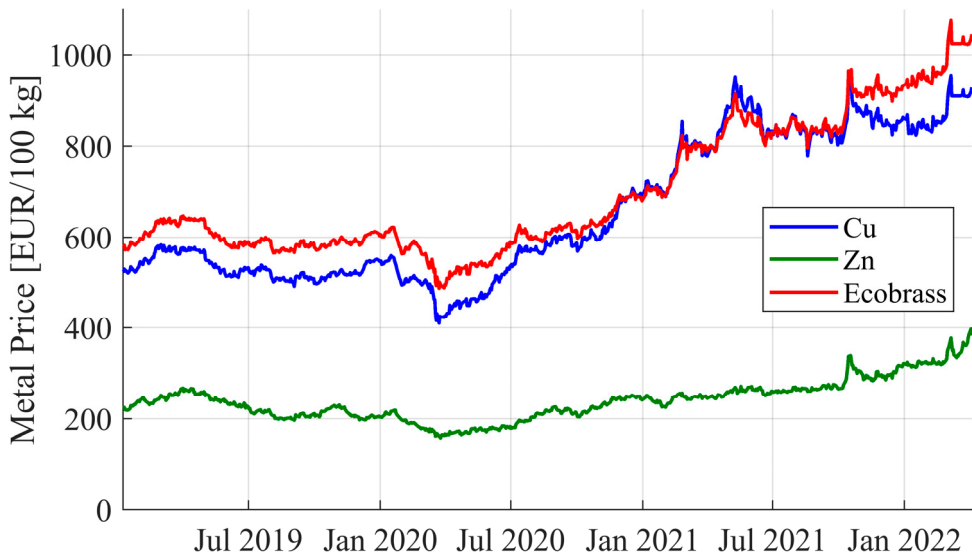
Figure 4.1. Metal price for Cu, Zn and Ecobrass (Wieland Werke's trade name for CuZn21Si3P) between 2019-01-07 and 2022-04-05 [140].

To promote the use of chip forging at companies not specialised in advanced material processing (i.e., small- and medium-sized part manufacturing enterprises), the process of chip forging should be kept relatively simple while still achieving the right quality for the produced components.

4.2 Description of chip forging

The basic idea for chip forging is to take advantage of the large plastic deformation at elevated temperatures that occurs in the hot forging process. It is hoped that by compacting chips into a green compact that can be handled and heated to the desired

temperature before being placed in a forging press, parts of the required quality can be produced. The high heat of hot forging (~750 °C for brass forging) promotes diffusion between the chips, and the large plastic deformation can make the porous green compact solid and homogeneous.

Two components have been chosen to demonstrate the method. Machining blanks for the two components can be seen in Figure 4.2. These blanks are forged from rod material and machined to final geometry. To manufacture the thermostatic valve housing denoted a) in Figure 4.2, 202 g of rod material is needed. The final component weighs 90 g after machining, giving a material utilisation of 44.6 %. In the manufacturing process, material will be removed in several steps to achieve the final geometry. The rod will be cut to a suitable length before forging, flash will be removed after forging, and finally the component will be machined. Most of the material removal will be done in the final machining step.
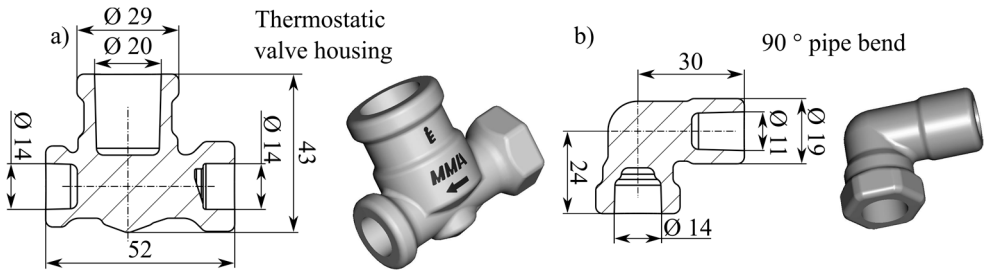
Figure 4.2. Demonstrator components chosen for chip forging as machining blanks [142; 143].

The removed material is commonly sent back to the material supplier for recycling [144]. This transportation of chips is not a value-adding process. If it were possible to re-use the material on-site, the cost of production and the environmental impact could be reduced.

Several different processes for material reclamation after machining have been reported, with promising results [145-151]. Duflou et al. [145] showed that the environmental impact of aluminium recycling can be reduced by a factor of 2 by implementing plasma spark sintering, and by a factor of 3–4 by implementing hot extrusion. Schemes for direct recycling have been developed for several other material groups using powder metallurgy (PM) [152]. Da Costa et al. [153] showed that it is possible to produce parts in grey cast iron by grinding metal cutting chips into a powder for subsequent pressing and sintering. A similar approach with pressing and sintering was tested on brass by Philips and Basheerkutty [154], who found that sintering of alloys that contain Zn can be problematic as the evaporation of Zn at high temperatures and prolonged sintering time changes the material's chemical composition. The same problem of zinc evaporation in the production of brass parts using powder metallurgy was reported by Radomyselskii et al. [155].

Methods for direct recycling of brass were developed individually by Nakagawa et al. [156] and Manukyan et al. [157].

In the early stages of developing this method, chips from machining CuZn38Pb3 were used. These chips were produced under dry cutting conditions and were therefore not contaminated with oil. The fact that chips from CuZn38Pb3 are very small compared to those from machining other brass alloys makes the compaction step more practical.

An experiment was conducted to determine the effect of particle size distributions on mechanical properties in the compaction stage. Cylindrical green compacts were made using a compaction pressure of 800 MPa. The results showed that a size distribution smaller than the size distribution of the machining chips did not have a significant impact on the relative density or microstructure of the forged parts [142]. As a result, a multimodal size distribution of chips was used in the next experiments.

The initial experimental series also showed that it was difficult to handle the green compacts and move them to the forging die, especially using automated handling equipment. To overcome this, an intermediate forging step was introduced in which the green compact was forged into a slightly smaller cylindrical shape before being forged into a machining blank, see Figure 4.3.
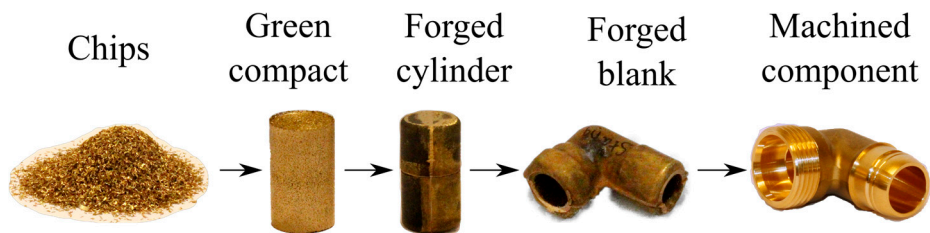
Figure 4.3. Process steps used in developing chip forging.

Using the process steps shown in Figure 4.3, a test batch of eight blanks, with the geometry shown in Figure 4.2 b), was produced. The blanks were subsequently machined into finished components that were subjected to a standardised acceptance test. In the acceptance test, the components were assembled with a nut that was tightened with 30 Nm, the assembly was filled with water and pressurised to 13 bar for 15 s. To pass the acceptance test, no leakage or pressure drop was allowed during this time. Of the eight tested components, five passed the acceptance test, giving an acceptance rate of 63 %. For components manufactured from rod material, the acceptance rate is close to 100 %. The components that did not pass the acceptance test broke when the nut was tightened to the specified torque on the threaded section.

By examining the microstructure of the forged components, the reason for breakage under moderate stresses such as tightening a nut to the specified torque becomes clear. Close to the edge of a forged blank, shown in Figure 4.4, an open chip

structure is visible, but further into the bulk of the blank, the material is more solid. Although the material is more solid further from the edge of the blank, porosities and remnants of the chips are visible, indicating weak points in the material.
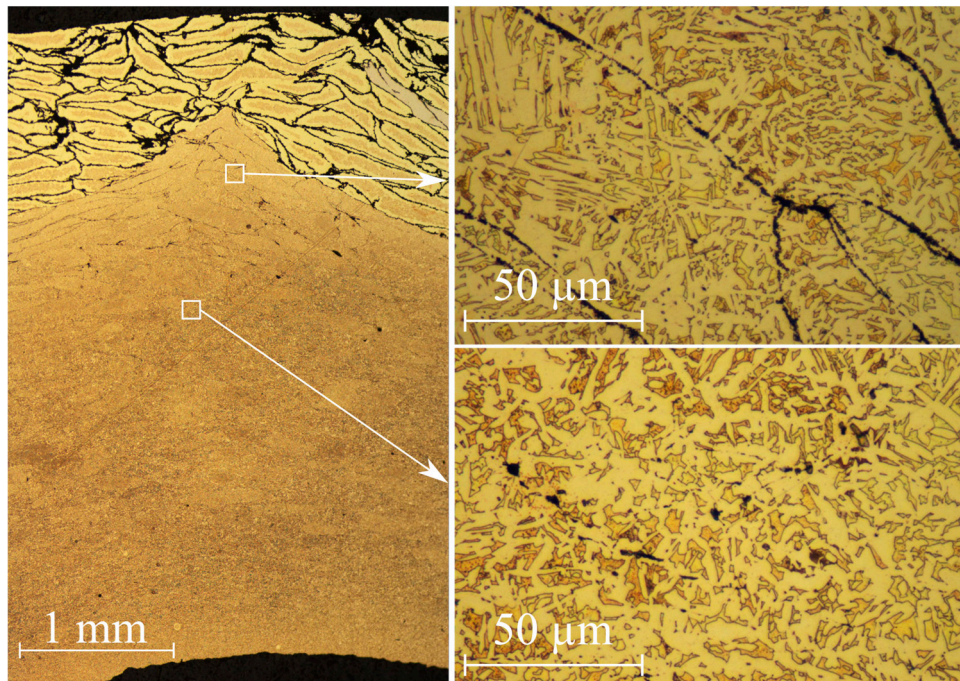
Figure 4.4. Microstructure of a chip forged blank [157].

Since partial bonding between the chips is achieved in the forging process, it is of interest to investigate whether the chemical composition is constant over the partial bond. Measurements with XEDS over areas with an open chip boundary and an area where the material appeared to be solid are shown in Figure 4.5. In the open chip boundary (Line 1), low levels of copper and zinc are measured with increased amounts of lead and oxygen, whereas measurements in the area which bridges the open chip boundaries show an even elemental distribution. The area between the open chip boundaries is, with a high probability, successful material bonding in the chip forging process. Additionally, XEDS analysis showed no changes in the chemical composition of the material after forging.
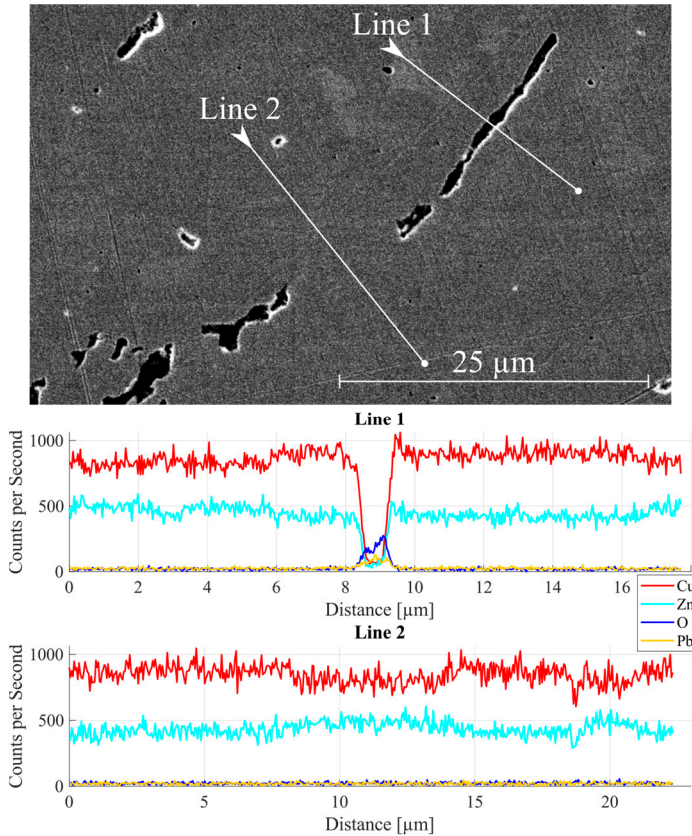
Figure 4.5. Chemical composition in a forged blank over the two marked lines [142].

In the above cases, the green compact was forged into a cylinder before being forged into a machining blank. The extra forging step was introduced since it was found to be difficult to handle the green compacts in the forging process. Hot compaction, another way of producing more durable green compact, was also tested. Hot compaction of chips should have several advantages over forging in two steps as one process step can be eliminated and the material does not need to be heated to forging temperature twice. By heating a mould and chips, small green compacts were produced using the same amount of chips, 6 g, at different temperatures, Figure 4.6. Since the same weight of chips was used to make samples with the same diameter, the samples' density is inversely proportional to their height. The density of the compacted samples increases with increased process temperature. The durability of the hot compacted samples was deemed sufficient for direct forging at compaction temperatures above 400 °C.
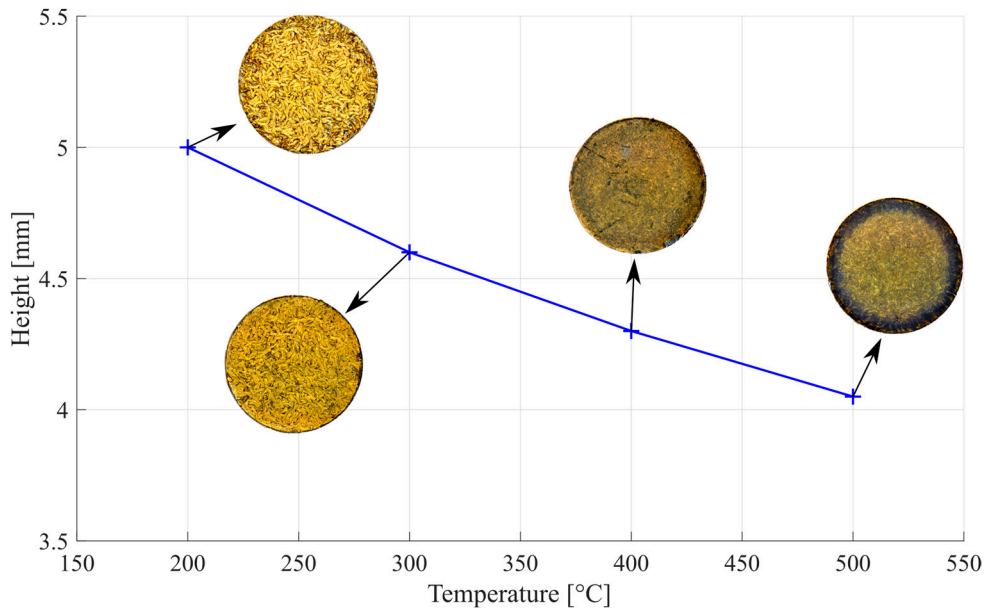
Figure 4.6. Height of hot compacted cylinders. The cylinders have the same weight and diameter. Modified after Johansson and Ivarsson [158].

The process route shown in Figure 4.7 is suggested for industrial implementation of chip forging. It includes a milling step if chips from metal cutting operations have a size distribution that is not suitable for compaction. As explained in section 3.3, the chips from alloys with a high Pb content will be small, but if another alloy is used a milling step is necessary to reduce the size of the chips.

The process route shown in Figure 4.7 also includes an oil separation step as the chips may contain oil in the form of cutting fluids. Lubrication is needed in the compaction process, but the remaining lubricant from the cutting process may be an inappropriate type or the wrong amount. The samples previously discussed were made using chips from turning CuZn38Pb3 in dry conditions.
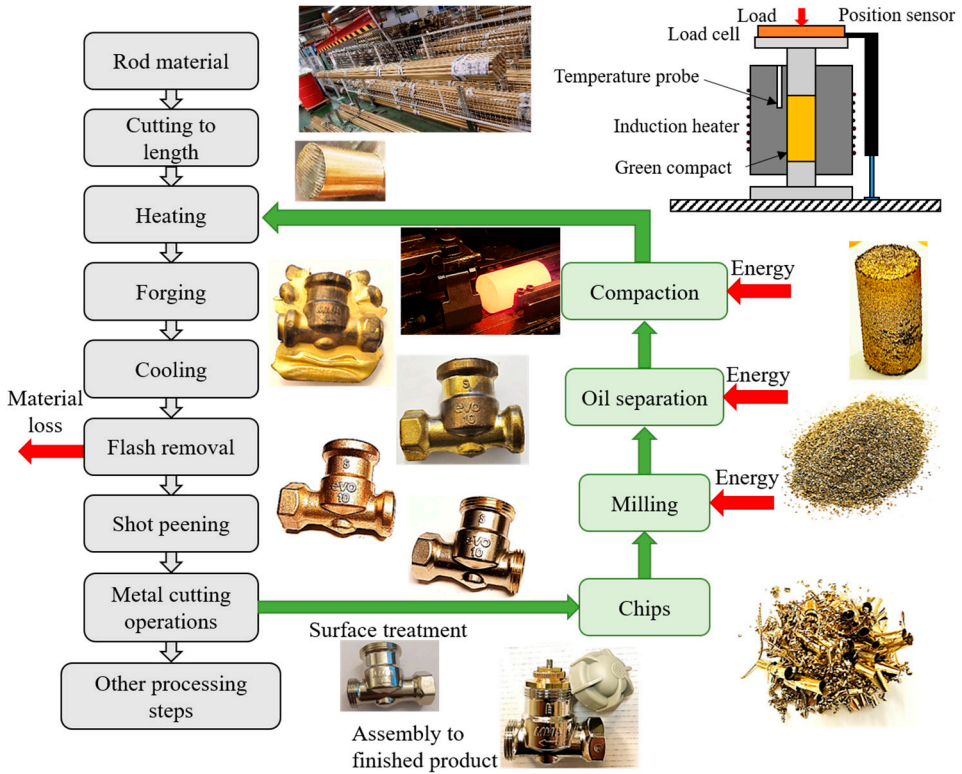
Figure 4.7. Suggested process route for chip forged components. [159]

4.3 Evaluation and optimisation

After showing the feasibility of chip forging using the Pb-containing alloy CuZn38Pb3, the Pb-free alloy CuZn21Si3P was used in further development of chip forging. The geometry of the forging blank was also changed to the thermostatic valve housing shown to the right in Figure 4.2. Based on the results of the experimental series on hot compaction, green compacts were produced at 400 °C before forging into machining blanks.

Because several process parameters can affect the quality of the chip forged component, the effect of these parameters on the finished component needs to be established. One of these parameters is lubrication, which is needed in the production of green compacts to reduce friction between particles and extend the lifetime of the compaction tool [160]. Large amounts of mineral oil are normally found mixed in with chips from metal cutting. It is a common practice in the brass

machining industry to use flood cooling with mineral oil. Since mineral oil is commonly used in brass machining, it is logical to investigate how well it works as a lubricant when producing green compacts, and its influence on the finished component. More environmentally friendly alternatives to mineral oil are also available, where vegetable oils such as rapeseed oil are seeing increased industrial usage. Vegetable oils have some advantages over mineral oils, such as improving the work environment in factories and reducing the need for fossil-based additives. Additives such as graphite can be used to attain good performance from vegetable oils in metal cutting [161]. Rapeseed oil with and without added nano-sized graphite platelets (GnP) was thus tested as a lubricating alternative in the compaction process. The GnP was produced by sonication of thermally expanded graphite in a 10 vol.% alcohol solution with 1 g thermally expanded graphite per 120 ml solution. As the optimal concentration of GnP in vegetable oil was not known for this application, three different concentrations of oil with additives were prepared (0.1, 0.2 and 0.4 vol.%).

Turning CuZn21Si3P in dry conditions resulted in chips that were up to 10 mm long, too long to be compacted directly. Table 4.1. shows the chip size distribution after jar milling using rollers for 20 minutes. Since the effect of using different lubricants would be examined, it was essential that the used chips be clean of contaminants before compaction. Accordingly, the chips were washed in acetone and dried before being mixed with the chosen lubricant.

Table 4.1. Chip size distribution of the chips after milling determined by sive granulometry.

Chip size	Fraction [%]
>1 mm	14.3
1-0.8 mm	33.2
0.8-0.6 mm	26.6
0.6-0.4 mm	20.5
0.4-0.2 mm	5.2
<0.2 mm	0.1

Different amounts of lubricants, 0.1, 0.2 and 0.3 wt.%, were added to the chips before compaction. Additionally, green compacts without added lubricants and blanks from rod material were produced. Each experimental condition was repeated three times, giving a total of 51 samples for 17 different experimental conditions.

Some effect is expected from the different experimental conditions, and quality parameters need to be chosen to be able to evaluate this effect. The density of the green compact indicates how well compacted the chips are after the first process step. Density after forging shows how much porosity is left in the forged machining blank. Densities of material after both processing steps are indicators of how successful these steps have been. Density was measured using the buoyancy method.

The highest mechanical load the manufactured component will be exposed to during the use phase of its life cycle is likely the torque applied when being installed. Therefore, it is important to maximize the chip forged component's maximum shear strength before failure. The test setup for torque testing is shown in Figure 4.8. A constant circular motion was applied on the hexagonal part of the component with a constant speed of 0.56 °/s while the applied torque was measured using a Kistler quartz dynamometer, Type 9275, until failure. This test is seen as equivalent to torquing the input hex end of the housing. To limit the torque to the measuring range of the torque sensor, a Ø15 mm through hole was made in all components. Due to variations in wall thickness after making the through hole, shear stress at the maximum torque was approximated using equation (9), where τ_{max} is the maximum shear stress, M_{max} is the measured torque at breakage, R is the radius of the hole in the tested component, and h is the smallest wall thickness. The equation is only valid for linear deformations and is therefore considered an approximation of the shear stress in this case, since metals generally break after plastic deformation occurs. Maximum shear stress is also chosen as a quality parameter.

$$\tau_{max} = \frac{M_{max}}{2\pi \cdot R^2 \cdot h} \tag{9}$$

As shown in Table 4.2, high relative green densities between 95.7– 98.7 % of the material's theoretical density were measured for all samples. The highest relative density is found for the samples made without any lubricants. After forging, all samples show a high relative density, between 97.0–98.7 %, which is 2–3 % higher than for the green compacts.
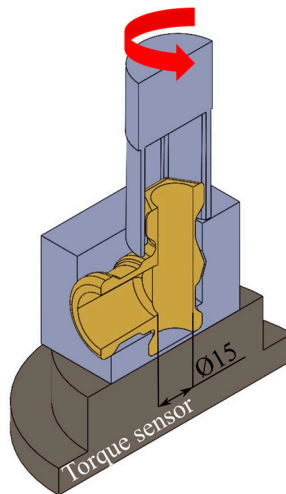
Figure 4.8. Section view of test setup for torque testing. [143]

Table 4.2. Average values for different measured physical properties.

	Relative Green Density [%]	Relative Forged Density [%]	Maximum Shear Stress [MPa]
Mineral oil 0.1 %	97.7	98.7	358.3
Mineral oil 0.2 %	96.7	98.2	407.8
Mineral oil 0.3 %	97.4	98.6	386.1
Rapeseed oil 0.1 %	97.5	98.4	358.3
Rapeseed oil 0.2 %	96.2	98.5	329.7
Rapeseed oil 0.3 %	95.7	98.2	353.6
Rapeseed oil 0.1 %, GnP 0.1 %	97.5	97.0	350.3
Rapeseed oil 0.2 %, GnP 0.1 %	97.1	97.1	289.5
Rapeseed oil 0.3 %, GnP 0.1 %	95.9	97.7	-
Rapeseed oil 0.1 %, GnP 0.2 %	97.1	98.0	-
Rapeseed oil 0.2 %, GnP 0.2 %	96.8	98.7	332.9
Rapeseed oil 0.3 %, GnP 0.2 %	95.8	98.3	333.9
Rapeseed oil 0.1 %, GnP 0.4 %	97.9	97.9	380.0
Rapeseed oil 0.2 %, GnP 0.4 %	96.6	98.2	310.8
Rapeseed oil 0.3 %, GnP 0.4 %	96.2	98.3	408.9
No lubricant	98.7	98.4	362.1
Rod	N/A	100	433.2

The results of the torque test show a relatively high strength for the forged components. The maximum shear stress depends significantly on the green compact preparation method (i.e., the lubrication strategy). The average for an experimental condition is shown to be from 6 % to 33 % lower compared to rod material. High component strength is found in samples with mineral oil with a concentration of ~ 0.2 wt. % and rapeseed oil of 0.3 wt. % with 0.4 vol. % GnP suspension. These results suggest that there could be an optimal concentration of oil and GnP additives to achieve the highest component strength. Paper V describes a detailed statistical analysis to characterise the obtained experimental data and estimate the best combination of lubricants and the GnP oil. The analysis showed that the amount of oil used in a sample did not have a significant effect on the density of the forged sample, but the concentration of GnP additives was important at a 5 % significance level. The initially used linear model for describing the dependence of maximum shear stress of the samples based on concentrations of oil and GnP is not sufficient. The quality of approximation was relatively low ($R^2 = 0.583$), indicating either a non-linear relationship, deficiencies in data collection, or too small a data set.

Curve fitting with a cubic spline surface was applied to the results to visualize the experimental data. Figure 4.9. shows the results of interpolation as a contour plot for the samples' forged density and maximum shear strength as a function of oil and GnP suspension concentrations. The accuracy of interpolation with cubic spline is $R^2 > 0.97$. The results of the curve fitting show that a concentration of GnP suspension of 0.2–0.25 vol. % in the oil and 0.15–0.2 wt. % oil mixed with the chips before compaction affects both the density and strength of forged samples in the desired direction (i.e., towards higher density and maximum shear stress).
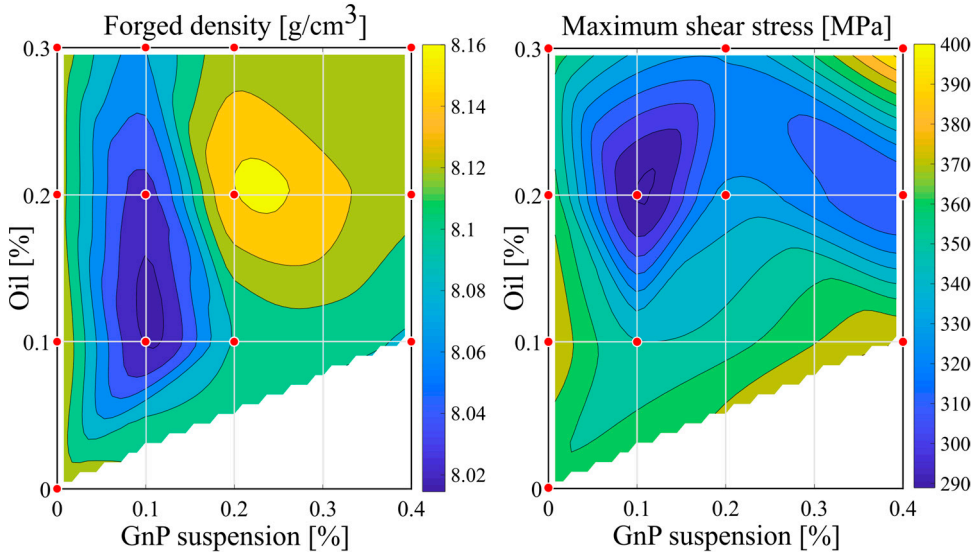
Figure 4.9. Contour plots of interpolation using cubic spline for all samples average forged density (left) and maximum shear strength (right) [143].

Using chip milling, compaction and forging, it is possible to produce machining blanks from metal cutting chips although with reduced mechanical strength. The maximum shear stress in components made using chip forging is from 6 % to 33 % lower than that of the base material. Further development of the method is needed to find optimal process parameters. The tests showed that liquid lubrication is a suitable additive, but solid lubricants should also be investigated. The applicability of the investigated method is influenced by several other parameters that were not discussed in this study, including compaction pressure and temperature, forging temperature, and the long-term effects on the chemical composition and mechanical properties of the material. Other factors such as suitable geometry for the method on both finished blank and green compact as well as economic viability are also of great interest. In addition, it is important to investigate whether chip forging actually consumes less resources than traditional recycling of brass via remelting.

4.4 Environmental impact

Chip forging has the potential to save energy and reduce emissions impacting climate change by avoiding melting of material and transportation between raw material suppliers and manufacturing sites. However, to evaluate the merits of the chip forging from an environmental point of view, it is important to evaluate the whole material lifecycle compared to traditional methods considering singular effects. Life cycle assessments (LCA) are commonly used to assess and quantify the

environmental impact of products and services [162]. The difference between the two recycling methods compared starts after metal cutting chips have been produced by a parts manufacturer, so this will be the starting point of the LCA.

In an LCA, impacts are assessed over the product's life cycle. Cradle-to-grave LCA includes raw material extraction, production, use and final disposal. Cradle-to-gate LCA includes only a certain part of the life cycle, such as from raw material extraction to production. In this study, a screening cradle-to-gate LCA was conducted to compare the environmental impacts of producing one thermostatic valve housing via chip forging with conventional production including recycling.

A vital part of LCA is the definition of a functional unit and system borders, which provides a quantitative measure to which all impacts are related. In this case, the functional unit was set to one (90 g) thermostatic valve housing. The cumulative energy demand (the primary energy consumption quantified in MJ equivalents) and the climate change impact (the contribution to global warming quantified in kg CO_2 equivalents) were calculated for the two compared systems in relation to this functional unit. The cumulative energy demand [163] and ReCiPe (version 1.1, hierarchist scenario, 2016) [164] impact assessment method were applied in order to quantify these impacts based on knowledge about the energy, inputs and outputs required for the production of one thermostatic valve housing via the two production systems. The results from this screening LCA are preliminary since the new production method for brass is still on a laboratory scale, and no actual production system is available to perform measurements on.

To be able to assess the impacts of the functional unit made using conventional material, data on the associated energy, inputs and outputs are required. Data for conventional brass production, including recycling, as well as for the electricity and lubricating oil needed in hot forging brass reclamation, was extracted from the Ecoinvent database version 3.5 [165] and selected to represent the global market including transport and transmission losses in the case of electricity production. The OpenLCA software version 1.8 [166] was used for calculations.

Even though no production system currently exists for chip forging, some basic data needs to be estimated for the two methods to perform the LCA. When producing the part using rod material, a piece of brass rod weighing 202 g is needed to produce one thermostatic valve housing where the finished part weighs 90 g. The removed material consists of 24 g flash, which cannot be recycled via the novel method. However, the remaining 88 g of scrap is removed as chips via metal cutting and is thus suitable for chip forging. Compared to using rod material, slightly more material, 250 g, is needed when using hot forging reclamation to ensure even material quality after forging. Because of this, the 88 g of material removed as chips can only replace 71 g of rod material when applying chip forging. The excess material is removed as flash after forging into a machining blank.

Most of the cutting fluid needs to be removed from the chips before reclamation. Because this oil separation is necessary in both manufacturing cases, the energy needed for this process will not be considered in the analysis. However, the 0.5 g oil per part that is required for the reclamation process to function properly will be included.

The chips need to be ground before compaction to ensure a suitable size distribution. The milling process requires energy, but relatively large batches of material can be milled simultaneously, resulting in an energy requirement of 0.02 kWh per part. Energy is also needed to compact the chips into green compacts, at 0.036 kWh per part.

The energy requirements for heating before compaction are difficult to quantify since it depends on whether the mould is heated or not. In other words, the heating energy required to produce the first compact is not the same as that required to produce subsequent compacts. In theory, the energy required to heat 250 g of chips is approximately 0.01 kWh based on the material's specific heat capacity, mass of the heated material and required temperature rise. In practice, considerably more energy is required due to heat loss and losses in energy conversion, so the electricity required for heating was estimated to 0.03 kWh per part. Based on the data gathered, the two production systems are shown in Figure 4.10. The 24 g of brass not available for chip forging in Figure 4.10 were 'cut off' and not included in the assessment [167].
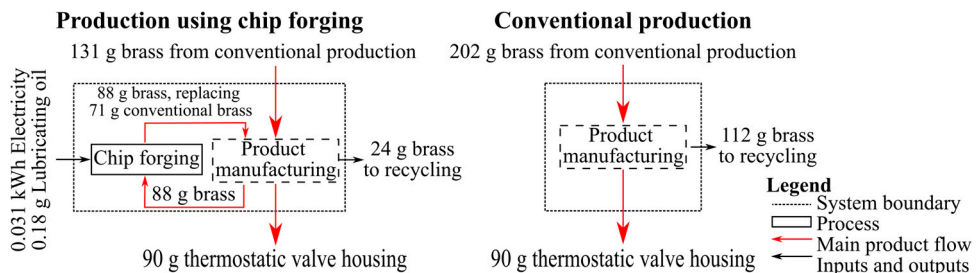
Figure 4.10. Manufacturing systems compared. Note that the product manufacturing process, marked with dashed lines, was not included in the analysis since the inputs and outputs of the process are assumed to be equal for both systems. [159]

The preliminary results for cumulative energy demand and climate change of the two compared systems for producing one thermostatic valve housing are presented in Figure 4.11. The impacts of the proposed production route using chip forging are lower than those of conventional brass production. Producing a thermostatic valve housing with the new production method has 29 % less cumulative energy demand and 30 % lower climate change impact compared to conventional production.
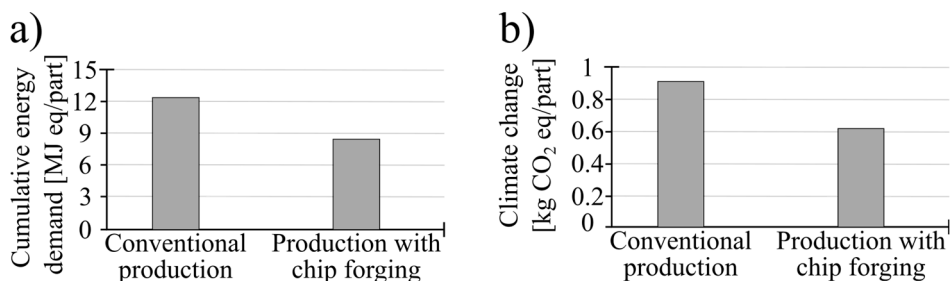
Figure 4.11. . Environmental impact expressed in a) cumulative energy demand [MJ eq.] and b) climate change [kg CO_2 eq.] for conventional production and production chip forging for a thermostatic valve housing [159].

4.5 Discussion and conclusions

The chapter describes how chip forging was developed from a feasibility study (paper IV), optimisation of a process parameter (paper V) and a screening LCA analysis for quantifying the environmental impact of using chip forging compared to conventional recycling (paper VI). In combination, papers IV to VI show that it is possible to re-use chips from metal cutting via compaction and hot forging instead of via traditional recycling where the material is melted and cast into new workpiece material. By using chip forging, the cumulative energy demand and climate change impact for production of a specific part are reduced by about 30 %. Some process parameters were investigated and optimised, for example, the type and amount of lubricating oil for compaction, but several more process parameters still need to be optimised, such as the compaction pressure and temperature as well as the forging temperature. The geometric shape of the forged component may also affect the outcome of chip forging since it is dependent on large plastic deformation and heat in the forging process to form uniform material. The comparison made in the LCA assumes that no significant degradation of the recycled material occurs over time, an assumption that needs to be experimentally verified.

The accuracy of any modelling will always be dependent on the quality of the input data, LCA is no exception to this rule. The results from the LCA presented are based on data from a reliable source, the Ecoinvent database, and any assessment of the accuracy of the data provided in that database is well outside the scope of this dissertation. Detailing the performance of a manufacturing system not yet existing at full scale is also not a trivial problem. Throughout the process, the LCA attempted to make a fair comparison between the two recycling cases based on independent data and scientific practices. Thus, the preliminary results are believed to be a valid and fair comparison between the systems.

Chip forging is still only on a laboratory scale, although with good results as outlined in this chapter. Given adequate time, upscaling and optimisation of the method, it is possible (or even likely) that the reclamation process could be improved. Thus, energy requirements might be reduced and other benefits, such as improved mechanical properties might become possible. Since there is, currently, no existing production system on which to perform measurements, there is some uncertainty associated with the numbers presented in this work; unforeseen problems may arise when scaling up the method for production and the production cost is not yet analysed.

Certainly, not all brass products made using hot forging will be suitable for chip forging. In the experiments conducted, none of the samples show full density or full mechanical strength, which indicates incomplete bonding between the chips in the material after chip forging. In some applications, the incomplete bonding will be problematic, and the consequences of incomplete bonding were not fully investigated. For instance, it is reasonable to suspect that fatigue resistance is lower in the inhomogeneous material since stress will not be evenly distributed. Corrosion resistance may also be affected, especially in applications with corrosive fluids that may penetrate porosities and shorten the service life of a component. More investigations are required to make definitive statements on these matters.

However, in some applications, these suspected flaws will not impact the function or quality of the manufactured component. Quality is, according to the author, relative and should be evaluated on a product's ability to fulfil the function it was designed for over the product life cycle. For instance, if a component is designed for exposure to a constant internal pressure of 10 bar, it is not necessarily an indicator of higher quality that the component does not fail when exposed to a constant pressure that is ten times higher than the pressure the part was designed for. It is, arguably, a sign of oversizing and can lead to wasted resources. Therefore, one should always strive for the 'right' quality for the application rather than for what may be perceived as 'high' quality. A product segment that may be especially suitable for introduction of chip forging is home furnishings (e.g., candlesticks and lighting armatures) where demands on the material's physical or chemical attributes are low from an engineering point of view.

While there is still developmental work to be done before chip forging can be fully implemented, it shows great potential in offering alternatives to traditional recycling and a way to a more circular material flow within the manufacturing industry.

5 Summary and conclusions

This chapter summarises the six appended papers and concludes the dissertation.

5.1 Summary of papers

5.1.1 Paper I: Machinability evaluation of low-lead brass alloys

Due to emerging regulations on the Pb content in brass alloys, the machinability of three Pb-free alloys was estimated and compared to Pb-containing brass (CuZn38Pb3). Several mechanical and thermal properties were measured, as well as results from machining, including cutting force measurements and burr height after machining.

The results show that none of the tested materials has as good or better machinability than Pb-containing brass. However, the machinability of CuZnSi3P is better than that of the other two investigated alloys, making it a viable choice for lead-free brass components.

5.1.2 Paper II: On the function of lead (Pb) in machining of brass alloys

As shown in paper I, brass with high Pb content shows extremely good machinability in case of turning. The reasons for the good machinability produced by alloying brass with Pb are not clearly understood. Examining and understanding the mechanism responsible may contribute to the development of more machinable brass alloys with low lead content.

The machining characteristics of two brass alloys, CuZn38Pb3 and CuZn42 were investigated and compared in a series of experiments. Several techniques were used to evaluate the effect of Pb on the machining process, including thermal imaging, high speed filming, scanning electron microscopy with x-ray energy dispersive spectroscopy (SEM XEDS), time-of-flight secondary mass ion spectroscopy (ToF SIMS), cutting force measurements and quick-stop testing.

The experiments revealed that the machinability enhancement provided by Pb does not originate from melting of Pb in the cutting zone, nor from Pb providing lubrication in the cutting zone. The reduction in cutting force is likely due to the short contact length between tool and chip and the easy separation of discrete chips from the workpiece, which is promoted by the presence of Pb globules in the material. When these globules are exposed to the high shear stress close to the shear plane, they start to deform, and as the stress increases, they form initiation points for crack formation. As a result, a thin, smeared, flakelike layer of lead can be seen when examining the shear plane using SEM.

5.1.3 Paper III: Influence of subsurface deformation induced by machining on stress corrosion cracking in lead-free brass

New stricter regulations on the lead content of brass for use in corrosive environments are driving the industry away from traditional leaded brass towards new Pb-free alloys. This has a knock-on effect on manufacturing, since Pb-free brass require higher cutting forces than traditional leaded brass. This increase in cutting forces may lead to increased subsurface deformation that can, in turn, lead to a decrease in corrosion resistance.

Two Pb-free brass alloys, CuZn38As and CuZn21Si3P, approved for use in drinking water applications, were machined using different tool geometries and feed rates. The resulting subsurface deformation was characterised using micro-hardness measurements and electron backscatter diffraction (EBSD). The material's resistance to stress corrosion cracking (SCC) was assessed by exposing the machined samples to a corrosive substance in accordance with SIS 117102.

Results show clear differences between the two tested materials' ability to withstand the corrosive environment without cracking, as well as a connection between subsurface deformation and SCC. In addition, tests showed that using a worn tool increases the subsurface deformation, which emphasises the need for process control when manufacturing products to be used in corrosive environments.

5.1.4 Paper IV: Hot forging operations of brass chips for material reclamation after machining operations

Chips are an inevitable by-product of all metal cutting operations. Production of small hollow components results in a high amount of chips per product. The paper investigates the feasibility of using compacted metal cutting chips as a base material for production of new machining blanks using hot forging.

By evaluating the relative density and microstructure of samples forged with different chip size distributions, it was found that narrower size distributions than

the distribution found directly after a turning operation did not have a significant effect on the end product.

Electron microscopy showed that partial diffusion bonding between the chips takes place during the forging operation and that heating and forging the chips into blanks does not change the material's chemical composition.

A small batch of blanks was machined into finished components and subjected to an acceptance test. Five out of eight components passed the acceptance test. The results indicate that it is possible to manufacture machining blanks from metal cutting chips, but further development is needed to improve the process.

5.1.5 Paper V: Determining process parameters for successful material reclamation of lead-free brass chips using hot forging operations: Lubrication

Since promising results were reported in Paper IV, the work of developing the recycling method continued. This paper focuses on one process parameter, namely the type and amount of lubricants used in the production of green compacts.

Unlike in paper IV, where chips from CuZn38Pb3 were used, machining chips from turning of CuZn21Si3P are used as base material. Mineral oil and rapeseed oil are used as lubricants, with and without additives of graphite nanoplatelets. Samples were produced and evaluated based on their relative density and torsional strength. Linear regression analysis and analysis of variance (ANOVA) were used to find the optimal type and amount of lubricants.

5.1.6 Paper VI: Screening environmental impact reduction enabled by brass reclamation through hot forging operations

Implementing the recycling method described in Paper IV and Paper V is likely to yield large environmental benefits. A screening cradle-to-gate life cycle assessment (LCA) is used to quantify these benefits.

A vital part of any LCA is defining the functional unit. In this case the functional unit chosen was a thermostatic valve housing. The methods known as cumulative energy demand and ReCiPe for climate change were used to quantify and compare the environmental impact of the functional unit when produced using conventional production methods and when produced using forging reclamation.

The preliminary results from the screening LCA show that using the hot forging recycling method would reduce both cumulative energy demand and climate change impact by about 30 % when producing the thermostatic valve housing compared to conventional recycling.

5.2 Conclusions

This dissertation shows that there are large differences in the material properties of the various brass alloys available on the market. These differences present challenges for the manufacturing industry, especially in relation to the machining of Pb-free alloys. The challenges can also be viewed as an opportunity to utilise the increased strength seen for one of the Pb-free alloys, CuZn21Si3P, to redesign components with more thin-walled sections without a loss of component strength. Such a redesign can reduce the amount of material needed to produce components compared to merely switching materials without redesign. The differences in material properties are also important to consider when machining these Pb-free alloys. In tensile testing, the mechanical properties for α- and α-β′ alloys are similar, but when using higher strain rates, as in the Charpy test, the leaded materials are shown to have significantly lower impact strength compared to Pb-free alloys.

One of the phases in CuZn21Si3P, κ′, is not found in reference databases. This is remarkable since databases of phases are extensive. The crystal structure and lattice parameters for κ′ have been be determined by using XRD and SAED.

The machinability of Pb-free brass is lower than that of alloys with high Pb content. This is well-known, but the mechanisms whereby Pb enhances machinability are still debated. Since no hard particles or phases are found in any of the investigated Pb-free materials, a previously published method of assessing a material's potential machinability was altered so as to better capture the potential machinability of brass alloys. The alteration consisted of exchanging abrasiveness for impact toughness. Large differences are seen between materials with different Pb content, which may be related to the formation of long, continuous chip formation in Pb-free brass.

The chip formation process in metal cutting is different between Pb-free alloys and brass with high Pb content. When machining brass with high Pb content, no continuous chips are formed irrespective of cutting speed. This indicates that the discontinuous chip formation process is not linked to cutting temperature or deformation speed in and around the shear plane. Discontinuous chip formation offers several advantages from a machinability point of view as the chips are easily removed from the machine during production, and cutting forces are reduced due to the short contact length with the tool. The short contact length means that friction interactions between tool and chip are negligible and that tool temperatures are lower since much of the heat generated in the cutting process will be accumulated in the chip, and there is less time for heat transfer between tool and chip. The low tool temperature in machining of brass with high Pb content is confirmed by thermal imaging. The long tool life seen when cutting brass with high lead content is likely also linked to the low tool temperature. The mechanism that provides the short chipping nature of brass with high Pb content is facilitation of crack formation, starting from deformed Pb globules when they reach the shear plane. Assumptions

about Pb melting in the secondary shear zone are disproven and arguments are presented about avoiding the term 'internal lubrication' to explain the enhanced machinability when using high Pb content in brass. Hence, the identified mechanisms responsible for the good machinability of high Pb content brass alloys form the answer to **RQ1**.

As an answer to **RQ2**, it can be also concluded that modifying the Pb-free brass alloys with additives which improve lubrication on the tool-chip interface (e.g. graphite additives) may be not as effective as modifications which induce better chip formation and chip breaking. Lead-free brass alloys with secondary phases which are harder or more brittle than the main α-phase enhance the inhomogeneity of the microstructure and support segmented chip formation process. It is the presence of β′-phase in CuZn42 and κ′-phase in CuZn21Si3P and their contribution to shear banding during the chip formation, which reduces the contact length on the rake face, reduces the cutting temperature and reduces the forces and cutting resistance.

Chip forging is proposed, developed and reported on in the dissertation as a way to increase the utilization of the workpiece material used for manufacturing brass components using a combination of hot forging and machining. By compacting chips from metal cutting into a semi-solid body that can be handled and heated before being placed in a forging press, it is possible to manufacture machining blanks that have mechanical properties similar to those of wrought brass. Chip forging is tested for brass with high Pb content (CuZn38Pb3) and Pb-free brass (CuZn21Si3P) with similar results. Further development of several process parameters is needed to fully realise the potential of the method. To quantify the environmental impact of the method, a screening cradle-to-gate LCA was conducted. This indicates that the method can reduce both cumulative energy demand and emissions that contribute to climate change by about 30 % compared to conventional production of a brass component. In this way, it was shown that **RQ3** can be achieved given further optimization of the chip forging process for maximizing material properties, and its upscaling for more exhaustive LCA analysis.

Finally, some recommendations to legislators and regulatory bodies need to be expressed. Discussions about reducing lead in certain applications, especially for components in contact with drinking water, have been going on for a long time and new regulations will soon be implemented across the European Union. When implementing these new regulations, attention should also be paid to goods produced outside the EU. Since lead-free brass has less favourable machining properties than products with high Pb content, as shown in chapter 3, domestic production will be at a severe disadvantage compared to imported products if imports do not have to adhere to the same rules and regulations. The reduction of Pb in brass is motivated by environmental and health-related issues that affect all brass products regardless of where they are produced. Therefore, imported goods must need to meet the same regulations as goods produced in the European Union.

The first reason for insisting on the same regulations is to legitimise the reduction of Pb in components made within the Union, motivated by health and environmental concerns. The second reason is related to fair competition in an open market. If domestic production is 'handicapped' by regulations, it should not be possible to import goods that cannot be manufactured domestically but compete on equal terms in the market. Obstacles to trade, such as tolls and import fees, can be used to balance the unequal production prerequisites, but the imported goods may still cause problems in the recycling process, which is the third reason to restrict import of components that do not follow the same regulations. Currently, brass is a highly circular material where a large share of the produced stock material is based on recycling. There is currently no efficient process for removing Pb from scrap, see section 1.3. Without a method to remove Pb from brass scrap, the only option to recycle brass scrap with unknown amounts of lead is dilution with virgin material to obtain Pb-free scrap. If brass components with high Pb content continue to be imported because of the increased cost of domestic production, the material stream to recycling will continue to contain higher amounts of Pb, making even more dilution necessary, which decreases the environmental and economic gains of recycling.

5.3 Future work

Brass, and especially lead-free brass, has been the subject of far less research than other commonly used engineering materials such as steel and aluminium, or even less commonly used materials such as titanium alloys. However, when the conditions for production in brass are changing, as is currently the case given the requirement to reduce Pb content, academia needs to provide industry with the support it needs to be able to make the transition as smoothly as possible. Because academia cannot provide detailed answers to specific questions related to the production of individual components, academic work should be directed towards providing answers and explanations for widely recognised issues and phenomena.

Although the European Union has decided to regulate Pb content, the regulations have not yet been implemented by the member states. Thus, the development of restrictions on Pb content needs to be closely followed in the near future. Currently, there is no widely accepted definition for what is to be considered 'Pb-free brass', but the industry and some certification bodies such as Sunda Hus are leaning towards considering brass with < 0.1 wt.% Pb as Pb-free. From a technological point of view, this is a rather generous definition of being free from a substance. It would be beneficial to develop a widely accepted definition, preferably worldwide, of what is to be considered 'Pb-free brass'.

This dissertation has relied on commercially available alloys. The composition of these alloys can vary within specified ranges, and it would be of interest to see whether there are some machinability maxima within the specified alloy limits. The work could then be expanded by introducing other alloying elements outside the alloy specifications. Development of new alloys is a complex task since the material produced must not only be machinable but must also meet the requirements in the use-phase of the produced component.

This investigation of machinability in this dissertation is restricted to turning, which is obviously not the only method used to produce parts. To gain a more comprehensive perspective on the machining in Pb-free brass, the work needs to be expanded to other machining methods, primarily milling and drilling. Some general guidelines about the machining of Pb-free brass need to be developed as regards machining data and tool geometries. This development should be done in close collaboration with industrial partners so as to understand the needs and differences in production prerequisites.

Some topics are left open for further investigation in this dissertation. For example, it is not clear whether the presence of the κ'-phase in CuZn21Si3P is due to the formation of a stable phase that should be found in the ternary phase diagram or whether it is a basically meta-stable phase that is stabilised by minor alloying elements. To determine this, further investigations are needed.

As previously discussed, chip forging is still in the initial stages of development, but the promising results so far should motivate further development. It should be possible to improve the quality of the chip forged material by further optimization. Process parameters that could be investigated and optimised include pressure and temperature in the compaction stage. Suitable and unsuitable blank geometries in the forging stage could also be investigated. In addition, the possibility of replacing the green compacts from the compaction stage by using extrusion should be investigated. If extrusion is feasible, continuous compacted rods could be produced, which would arguably be beneficial in production since they could be cut to length instead of producing green compacts with differing amounts of material.

6 References

[1] Copper: An Ancient Metal (2021) Darthmouth Toxic Metals Superfund Research program, Retrieved from https://sites.dartmouth.edu/toxmetal/more-metals/copper-an-ancient-metal/. Accessed 2021-12-21.

[2] Craddock, P. T. (1978). The composition of the copper alloys used by the Greek, Etruscan and Roman civilizations: 3. The origins and early use of brass. *Journal of Archaeological Science*, 5(1), 1-16.

[3] Macalister, R. (1912). The Excavaton of Gezer.

[4] Craddock, P. T. (1976). The composition of the copper alloys used by the Greek, Etruscan and Roman civilizations 1. The Greeks before the archaic period. *Journal of Archaeological Science*, 3(2), 93-113. doi: https://doi.org/10.1016/0305-4403(76)90079-0.

[5] Rumford, B. (1798). An Inquiry concerning the Source of the Heat Which is Excited by Friction. *Philosophical Transactions of the Royal Society of London*, 88, 80-102. doi: https://doi.org/10.2307/106970.

[6] Callister Jr, W. D., & Rethwisch, D. G. (2008). Fundamentals of materials science and engineering: an integrated approach. John Wiley & Sons.

[7] Obitz, C., Johansson, J., Hagström, J., Windmark, C., Ståhl, J.-E., Rod, O., et al. (2022) 'Förbättrade blyfria mässingsprodukter genom optimering längs värdekedjan (OPTIBRASS). Slutrapport' *Jernkontorets forskning*. Jernkontoret B 780.

[8] Thornton, I., Rautiu, R., & Brush, S. M. (2001). Lead the facts. London, UK: IC Consultants Ltd.

[9] Maher, B. A., Moore, C., & Matzka, J. (2008). Spatial variation in vehicle-derived metal pollution identified by magnetic and elemental analysis of roadside tree leaves. *Atmospheric Environment*, 42(2), 364-373. doi: https://doi.org/10.1016/j.atmosenv.2007.09.013.

[10] Levin, R., Zilli Vieira, C. L., Rosenbaum, M. H., Bischoff, K., Mordarski, D. C., & Brown, M. J. (2021). The urban lead (Pb) burden in humans, animals and the natural environment. *Environ Res*, 193, 110377. doi: https://doi.org/10.1016/j.envres.2020.110377.

[11] Radcliffe, D. (1990, 1990-08-04). Millie Gets the Lead Out. *Washington Post*. Retrieved from https://www.washingtonpost.com/archive/lifestyle/1990/08/04/millie-gets-the-lead-out/98307e73-6f7d-4e34-ad1c-9c1d0461d8d8/

[12] Vaajamo, T., Johto, H., & Taskinen, P. (2013). Solubility study of the copper-lead system. *International Journal of Materials Research*, 104(4), 372-376. doi: https://doi.org/10.3139/146.110876.

[13] Samandi, M., & Wise, M. (1989) 'Machinability of Copper Based Alloys' *J INCRA Rep*. p. 110.

[14] Rosner, D. (2016). A Lead Poisoning Crisis Enters Its Second Century. *Health Aff (Millwood)*, 35(5), 756-9. doi: https://doi.org/10.1377/hlthaff.2016.0362.

[15] Shelson, J. (2016). Lead in the Water-The Flint Water Crisis. *Def. Counsel J.*, 83, 520-525.

[16] International lead and zinc study group (2019). The world lead factbook 2019. Portugal: Liasbon.

[17] European Union (2020). DIRECTIVE (EU) 2020/2184 OF THE EUROPEAN PARLIAMENT AND OF THE COUNCIL of 16 December 2020 on the quality of water intended for human consumption. *Official Journal of the European Union*.

[18] 4 MS Common Approach (2020) 'ACCEPTANCE OF METALLIC MATERIALS USED FOR PRODUCTS IN CONTACT WITH DRINKING WATER ' *Procedure for the acceptance of metallic materials for PDW*.

[19] Estelle, A. A. (2016). Drinking water lead regulations: impact on the brass value chain. *Materials Science and Technology*, 32(17), 1763-1770. doi: https://doi.org/10.1080/02670836.2016.1220906.

[20] Wolfenden, A., & Robinson, W. H. (1977). Mechanical Damping in Leaded and in Lead-Free Alpha-Brass. *Acta Metallurgica*, 25(7), 823-826. doi: https://doi.org/10.1016/0001-6160(77)90099-2.

[21] Kennedy, F. E., & Voss, D. A. (1979). REEXAMINATION OF THE WEAR OF LEADED BRASS ON HARDENED STEEL (Conference Paper). *Wear of Materials*, 89-96. https://www.scopus.com/inward/record.uri?eid=2-s2.0-0018675206&partnerID=40&md5=f2bb5fb1b1c5afae40b864fbe6be7bbf.

[22] Glardon, R., & Finnie, I. (1983). A Study of the Friction and Wear of Cartridge and Free-Cutting Brass. *Journal of Engineering Materials and Technology-Transactions of the Asme*, 105(1), 31-35. doi: https://doi.org/10.1115/1.3225615.

[23] Wolfenden, A., & Wright, P. K. (1979). Role of lead in free-machining brass. *Metals Technology*, 6(1), 297-302. doi: https://doi.org/10.1179/030716979803276697.

[24] Gane, N. (1980). The effect of lead on the friction and machining of brass. *Philosophical Magazine A*, 43(3), 545-566. doi: https://doi.org/10.1080/01418618108240394.

[25] Doyle, E. D. (1974). MECHANISMS OF PLASTIC INSTABILITY IN THE MACHINING OF METALS. https://www.scopus.com/inward/record.uri?eid=2-s2.0-0016363318&partnerID=40&md5=8d4c2ebcc7755e62c03ab8cc2d1bd86e

[26] Sullivan, K. F., Wright, P. K., & Smith, P. D. (1978). Metallurgical Appraisal of Instabilities Arising in Machining. *Metals Technology*, 5(Jun), 181-189. doi: https://doi.org/10.1179/mt.1978.5.1.181 .

[27] Stoddart, C. T. H., Lea, C., Dench, W. A., Green, P., & Pettit, H. R. (1979). Relationship between lead content of Cu–40Zn, machinability, and svvarf surface composition determined by Auger electron spectroscopy. *Metals Technology*, 6(1), 176-184. doi: https://doi.org/10.1179/030716979803276435.

[28] Williams, J. E., Smart, E. F., & Milner, D. R. (1970). Metallurgy of Machining 2. Cutting of Single-Phase, 2-Phase and Some Free Machining Alloys (Article). *Metallurgia*, 81(484), 51-59.

[29] Padmavardhani, D., & Prasad, Y. (1991). Characterization of hot deformation behavior of brasses using processing maps: Part I. α Brass. *Metallurgical Transactions A*, 22(12), 2985-2992.

[30] Padmavardhani, D., & Prasad, Y. (1991). Characterization of hot deformation behavior of brasses using processing maps: Part II. β Brass and α-β brass. *Metallurgical Transactions A*, 22(12), 2993-3001.

[31] La Fontaine, A., & Keast, V. J. (2006). Compositional distributions in classical and lead-free brasses. *Materials Characterization*, 57(4-5), 424-429. doi: https://doi.org/10.1016/j.matchar.2006.02.005.

[32] Vilarinho, C., Davim, J. P., Soares, D., Castro, F., & Barbosa, J. (2005). Influence of the chemical composition on the machinability of brasses. *Journal of Materials Processing Technology*, 170(1-2), 441-447. doi: https://doi.org/10.1016/j.jmatprotec.2005.05.035.

[33] Nobel, C., Klocke, F., Lung, D., & Wolf, S. (2014). Machinability Enhancement of Lead-free Brass Alloys. *Procedia CIRP*, 14, 95-100. doi: https://doi.org/10.1016/j.procir.2014.03.018.

[34] Schultheiss, F., Johansson, D., Bushlya, V., Zhou, J., Nilsson, K., & Ståhl, J.-E. (2017). Comparative study on the machinability of lead-free brass. *Journal of Cleaner Production*, 149, 366-377. doi: https://doi.org/10.1016/j.jclepro.2017.02.098

[35] Johansson, J., Persson, H., Ståhl, J. E., Zhou, J. M., Bushlya, V., & Schultheiss, F. (2019). Machinability Evaluation of Low-Lead Brass Alloys. *Procedia Manufacturing*, 38, 1723-1730. doi: https://doi.org/10.1016/j.promfg.2020.01.102.

[36] Toulfatzis, A., Pantazopoulos, G., David, C., Sagris, D., & Paipetis, A. (2018). Machinability of Eco-Friendly Lead-Free Brass Alloys: Cutting-Force and Surface-Roughness Optimization. *Metals*, 8(4), 250. doi: https://doi.org/10.3390/met8040250

[37] Laakso, S. V. A., Hokka, M., Niemi, E., & Kuokkala, V.-T. (2013). Investigation of the effect of different cutting parameters on chip formation of low-lead brass with experiments and simulations. *Proceedings of the Institution of Mechanical Engineers, Part B: Journal of Engineering Manufacture*, 227(11), 1620-1634. doi: https://doi.org/10.1177/0954405413492732.

[38] Reddy, V. V., Tam, P. L., Krishna, A. V., & Rosén, B. G. 1183 (2019) 'Characterization of subsurface deformation of turned brasses: lead brass (CuZn39Pb3) and lead free brass (CuZn21Si3P)' *Journal of Physics: Conference Series*. IOP Publishing. doi: https://doi.org/10.1088/1742-6596/1183/1/012006.

[39] Laws, K. J., Crosby, C., Sridhar, A., Conway, P., Koloadin, L. S., Zhao, M., et al. (2015). High entropy brasses and bronzes – Microstructure, phase evolution and properties. *Journal of Alloys and Compounds*, 650, 949-961. doi: https://doi.org/10.1016/j.jallcom.2015.07.285.

[40] Imai, H., Kosaka, Y., Kojima, A., Li, S., Kondoh, K., Umeda, J., et al. (2010). Characteristics and machinability of lead-free P/M Cu60–Zn40 brass alloys dispersed with graphite. *Powder Technology*, 198(3), 417-421. doi: https://doi.org/10.1016/j.powtec.2009.12.010.

[41] Li, S. F., Kondoh, K., Imai, H., & Atsumi, H. (2011). Fabrication and properties of lead-free machinable brass with Ti additive by powder metallurgy. *Powder Technology*, 205(1-3), 242-249. doi: https://doi.org/10.1016/j.powtec.2010.09.020.

[42] Wang, J., Liu, P., Liu, X., Chen, X., Li, W., Ma, F., et al. (2018). Effect of Si and P content on microstructure and properties of lead-free brass (Article). *Gongneng Cailiao/Journal of Functional Materials*, 49(11), 11194-11199. https://www.scopus.com/inward/record.uri?eid=2-s2.0-85063326283&doi=10.3969%2fj.issn.1001-9731.2018.11.032&partnerID=40&md5=edec1dd25f610673707d30938b1e9829.

[43] Kuyucak, S., & Sahoo, M. (1996). A review of the machinability of copper-base alloys. *Canadian Metallurgical Quarterly*, 35(1), 1-15. doi: https://doi.org/10.1179/cmq.1996.35.1.1.

[44] Stavroulakis, P., Toulfatzis, A. I., Pantazopoulos, G. A., & Paipetis, A. S. (2022). Machinable Leaded and Eco-Friendly Brass Alloys for High Performance Manufacturing Processes: A Critical Review. *Metals*, 12(2), 246. doi: https://doi.org/10.3390/met12020246.

[45] Nakano, A., Rochman, N. T., & Sueyoshi, H. (2005). Removal of lead from copper alloy scraps by compound-separation method. *Materials Transactions*, 46(12), 2719-2724. doi: https://doi.org/10.2320/matertrans.46.2719.

[46] Sueyoshi, H., Yamada, K., Miyazaki, M., Okada, T., Ashie, N., & Kousaka, Y. (2018). Mechanism of Pb Removal from Brass Scrap by Compound Separation Using Ca and NaF. *International Journal of Nonferrous Metallurgy*, 07(01), 1-7. doi: https://doi.org/10.4236/ijnm.2018.71001.

[47] Hilgendorf, S., Binz, F., Welter, J. M., & Friedrich, B. (2016). Lead removal from brass scrap by fluorine-free compound separation. *Materials Science and Technology*, 32(17), 1782-1788. doi: https://doi.org/10.1080/02670836.2016.1223574 .

[48] Huang, X. S., Zhao, H. L., Wang, C. Y., & Zhang, X. F. (2020). One-step separation of hazardous element lead in brass alloy by physical external field. *Journal of Cleaner Production*, 276, 123358. doi: https://doi.org/10.1016/j.jclepro.2020.123358.

[49] Grohbauer, A., & Wieland-Werke AG. (2012) Verfahren zur Abtrennung von Blei aus dem Messing-Recycling-Kreislauf.

[50] Schultheiss, F., Sjöstrand, S., Rasmusson, M., Windmark, C., & Ståhl, J.-E. (2016) 'Comparative Study on the Machinability and Manufacturing Cost in Low-Lead Brass' *26th International Conference on Flexible Automation and Intelligent Manufacturing*. pp. 496-503.

[51] Andersson, Ö. (2012). Experiment! - Planning, Implementing and Interpreting. West Sussex, United Kingdom: John Wiley & Sons.

[52] Murakami, Y. (1972). Lattice Softening, Phase Stability and Elastic Anomaly of the β-Au-Cu-Zn Alloys. *Journal of the Physical Society of Japan*, 33(5), 1350-1360. doi: https://doi.org/10.1143/jpsj.33.1350.

[53] Shimizu, S., Murakami, Y., & Kachi, S. (1976). Lattice Softening and Martensitic Transformation in Cu–Ni–Zn β Phase Alloys. *Journal of the Physical Society of Japan*, 41(1), 79-84. doi: https://doi.org/10.1143/jpsj.41.79.

[54] 'Cu-Zn Binary Phase Diagram 0-100 at.% Zn: Datasheet from "PAULING FILE Multinaries Edition – 2012" in SpringerMaterials' (2021). Springer-Verlag Berlin Heidelberg & Material Phases Data System (MPDS), Switzerland & National Institute for Materials Science (NIMS), Japan. Available at: https://materials.springer.com/isp/phase-diagram/docs/c_0906431 (Accessed: 2021-12-28).

[55] Straumanis, M. E. (1949). The Precision Determination of Lattice Constants by the Powder and Rotating Crystal Methods and Applications. *Journal of Applied Physics*, 20(8), 726-734. doi: https://doi.org/10.1063/1.1698520.

[56] Wang, J., Xu, H., Shang, S., Zhang, L., Du, Y., Zhang, W., et al. (2011). Experimental investigation and thermodynamic modeling of the Cu–Si–Zn system with the refined description for the Cu–Zn system. *Calphad*, 35(2), 191-203. doi: https://doi.org/10.1016/j.calphad.2011.02.001.

[57] Jacobsson, D., Däcker, C.-Å., Sundberg, R., & Rod, O. (2010). A general guide for failure analysis of brass. Stockholm, Sweden: Swerea KIMAB.

[58] Sundberg, R., Holm, R., Hertzman, S., Hutchinson, B., & Lindh-Ulmgren, E. (2003). Dezincification (DA) and intergranular corrosion (IGA) of brass - influence of composition and heat treatment. *Metall*, 57(11), 721-731.

[59] Humphreys, F. J. (2001). Grain and subgrain characterisation by electron backscatter diffraction. *Journal of Materials Science*, 36(16), 3833-3854. doi: https://doi.org/10.1023/a:1017973432592.

[60] Predel, B. 'Ac-Ag ... Au-Zr · Introduction: Datasheet from Landolt-Börnstein - Group IV Physical Chemistry · Volume 12A: "Ac-Ag ... Au-Zr" in SpringerMaterials'. Springer-Verlag Berlin Heidelberg. Available at: https://materials.springer.com/lb/docs/sm_lbs_978-3-540-33962-5_2 .

[61] Lewis, R., Christoforou, P., Wang, W. J., Beagles, A., Burstow, M., & Lewis, S. R. (2019). Investigation of the influence of rail hardness on the wear of rail and wheel materials under dry conditions (ICRI wear mapping project). *Wear*, 430, 383-392. doi: https://doi.org/10.1016/j.wear.2019.05.030.

[62] Jan-Eric, S., & Seco Tools AB. (2012). Metal cutting theories and models. Division of Production and Materials Engineering.

[63] Songmene, V., Zaghbani, I., & Kientzy, G. (2018). Machining and Machinability of Tool Steels: Effects of Lubrication and Machining Conditions on Tool Wear and Tool Life Data. *8th Cirp Conference on High Performance Cutting (Hpc 2018)*, 77, 505-508. doi: https://doi.org/10.1016/j.procir.2018.08.252.

[64] Broitman, E. (2017). Indentation Hardness Measurements at Macro-, Micro-, and Nanoscale: A Critical Overview. *Tribology Letters*, 65(1). doi: https://doi.org/10.1007/s11249-016-0805-5.

[65] Oliver, W. C., & Pharr, G. M. (1992). An Improved Technique for Determining Hardness and Elastic-Modulus Using Load and Displacement Sensing Indentation Experiments. *Journal of Materials Research*, 7(6), 1564-1583. doi: https://doi.org/10.1557/Jmr.1992.1564.

[66] Tóth, L., Rossmanith, H. P., & Siewert, T. A. (2002). Historical background and development of the Charpy test. *European Structural Integrity Society*, 30, 3-19. doi: https://doi.org/10.1016/S1566-1369(02)80002-4.

[67] Lucon, E. (2016). Experimental Assessment of the Equivalent Strain Rate for an Instrumented Charpy Test. *Journal of Research of the National Institute of Standards and Technology*, 121, 165-179. doi: https://doi.org/10.6028/jres.121.007.

[68] Nobel, C., Hofmann, U., Klocke, F., & Veselovac, D. (2016). Experimental investigation of chip formation, flow, and breakage in free orthogonal cutting of copper-zinc alloys. *International Journal of Advanced Manufacturing Technology*, 84(5-8), 1127-1140. doi: https://doi.org/10.1007/s00170-015-7749-z.

[69] Nobel, C., Hofmann, U., Klocke, F., Veselovac, D., & Puls, H. (2015). Application of a new, severe-condition friction test method to understand the machining characteristics of Cu–Zn alloys using coated cutting tools. *Wear*, 344, 58-68.

[70] Borggren, U., & Selleby, M. (2003). A thermodynamic database for special brass. *Journal of Phase Equilibria*, 24(2), 110-121. doi: https://doi.org/10.1361/105497103770330721.

[71] 'Cu7Si (Cu0.875Si0.125 ht) Crystal Structure: Datasheet from "PAULING FILE Multinaries Edition – 2012" in SpringerMaterials'. Springer-Verlag Berlin Heidelberg & Material Phases Data System (MPDS), Switzerland & National Institute for Materials Science (NIMS), Japan. Available at: https://materials.springer.com/isp/crystallographic/docs/sd_1210743.

[72] Weitzer, F., Remschnig, K., Schuster, J. C., & Rogl, P. (1990). Phase equilibria and structural chemistry in the ternary systems M–Si–N and M–B–N (M = Al, Cu, Zn, Ag, Cd, In, Sn, Sb, Au, Tl, Pb, Bi). *Journal of Materials Research*, 5(10), 2152-2159. doi: https://doi.org/10.1557/jmr.1990.2152.

[73] 'Cu-Si-Zn Vertical Section of Ternary Phase Diagram: Datasheet from "PAULING FILE Multinaries Edition – 2012" in SpringerMaterials'. Springer-Verlag Berlin Heidelberg & Material Phases Data System (MPDS), Switzerland & National Institute for Materials Science (NIMS), Japan. Available at: https://materials.springer.com/isp/phase-diagram/docs/c_0927245.

[74] Mima, G., & Hasegawa, M. (1957). Diagram of copper-silicon-zinc alloys. II. *Technology Reports of the Osaka University*, 7, 385-97.

[75] Olesinski, R. W., & Abbaschian, G. J. (1986). The Cu−Si (Copper-Silicon) system. *Bulletin of Alloy Phase Diagrams*, 7(2), 170-178. doi: https://doi.org/10.1007/bf02881559.

[76] Tam, P. L., Schultheiss, F., Stahl, J. E., & Nyborg, L. (2016). Residual stress analysis of machined lead-free and lead-containing brasses. *Materials Science and Technology*, 32(17), 1789-1793. doi: https://doi.org/10.1080/02670836.2016.1223266.

[77] Giannuzzi, L. A., & Stevie, F. A. (1999). A review of focused ion beam milling techniques for TEM specimen preparation. *Micron*, 30(3), 197-204. doi: https://doi.org/10.1016/S0968-4328(99)00005-0.

[78] Vieregge, G. (1959). Zerspanung der Eisenwerkstoffe. Verlag Stahleisen.

[79] Shaw, M. C., & Cookson, J. O. (2005). Metal cutting principles. Oxford, New York, USA: Oxford University press New York.

[80] Sandvik Coromant AB. (1994). Modern skärande bearbetning - en praktisk handbok (in Swedish). Sandviken, Sweden: Sandvik Coromant - Tekniska Redaktionen, CMSK.

[81] Mills, B., & Redford, A. H. (1983). The Concept of Machinability. Essex, England: Applied Science publishers LTD.

[82] Venkata, R. (2005). Machinability evaluation of work materials using a combined multiple attribute decision-making method. *The International Journal of Advanced Manufacturing Technology*, 28(3-4), 221-227. doi: https://doi.org/10.1007/s00170-004-2348-4.

[83] Henkin, A., & Datsko, J. (1963). The Influence of Physical Properties on Machinability (Article). *Journal of Engineering for Industry*, 85(4), 321-327. doi: https://doi.org/10.1115/1.3669880.

[84] Thiele, E. W. J., Kundig, K. J. A., Murphy, D. W., Soloway, G., & Duffin, B. (1990). Comparative Machinability of Brasses, Steels and Aluminum Alloys: CDA's Universal Machinability Index. *SAE Transactions*, 99, 362-371. doi: https://doi.org/10.2307/44553710.

[85] ASM International. (1995). ASM Handbook Vol. 16: Machining. Materials Park, OH, USA: ASM International.

[86] Andersson, M., & Ståhl, J.-E. (2007) 'Polar machinability diagrams-A model to predict the machinability of a work material' *Swedish Production Symposium*.

[87] Xu, L., Schultheiss, F., Andersson, M., & Ståhl, J.-E. (2013). General conception of polar diagrams for the evaluation of the potential machinability of workpiece materials. *International Journal of Machining and Machinability of Materials*, 14(1). doi: https://doi.org/10.1504/ijmmm.2013.055119.

[88] Olovsjö, S., Hammersberg, P., Avdovic, P., Ståhl, J.-E., & Nyborg, L. (2012). Methodology for evaluating effects of material characteristics on machinability— theory and statistics-based modelling applied on Alloy 718. *The International Journal of Advanced Manufacturing Technology*, 59(1-4), 55-66.

[89] Chen, L. (2015). Nanoindentation characterization of high chromium white cast iron for assessment of machining performance. Lund: Lund University.

[90] Woxén, R. (1932). A Theory and an equation for the life of lathe tools. *Ingeniörsvetenskapsakademins handlingar*, 119.

[91] Johansson, I. (1967) Metod för beräkning av skärkraft, moment och effekter vid fräsning. Chalmers tekniska högskola

[92] Kienzle, O. (1952). Die bestimmung von kräften und Leistungen an spanenden Werkzeugen und Werkzeugmaschinen (in German). *J VDI-Z*, 94(11), 299-305.

[93] Taylor, F. W. (1906). On the art of cutting metals. THE AMERICAN SOCIETY OF MECHANICAL ENGINEERS.

[94] Klocke, F., Nobel, C., & Veselovac, D. (2015). Influence of Tool Coating, Tool Material, and Cutting Speed on the Machinability of Low-Leaded Brass Alloys in Turning. *Materials and Manufacturing Processes*, 31(14), 1895-1903. doi: https://doi.org/10.1080/10426914.2015.1127944.

[95] Augspurger, T., Bergs, T., Döbbeler, B., & Lima, A. (2019). Methodology for the Measurement of the Heat Partitioning by Thermal Imaging in the Orthogonal Cutting Process. *Journal of Heat Transfer*, 141(7). doi: https://doi.org/10.1115/1.4043170.

[96] Davies, M. A., Ueda, T., M'Saoubi, R., Mullany, B., & Cooke, A. L. (2007). On The Measurement of Temperature in Material Removal Processes. *CIRP Annals*, 56(2), 581-604. doi: https://doi.org/10.1016/j.cirp.2007.10.009.

[97] Rudnev, V., Loveless, D., Cook, R., & Black, M. (2003). Handbook of Induction Heating. New York, USA: Marcel Dekker Inc.

[98] Lanc, Z., Zeljković, M., Živković, A., Štrbac, B., & Hadžistević, M. (2018). Determination of Emissivity of Brass Alloy using Infrared Thermographic Technique. *Original scientific paper Izvirni znanstveni članki*, 65(3), 115-122.

[99] Bjerke, A., Hrechuk, A., Lenrick, F., M'Saoubi, R., Larsson, H., Markström, A., et al. (2021). Onset of the degradation of CVD α-Al2O3 coating during turning of Ca-treated steels. *Wear*, 477, 203785. doi: https://doi.org/10.1016/j.wear.2021.203785.

[100] Lindvall, R., Lenrick, F., Persson, H., M'Saoubi, R., Stahl, J. E., & Bushlya, V. (2020). Performance and wear mechanisms of PCD and pcBN cutting tools during machining titanium alloy Ti6Al4V. *Wear*, 454, 203329. doi: https://doi.org/10.1016/j.wear.2020.203329.

[101] Sagapuram, D., Udupa, A., Viswanathan, K., Mann, J. B., M'Saoubi, R., Sugihara, T., et al. (2020). On the Cutting of Metals: A Mechanics Viewpoint. *Journal of Manufacturing Science and Engineering*, 142(11). doi: https://doi.org/10.1115/1.4047869.

[102] Olsson, M. (2021) Machinability of Single-phase Materials: Surface integrity and tool wear analysis. Lund University

[103] Giannuzzi, L. A., & Michael, J. R. (2013). Comparison of channeling contrast between ion and electron images. *Microscopy and Microanalysis*, 19(2), 344-349. doi: https://doi.org/10.1017/S1431927612014286.

[104] Childs, T. H. C. (2006). Friction modelling in metal cutting. *Wear*, 260(3), 310-318. doi: https://doi.org/10.1016/j.wear.2005.01.052.

[105] Timothy, S. P. (1987). The Structure of Adiabatic Shear Bands in Metals - a Critical-Review. *Acta Metallurgica*, 35(2), 301-306. doi: https://doi.org/10.1016/0001-6160(87)90238-0.

[106] Childs, T. H. C., Arrazola, P.-J., Azpitarte, L., Garay, A., Soriano, D., S-de-Buruaga, M., et al. (2022). Physical modelling with experimental validation of high ductility metal cutting chip formation illustrated by copper machining. *International Journal of Machine Tools and Manufacture*, 173, 103847. doi: https://doi.org/10.1016/j.ijmachtools.2021.103847.

[107] Trent, E. M., & Wright, P. K. (2000). Metal cutting. Butterworth-Heinemann.

[108] Östholm, S. (1990) Simulering och identifiering av skäreggars mekaniska belastningsbild (in Swedish). Doctoral, Lund University

[109] Ståhl, J.-E., & Östholm, S. 84-02 (1984) 'Studie av skäreggens belastningsbild vid diskontinuerlig spånbildning (in Swedish)' *Institutionen för mekanisk teknologi och verktygsmaskiners rapportserie*. 1984-10-10. Lund, Sweden: Institutionen för mekanisk teknologi, Tekniska högskolan i Lund.

[110] Amaral, L., Quinta, R., Silva, T. E., Soares, R. M., Castellanos, S. D., & de Jesus, A. M. P. (2018). Effect of lead on the machinability of brass alloys using polycrystalline diamond cutting tools. *Journal of Strain Analysis for Engineering Design*, 53(8), 602-615. doi: https://doi.org/10.1177/0309324718796384.

[111] Bushlya, V., Johansson, D., Lenrick, F., Ståhl, J.-E., & Schultheiss, F. (2017). Wear mechanisms of uncoated and coated cemented carbide tools in machining lead-free silicon brass. *Wear*, 376-377, 143-151. doi: https://doi.org/10.1016/j.wear.2017.01.039.

[113] Trent, E. M. (1988). Metal cutting and the tribology of seizure: III temperatures in metal cutting. *Wear*, 128(1), 65-81. doi: https://doi.org/10.1016/0043-1648(88)90253-0.

[114] Johansson, J., Alm, P., M'Saoubi, R., Malmberg, P., Ståhl, J.-E., & Bushlya, V. (2022). On the function of lead (Pb) in machining brass alloys. *The International Journal of Advanced Manufacturing Technology*. doi: http://doi.org/10.1007/s00170-022-09205-0.

[115] Ståhl, J.-E. (1986) Skäreggars spontanhaverier. Doctoral, Lund University

[116] Schultheiss, F., Fallqvist, M., M'Saoubi, R., Olsson, M., & Ståhl, J. E. (2013). Influence of the tool surface micro topography on the tribological characteristics in metal cutting—Part II Theoretical calculations of contact conditions. *Wear*, 298-299, 23-31. doi: https://doi.org/10.1016/j.wear.2012.11.067.

[117] Doyle, E. D., Horne, J. G., & Tabor, D. (1979). Frictional interactions between chip and rake face in continuous chip formation. *Proceedings of the Royal Society of London. A. Mathematical and Physical Sciences*, 366(1725), 173-183. doi: https://doi.org/10.1098/rspa.1979.0046.

[118] Chandrasekaran, H., Granfors, M., & M'Saoubi, R. (2006). Tribological aspects of tool–chip and tool–work contact in machining and the application of laser spectrometry. *Wear*, 260(3), 319-325. doi: https://doi.org/10.1016/j.wear.2005.04.023.

[119] Field, M., & Kahles, J. F. (1971). Review of surface integrity of machined components. *Annals of the CIRP*, 20(2), 153-163.

[120] Field, M., Kahles, J. F., & Cammet, J. T. (1972). A review of measuring methods for surface integrity. *Annals of the CIRP*, 21, 219-238.

[121] Tönshoff, H. K., Arendt, C., & Amor, R. B. (2000). Cutting of Hardened Steel. *CIRP Annals*, 49(2), 547-566. doi: https://doi.org/10.1016/s0007-8506(07)63455-6.

[122] Brandl, E., Malke, R., Beck, T., Wanner, A., & Hack, T. (2009). Stress corrosion cracking and selective corrosion of copper-zinc alloys for the drinking water installation. *Materials and Corrosion*, 60(4), 251-258. doi: https://doi.org/10.1002/maco.200805079.

[123] Bardal, E. (2004). Corrosion and Protection. London: Springer-Verlag.

[124] Sperry, E. S. (1906). The season-cracking of brass and bronze tubing. *Brass World*, 2(2), 39-44.

[125] Mattsson, E. (1961). Stress corrosion in brass considered against the background of potential/pH diagrams. *Electrochimica Acta*, 3(4), 279-291.
doi: https://dx.doi.org/10.1016/0013-4686(61)85004-4.

[126] Jones, R. H. (2017). Evaluation of Stress-Corrosion Cracking. In R. H. Jones (Ed.), *Stress-Corrosion Cracking* (pp. 367-417). ASM International. doi: https://doi.org/10.31399/asm.tb.sccmpe2.t55090367.

[127] Liao, Z. R., la Monaca, A., Murray, J., Speidel, A., Ushmaev, D., Clare, A., et al. (2021). Surface integrity in metal machining - Part I: Fundamentals of surface characteristics and formation mechanisms. *International Journal of Machine Tools & Manufacture*, 162, 103687. doi: https://doi.org/10.1016/j.ijmachtools.2020.103687.

[128] la Monaca, A., Murray, J. W., Liao, Z., Speidel, A., Robles-Linares, J. A., Axinte, D. A., et al. (2021). Surface integrity in metal machining - Part II: Functional performance. *International Journal of Machine Tools and Manufacture*, 164, 103718. doi: https://doi.org/10.1016/j.ijmachtools.2021.103718.

[129] Zhou, N., Pettersson, R., Peng, R. L., & Schonning, M. (2016). Effect of surface grinding on chloride induced SCC of 304L. *Materials Science and Engineering a-Structural Materials Properties Microstructure and Processing*, 658, 50-59.
doi: https://doi.org/10.1016/j.msea.2016.01.078.

[130] Zhou, N., Pettersson, R., Schonning, M., & Peng, R. L. (2018). Influence of surface grinding on corrosion behavior of ferritic stainless steels in boiling magnesium chloride solution. *Materials and Corrosion*, 69(11), 1560-1571.
doi: https://doi.org/10.1002/maco.201810206.

[131] Metcalfe, R. G., & Pearce-Boltec, N. (2018). Stress corrosion cracking of a copper elbow fitting. *Engineering Failure Analysis*, 90, 197-201.
doi: https://doi.org/10.1016/j.engfailanal.2018.03.016.

[132] Du, X. S., Su, Y. J., Li, J. X., Qiao, L. J., & Chu, W. Y. (2012). Inhibitive effects and mechanism of phosphates on the stress corrosion cracking of brass in ammonia solutions. *Corrosion Science*, 60, 69-75.
doi: https://doi.org/10.1016/j.corsci.2012.04.011.

[133] Du, X. S., Su, Y. J., Zhang, C., Li, J. X., Qiao, L. J., Chu, W. Y., et al. (2013). Pre-strain enhances film rupture to promote SCC of brass in Mattsson's solution – A proposal for a film-rupture-induced SCC mechanism. *Corrosion Science*, 69, 302-310. doi: https://doi.org/10.1016/j.corsci.2012.11.043.

[134] Metallnormcentralen (1970) 'SIS 117102:1970' Stress corrosion test for copper alloys using ammoniacal copper sulphate solution.

[135] Metallnormcentralen (1988) 'SS-ISO 6957:1988' Copper alloys - Ammonia test for stress corrosion resistance (ISO 6957:1988).

[136] Zhou, J. M., Bushlya, V., Peng, R. L., Johansson, S., Avdovic, P., & Ståhl, J. E. (2011). Effects of Tool Wear on Subsurface Deformation of Nickel-based Superalloy. *1st Cirp Conference on Surface Integrity (Csi)*, 19, 407-413.
doi: http://doi.org/10.1016/j.proeng.2011.11.133.

[137] Bushlya, V., Zhou, J. M., & Ståhl, J. E. (2014). Modeling and experimentation on multistage work-hardening mechanism in machining with nose-radiused tools and its influence on machined subsurface quality and tool wear. *International Journal of Advanced Manufacturing Technology*, 73(1-4), 545-555.
doi: https://doi.org/10.1007/s00170-014-5837-0.

[138] Sakai, T., Belyakov, A., Kaibyshev, R., Miura, H., & Jonas, J. J. (2014). Dynamic and post-dynamic recrystallization under hot, cold and severe plastic deformation conditions. *Progress in Materials Science*, 60, 130-207.
doi: https://doi.org/10.1016/j.pmatsci.2013.09.002.

[139] United Nations. (2016). Transforming our world: The 2030 agenda for sustainable development.

[140] Jovane, F., Yoshikawa, H., Alting, L., Boër, C. R., Westkamper, E., Williams, D., et al. (2008). The incoming global technological and industrial revolution towards competitive sustainable manufacturing. *CIRP Annals*, 57(2), 641-659.
doi: https://doi.org/10.1016/j.cirp.2008.09.010.

[141] Wieland Werke AG. https://www.wieland.com/en/resources/metal-information#metal-information . Accessed 2022-05-05 .

[142] Johansson, J., Ivarsson, L., Stahl, J. E., Bushlya, V., & Schultheiss, F. (2017). Hot forging operations of brass chips for material reclamation after machining operations. *Procedia Manufacturing*, 11, 584-592.
doi: http://doi.org/10.1016/j.promfg.2017.07.152.

[143] Johansson, J., Gutnichenko, O., Ståhl, J. E., Bushlya, V., & Schultheiss, F. (2019). Determining process parameters for successful material reclamation of lead-free brass chips using hot forging operations: Lubrication. *Procedia CIRP*, 80, 108-113.
doi: https://doi.org/10.1016/j.procir.2019.01.086.

[144] Kaplan, R. S., & Ness, H. (1987). Recycling of Metals (Reprinted from Encyclopedia of Materials Science and Engineering, 1986). *Conservation & Recycling*, 10(1), 1-13. doi: https://doi.org/10.1016/0361-3658(87)90002-6.

[145] Duflou, J. R., Tekkaya, A. E., Haase, M., Vanmeensel, K., Kellens, K., Dewulf, W., et al. (2015). Environmental assessment of solid state recycling routes for aluminium alloys: Can solid state processes significantly reduce the environmental impact of aluminium recycling? *CIRP Annals*, 64(1), 37-40.
doi: https://doi.org/10.1016/j.cirp.2015.04.051.

[146] Paraskevas, D., Kellens, K., Dewulf, W., & Duflou, J. R. (2015). Environmental modelling of aluminium recycling: a Life Cycle Assessment tool for sustainable metal management. *Journal of Cleaner Production*, 105, 357-370.
doi: https://doi.org/10.1016/j.jclepro.2014.09.102.

[147] Khamis, S. S., Lajis, M. A., & Albert, R. A. O. (2015). A Sustainable Direct Recycling of Aluminum Chip (AA6061) in Hot Press Forging Employing Response Surface Methodology. (Paper presented at the 12th Global Conference on Sustainable Manufacturing - Emerging Potentials).
doi: https://doi.org/10.1016/j.procir.2014.07.023

[148] Zhang, J., Pang, X., Chen, H., Shi, G., & Deng, W. (2019). Process and forming performance of ploughing extrusion cutting for recycling of metal chips. *Journal of Materials Processing Technology*, 274, 116283.
doi: https://10.1016/j.jmatprotec.2019.116283.

[149] Yusuf, N. K., Lajis, M. A., Daud, M. I., & Noh, M. Z. 315 (2013) 'Effect of operating temperature on direct recycling aluminium chips (AA6061) in hot press forging process' *Applied Mechanics and Materials*. Trans Tech Publ, pp. 728-732.

[150] Lee, C. M., Choi, Y. H., Ha, J. H., & Woo, W. S. (2017). Eco-Friendly Technology for Recycling of Cutting Fluids and Metal Chips: A Review. *International Journal of Precision Engineering and Manufacturing-Green Technology*, 4(4), 457-468.
doi: https://doi.org/10.1007/s40684-017-0051-9.

[151] Topolski, K., Bochniak, V., Lagoda, M., Ostachowski, P., & Garbacz, H. (2017). Structure and properties of titanium produced by a new method of chip recycling. *Journal of Materials Processing Technology*, 248, 80-91.
doi: https://doi.org/10.1016/j.jmatprotec.2017.05.005.

[152] Murray, J. W., Speidel, A., Jackson-Crisp, A., Smith, P. H., Constantin, H., & Clare, A. T. (2021). Unprocessed machining chips as a practical feedstock in directed energy deposition. *International Journal of Machine Tools and Manufacture*, 169, 103803. doi: https://doi.org/10.1016/j.ijmachtools.2021.103803.

[153] da Costa, C. E., Zapata, W. C., & Parucker, M. L. (2003). Characterization of casting iron powder from recycled swarf. *Journal of Materials Processing Technology*, 143-144, 138-143. doi: https://doi.org/10.1016/s0924-0136(03)00394-7.

[154] Philip, P. K., & Basheerkutty, Y. (1991). Reclamation of metal cutting brass chips using powder metallurgy. *Powder Metallurgy*, 34(1), 45-52.

[155] Radomyselskii, I., Baglyuk, G., & Mazharova, G. (1984). Production and properties of brass-base P/M constructional materials. A review. *Soviet Powder Metallurgy*, 23(3), 218-225.

[156] Nakagawa, T., Tanaka, T., & Amano, T. (1978). Powder Forging of High-Strength Brass and Its Application to Automobile Parts. *Journal of Mechanical Working Technology*, 2(2), 179-195. doi: https://doi.org/10.1016/0378-3804(78)90006-2.

[157] Manukyan, N., Khachatryan, L., Petrosyan, G., Bodzhikyan, É., Petrosyan, K. L., Gevorkyan, A., et al. (1983). Production technology and properties of extruded materials from brass swarf. *Soviet Powder Metallurgy*, 22(6), 474-478.

[158] Johansson, J., & Ivarsson, L. (2016). Tekniska förutsättningar för spånsmide av mässingskomponenter.

[159] Johansson, J., Furberg, A., & Schultheiss, F. 13 (2020) 'Screening Environmental Impact Reduction Enabled by Brass Reclamation Through Hot Forging Operations' *Advances in Transdisciplinary Engineering, 9th Swedish Production Symposium, SPS 2020*. IOS Press BV, pp. 241-248. Available at: https://www.scopus.com/inward/record.uri?eid=2-s2.0-85098635889&doi=10.3233%2fATDE200162&partnerID=40&md5=1a71bff534ddaa8e1f6dfc04ad60d086.

[160] German, R. M. (2005). Powder metallurgy and particulate materials processing: the processes, materials, products, properties, and applications. Metal powder industries federation Princeton.

[161] Gutnichenko, O., Bushlya, V., Bihagen, S., & Ståhl, J.-E. (2018). Influence of GnP additive to vegetable oil on machining performance when MQL-assisted turning Alloy 718. *Procedia Manufacturing*, 25, 330-337.

[162] Tillman, A., & Baumann, H. (2004). The Hitchhikers guide to LCA. Lund, Sweden: Studentlitteratur AB.

[163] Frischknecht, R., Wyss, F., Knopfel, S. B., Lutzkendorf, T., & Balouktsi, M. (2015). Cumulative energy demand in LCA: the energy harvested approach (journal article). *International Journal of Life Cycle Assessment*, 20(7), 957-969. doi: https://doi.org/10.1007/s11367-015-0897-4.

[164] Huijbregts, M. A. J., Steinmann, Z. J. N., Elshout, P. M. F., Stam, G., Verones, F., Vieira, M., et al. (2017). ReCiPe2016: a harmonised life cycle impact assessment method at midpoint and endpoint level. *International Journal of Life Cycle Assessment*, 22(2), 138-147. doi: https://doi.org/10.1007/s11367-016-1246-y.

[165] Ecoinvent (2018). Ecoinvent database version 3.5. Accessed.

[166] GreenDelta (2019). Open LCA software version 1.8. Accessed.

[167] Ekvall, T., & Tillman, A. M. (1997). Open-Loop Recycling: Criteria for Allocation Procedures. *International Journal of Life Cycle Assessment*, 2(3), 155-162. doi: https://doi.org/10.1007/Bf02978810.

v_c

Shear plane

Pb film on
fracture surface

Cutting tool

Area with
detected Pb

ε_I

h_1

τ_s

Contact zone

Area without
detected Pb

$\phi(t)$

ε_{III}

Crack formation and
heavily deformed Pb grains

Pb film on
machined surface

Pb grains